

Self-assembly, rheological properties and self-healing studies of supramolecular polymers in the bulk state

Dissertation

zur Erlangung des Naturwissenschaften
Dr. rer. nat.

der

Naturwissenschaftliche Fakultät II
Chemie, Physik und Mathematik

der Martin-Luther-Universität
Halle-Wittenberg

vorgelegt von

Herr **Tingzi Yan**

geboren am 17.10.1984 in Shandong China

Halle (Saale), July, 2015

Gutachter:

1. Prof. Dr. Thomas Thurn-Albrecht
2. Prof. Dr. Wolfgang Paul
3. Prof. Dr. Sebastian Seiffert

Öffentliche Verteidigung: 30. November 2015

Contents

| | | |
|----------|--|-----------|
| 1 | Introduction | 1 |
| 1.1 | Supramolecular polymers | 2 |
| 1.1.1 | Supramolecular polymers in dilute solution | 4 |
| 1.1.2 | Supramolecular assemblies in the bulk state | 6 |
| 1.2 | Supramolecular block polymers | 8 |
| 1.3 | Self-healing materials | 10 |
| 1.4 | Purpose and construction of the thesis | 11 |
| 2 | Basic concepts | 13 |
| 2.1 | Block copolymers | 13 |
| 2.1.1 | Basics of thermodynamics | 13 |
| 2.1.2 | Asymmetric Block copolymers | 15 |
| 2.2 | Small angle x-ray scattering | 15 |
| 2.2.1 | Scattering vector | 16 |
| 2.2.2 | Form factor | 16 |
| 2.2.3 | Structure factor | 18 |
| 2.2.4 | Bragg equation | 20 |
| 2.2.5 | Miller index | 21 |
| 2.2.6 | Reciprocal lattice | 22 |
| 2.3 | Rheological properties of polymer melt, network and colloidal suspension | 22 |
| 2.3.1 | Basic knowledge | 22 |
| 2.3.2 | Rheological properties of polymer melt | 27 |
| 2.3.3 | Rheological properties of dynamic network and critical gel | 30 |
| 2.3.4 | Rheological properties of colloidal suspensions | 31 |
| 2.4 | Nonlinear rheology | 33 |
| 2.4.1 | Strain sweep in oscillatory shear measurement | 33 |
| 2.4.2 | Startup shear | 33 |
| 2.4.3 | Stress relaxation at large step strain | 35 |
| 3 | Experimental methods | 37 |
| 3.1 | Small angle X-ray scattering | 37 |
| 3.2 | Rheology | 39 |
| 3.2.1 | Introduction of the rheometer | 39 |
| 3.3 | Infrared spectroscopy | 40 |

| | | |
|----------|--|------------|
| 4 | Nanostructure and Rheology of Hydrogen-Bonding Telechelic Polymers in the Melt: From Micellar Liquids and Solids to Supramolecular Gels | 43 |
| 4.1 | Samples | 43 |
| 4.2 | Results and Discussion | 44 |
| 4.2.1 | Analysis of the micellar superstructure of the monofunctional polymer Tr-PIB in the melt | 44 |
| 4.2.2 | Disordered phase of Th-PIB in the bulk state | 51 |
| 4.2.3 | Micellar superstructure in a mixture of two complementary, monofunctional telechelic polymers Tr-PIB+Th-PIB | 52 |
| 4.2.4 | Temperature dependent supramolecular networks of micellar aggregates | 57 |
| 4.2.5 | Unspecific hydrogen bonding by Infrared spectroscopy | 60 |
| 4.3 | Conclusion | 62 |
| 5 | Supramolecular PnBA-PIB block copolymer | 63 |
| 5.1 | Sample | 64 |
| 5.2 | Structural information from SAXS analysis | 64 |
| 5.3 | Rheological data of supramolecular block copolymer PnBA-PIB | 68 |
| 5.4 | Conclusion | 70 |
| 6 | Nonlinear Rheology and Self-healing properties of Supramolecular PIB network | 71 |
| 6.1 | Samples | 72 |
| 6.2 | Results and Discussion | 72 |
| 6.2.1 | Evidence for Interconnected micellar network from SAXS and rheological analysis | 72 |
| 6.2.2 | Nonlinear rheological analysis | 84 |
| 6.2.3 | Modulus recovery (Self-healing) analysis after sample failure | 90 |
| 6.3 | Conclusion | 92 |
| 7 | Summary | 93 |
| | Appendix | 97 |
| | Bibliography | 101 |

Chapter 1

Introduction

Polymers are large molecules with hundreds to thousands of repeating monomeric units linked by covalent bonds [1]. From 19th century, people started to use natural polymers and developed the semi-synthetic materials based on natural polymers. In 1907, the first synthetic polymer was invented by Leo Baekeland, known as the Bakelite, a thermosetting phenol-formaldehyde resin.

The nature of polymers was not clearly understood until a long time after polymers were used as materials. From 19th century, the polymers were taken as colloids aggregated from small molecules through intermolecular forces. In 1920, Hermann Staudinger proposed [2] that rubber and other polymers such as starch, cellulose and proteins are long chains with repeating monomeric units linked by covalent bonds. It was a completely different understanding of polymers compared to the prevailing idea during that time which stated that polymers were just a kind of aggregated colloids. The idea of taking polymers as long chains was gradually accepted in the 1920s. We take polyisobutylene (PIB) as an example. The monomeric

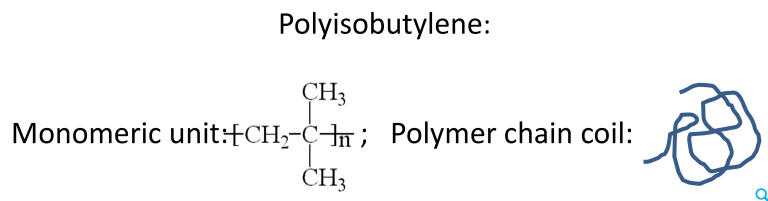


Figure 1.1: Polyisobutylene: the monomeric unit, and the chain configuration.

unit and the chain configuration is shown in Figure 1.1.

The acceptance of the concept of polymers laid the cornerstone for the polymer science and great progress was achieved in the following decades. Polymers have many advantages compared to the traditional materials, such as high strength with very low density, corrosion resistance, thermal insulation and so on. Many polymers with excellent performances for different purposes were developed and a large amount of synthetic polymers were consumed every year, which also influenced the whole society and everyday life of human being.

Later on, as the demands of materials with better performance increased, polymer blending was found to be a very useful tool to get new materials [3]. By blending two different polymers, the new materials can have the advantageous properties of both components. But

gradually the disadvantages were also noticed. Because many polymer blends are liable to have macrophase separation due to the miscibility of the different components, the polymer blends show low stabilities and thus the application of blending is limited.

Another method to develop new polymers is to use copolymerization of different monomeric units to create copolymers. Block copolymers, as the most extensively studied and widely used copolymers, are polymers with two or more blocks connected by covalent bonds. Because of the covalent connection of different blocks, macrophase separation between

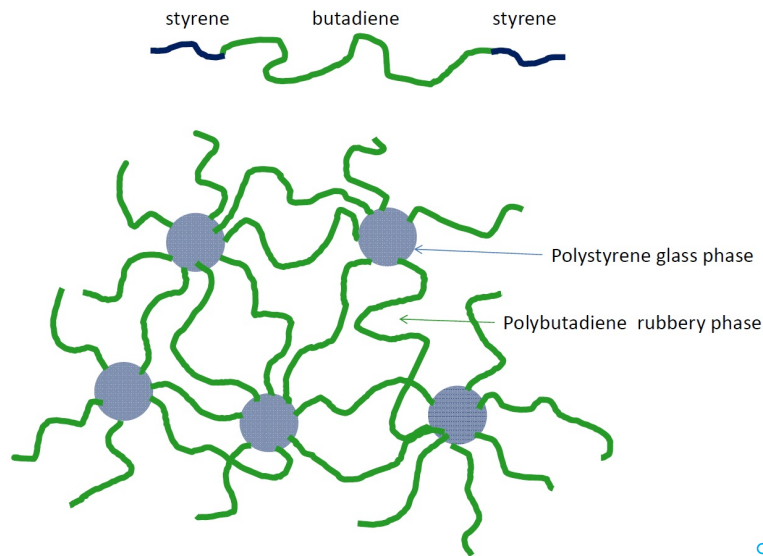


Figure 1.2: Molecular structure of the Poly(styrene-butadiene-styrene) block copolymer and schematic figure of the physical crosslinked SBR network.

different blocks is hindered. Instead, microphase separation could happen and it leads to different structural formation at nano-scale [4].

Block copolymers have many interesting properties. For example, the triblock copolymer Poly(styrene-butadiene-styrene) (SBS) can be used as the thermoplastic elastomer, as shown in Figure 1.2. Because of the microphase separation between the polystyrene (PS) block and the polybutadiene (PB) block, the glassy PS block segregates into cluster and acts as immobile crosslink points while the flexible PB block acts as the matrix and behaves like elastic chains. At room temperature, the sample behaves like a chemical cross-linked rubber, while the sample flows at high temperatures with heating and can be reprocessed. For comparison, due to the chemical cross-linked nature of the traditional rubber, the recycle (reprocessing) is not possible unless the polymer is degraded.

1.1 Supramolecular polymers

Supramolecules (supramolecular assemblies) are molecular assemblies different from traditional molecules [5, 6]. Traditional molecules are formed through strong bonding like covalent bonding, while weak reversible interactions, like hydrogen bonds, are more impor-

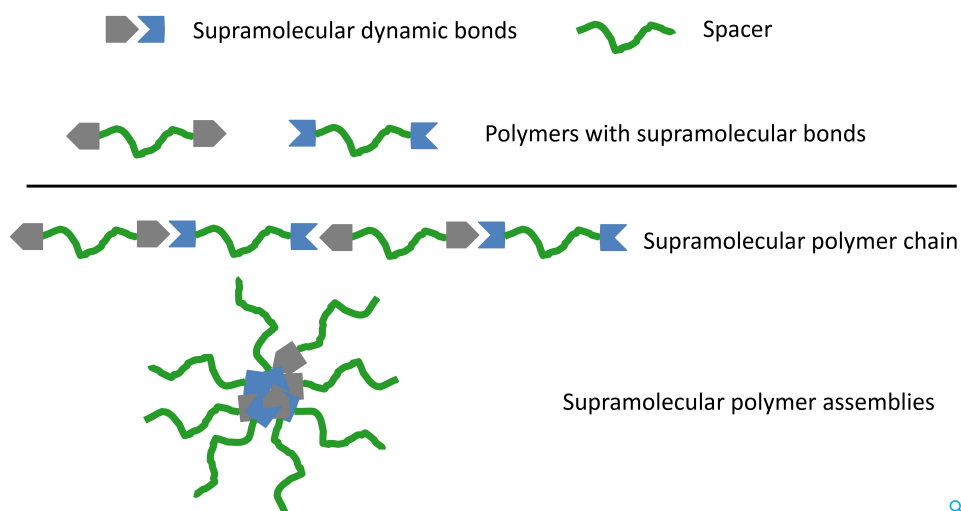


Figure 1.3: Nonmenclatures in supramolecular polymers and corresponding schemes.

tant in the supramolecule area. With the reversible dynamic bonding, the molecules can be assembled into different supramolecular structures (assemblies).

In 1990th, the idea to combine the supramolecules and polymers was realized by Lehn [7]. Large molecules are formed by connecting the monomeric units one by one through dynamic bonding. Such large molecules are called supramolecular polymers.

Supramolecular polymers are large molecules in which reversible dynamic bonding, like multiple hydrogen bonding [8–10], metal-ligand bonding [11, 12], plays an important role in structure formation and mechanical properties.

The monomeric units of supramolecular polymers are composed of dynamic bonding groups and spacers. The spacers of monomeric units can either be small monomeric units like traditional monomers or "medium-sized chain" (with molecular weight from several hundred Dalton [13] to several ten thousand Dalton [14]) "monomeric" units. Figure 1.3 shows an scheme of supramolecular polymers based on the second case. The supramolecular "monomeric" units with medium-sized chains can be taken as telechelic polymers with supramolecular groups or polymers with supramolecular bonds. The dynamic bonding can be hydrogen bonds [8–10], ionic bonds [15, 16], metal-ligand bonds [11, 12] and so on.

With the development of supramolecular chemistry, the supramolecular polymer systems contain not only linear supramolecular polymers and supramolecular polymer networks but also supramolecular polymer assemblies with high degree of internal order [17], such as nanofibers, nanoribbons and nanotubes.

Due to the inclusion of dynamic bonding groups into polymeric system, the dynamics of hydrogen bonding is also involved in the supramolecular polymers. They can be tuned easily by temperature changes. One potential application of supramolecular polymers is to get the easy processing polymer. At lower temperature, the supramolecular polymers act as the real polymers. While at higher temperature, the supramolecular polymers disassociate into small monomeric units. The viscosity can be strongly decreased due to the absence of entanglements and reduction of the molecular weight. Recently Leibler [18] reported an example of an easy processing material based on supramolecular polymers.

Another potential application of supramolecular polymers is self-healing materials [19–22] or stimuli-response materials [23]. After the materials are broken, the dynamic bonds can recombine and it leads to automatic healing. Since the dynamic bonding can be sensitive to different kinds of stimuli [23], e.g. temperature, light, sonication, electrical potential, the supramolecular polymer materials can be used in many different areas.

Due to the attractive potential applications, supramolecular polymers were studied extensively in the past decades. Understanding of supramolecular polymers in dilute solution is relatively clear. While supramolecular polymers in the bulk state are not studied extensively and quantitative studies are rare, e.g., the correlation between structure and mechanical properties. Since the supramolecular polymers are mostly applied in the bulk state, the studies of supramolecular polymers in the bulk state are important and highly needed.

In the following part, the reported studies on supramolecular polymers in the solution and in the bulk state will be reviewed.

1.1.1 Supramolecular polymers in dilute solution

It was reported by many groups [24–28] that supramolecular polymers were formed through dynamic bonding connection of "monomeric" units. In the supramolecular polymers, the most important thing is the dynamic bonding.

The parameter to describe the dynamic bonding is the association constant (K_a). Assuming A and B are the hydrogen bonding units, they can form hydrogen bonding state $A\cdots B$. Then in the equilibrium state, the association constant can be represented with the following equation.



where $[A\cdots B]$, $[A]$, $[B]$ represent the concentration of $A\cdots B$, A and B species respectively.

From thermodynamic point of view, the association constant of hydrogen bonding is related to the free energy of the hydrogen bonding process ΔG_a , as shown in the following equation:

$$K_a = \exp\left(-\frac{\Delta G_a}{RT}\right) \quad (1.2)$$

In supramolecular polymer solution, the bifunctional supramolecular polymeric units can form long dynamic chains by head-tail linkage, just like the polymerization process. One simple model used to describe the relation between the degree of "polymerization" (DP) and the association constant (K_a) is the isodesmic model. The model assumes that the association constant is independent on the chain length. The relation between DP and K_a can be represented by the following equation [10, 25].

$$DP = \frac{1 + \sqrt{1 + 4K_a C_0}}{2} \approx \sqrt{K_a C_0} \quad (1.3)$$

where C_0 is the concentration of supramolecular polymer with a unit of mol/L.

If the supramolecular monomer has a short spacer, like the normal polymeric repeating unit and the concentration of the supramolecular polymer solution is 0.1 M^{-1} ($\text{M}=\text{mol/L}$), then we need the association constant larger than 10^5 M^{-1} to get a DP larger than 100. If the supramolecular monomer has a long spacer, e.g. an oligomer with molecular weight of 10^4 g/mol , then a smaller K_a (10^3 M^{-1}) could lead to a supramolecular polymer with molecular weight of 10^5 g/mol .

To have high polymerization degree, hydrogen bonding pairs with higher association constant need to be developed, i.e. multiple hydrogen bonding. The following Figure 1.4 shows some multiple hydrogen bonding pairs and the corresponding K_a .

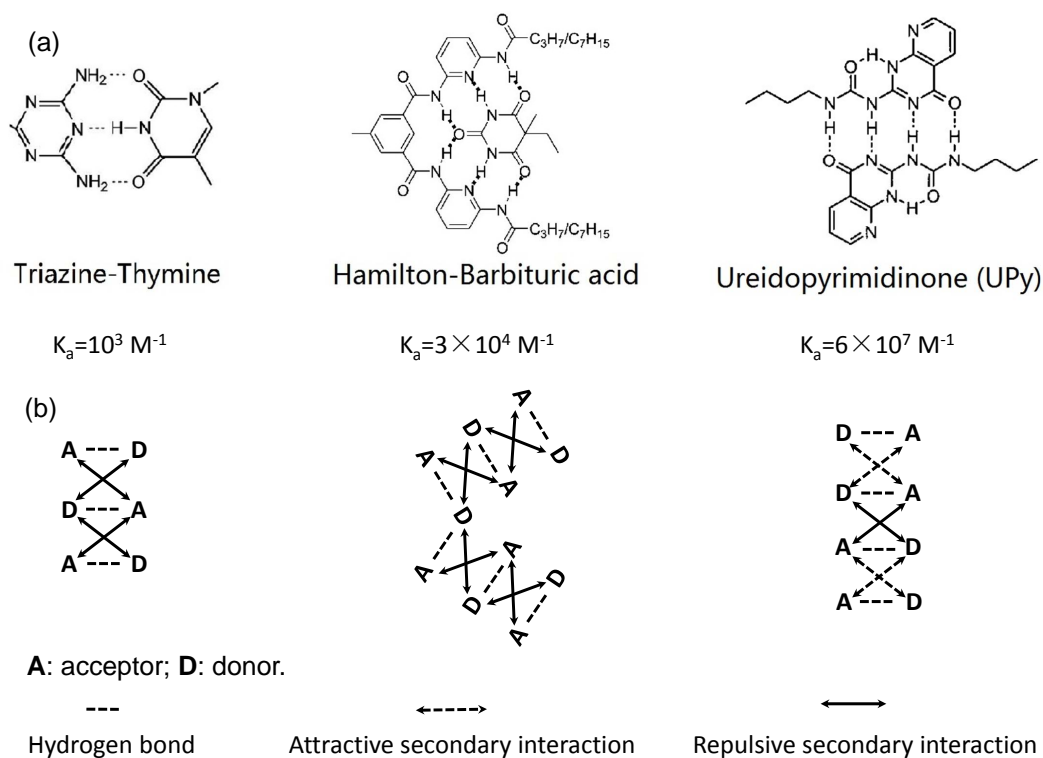


Figure 1.4: (a) Three multiple hydrogen bonding pairs, their association constants and (b) the corresponding hydrogen bonding interactions and the secondary interactions in solution.

Figure 1.4 shows three widely used multiple hydrogen bonding pairs. The triazine/thymine groups were first developed during 1980th and such hydrogen bonding pair has an association constant of 10^3 M^{-1} . The barbituric acid/ hamilton wedge hydrogen bonding groups were developed by Hamilton et al. The hydrogen bonding has a higher association constant of around $3 \times 10^4 \text{ M}^{-1}$. The self-complementary quadruple hydrogen bonding units ureidopyrimidinone (UPy) was first synthesized by Meijer's group [25]. The hydrogen bonding groups have a association constant of around $6 \times 10^7 \text{ M}^{-1}$ in chloroform solution. The UPy groups are widely used as the strong associative hydrogen bonding groups in the recent

decades.

There are many factors that influence the association constants of the hydrogen bonding pairs, e.g. the number of hydrogen bonds formed per hydrogen bond array, and secondary electrostatic interactions, the polarity of solvent, and the substituent group on the hydrogen bonding groups.

The association constant of hydrogen bonding can be increased by increasing of the number of hydrogen bonds formed per hydrogen bonding pair. This is easy to understand and that's why many different kinds of multiple hydrogen bonding pairs have been synthesized in the past years [9, 10].

But higher number of hydrogen bonds may not lead to higher association constant, for example, the Hamilton wedge/barbituric acid forms a larger number of hydrogen bonds than the ureidopyrimidione while the association constant is less. This is because the secondary interaction also plays an important role. Sartorius and Schneider [29] found a simple relation between the free energy and the multiple hydrogen bonding complexes in chloroform. Each hydrogen bond contributes around 7.9 kJ/mol energy to the free energy and each secondary interaction energy contribute approx. ± 2.9 kJ/mol to the free energy. The lower part of Figure 1.4 is the schematic picture of hydrogen bonding interactions. Although the number of hydrogen bonding formed by Hamilton/Barbituric acid is larger than that of UPy, the association constant of Hamilton/Barbituric acid is even less because there is a larger amount of repulsive secondary interactions.

Since the hydrogen bonding unit is also electrostatic dipolar component, the polarity of solvent also influences the hydrogen bonding interaction. In a solvent with lower polarity, the hydrogen bonding has a higher association constant. For example, an AAAA-DDDD quadruple hydrogen-bonding array [30] has an association constant of $3 \times 10^{12} \text{ M}^{-1}$ in CH_2Cl_2 , and $1.5 \times 10^6 \text{ M}^{-1}$ in CH_3CN , and $3.4 \times 10^5 \text{ M}^{-1}$ in 10% v/v DMSO/ CHCl_3 .

Besides the linear chain formation, there could also be the side reaction like the cyclic ring formation [26]. Meijer reported that below a concentration, the formation of cyclic rings is dominant because of the very dilute solution and the high association constant of the hydrogen bonding groups.

1.1.2 Supramolecular assemblies in the bulk state

In the bulk state, because of the high concentration of functional groups the situation of the hydrogen bonding functional polymers is more complicated. Besides the hydrogen bonding interaction, one important driving force that influences the structural formation of hydrogen bonding functional polymers in the bulk state is the phase separation between the spacers and the hydrogen bonding groups. This makes the hydrogen bonding functional polymers analogous to the block copolymers and supramolecular aggregates might form instead of linear dynamic supramolecular polymer chains [31]. Different kinds of aggregates can be formed, e.g. the spherical aggregates [32, 33], crystalline structure [13, 34], fibrous structure [35, 36].

It was reported by Hayes [33] that although hydrogen bonding groups of the hydrogen bonding functional polymers segregate in the bulk state, the association constants of hydrogen bonding groups measured in solution are still valid to influence the structural forma-

tion and rheological properties of supramolecular polymers in the bulk state. They took use of a series of polyurethanes functionalized with different hydrogen bonding groups, all of which had association constants lower than 50 M^{-1} , and they found the hydrogen bonding groups aggregated and supramolecular elastomers formed instead of linear dynamic chains. From SAXS data, the aggregates of hydrogen bonding groups becomes larger and the demixing/phase separation between hydrogen bonding groups and polyurethane become stronger with increasing association constant. From rheological measurements, the temperature for flow became also higher with increasing association constant. This means that although microphase separated structure (supramolecular elastomers) instead of linear chains is formed, both the morphology and rheological properties of the hydrogen bonding functional polyurethane in the bulk state correlated with the binding constants of the hydrogen bonding end groups measured in the dilute solution.

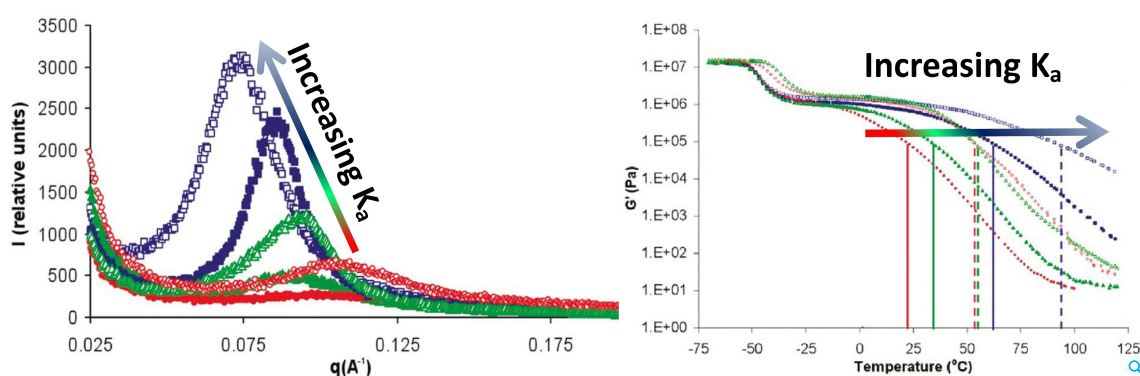


Figure 1.5: SAXS pattern and rheological curves for a series of hydrogen bonded supramolecular polyurethane elastomers with different functional groups [33].

For the case shown above, the correlation works well because they all form the same kind of aggregates. However, if the hydrogen bonding functional polymers form different kinds of aggregates, the correlation between structure/rheological properties and association constants can be lost. Leibler [37] studied the thymine/triazine functionalized supramolecular poly(propylene oxide) monomeric units in the bulk state and found that the polymers functionalized with strongly complementary hydrogen bonding groups shows liquid behaviour while the polymers functionalized with weakly complementary hydrogen bonding groups is a solid. By SAXS measurements they found that the supramolecular polymer with weakly complementary hydrogen bonding groups shows ordered lamellar structure and the stickers crystallize while the strong complementary hydrogen bonding groups inhibit the crystallization of the stickers in the polymers functionalized with stronger complementary stickers.

Because of the strong self-complementary interaction of ureidopyrimidinon (UPy) groups, Meijer and other groups made extensive studies on the polymers functionalized with ureidopyrimidinone (UPy) hydrogen bonding groups. In most cases, no aggregates was observed in the UPy-functionalized polymers (PCL [35], PEB [36], PEP) except the supramolecular PDMS. In the UPy functionalized PDMS samples, nano-fibers were observed from AFM images. It was explained by the reason that the demixing between the UPy groups and the PDMS was too strong that the lateral π - π stacking makes the fiber aggregation possible. But

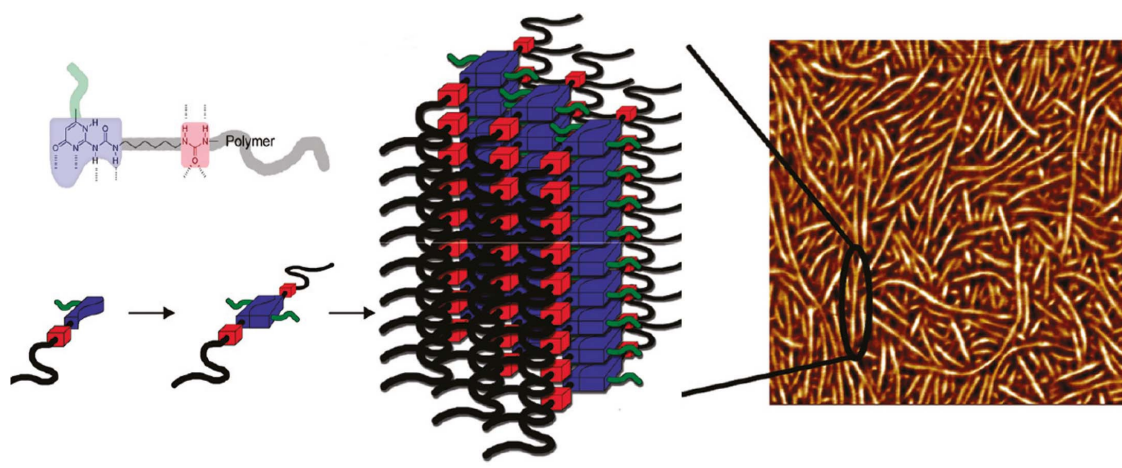


Figure 1.6: Molecular structure of UPy-urea functionalized supramolecular polymer and the steps of construction of nanofibers by hydrogen bonding and stacking [36].

when an urea group was embedded between the UPy group and the spacer (the polymer main chain or oligomer) [36], the nanofibers were observed for all the samples from AFM measurements, as shown in Figure 1.6. The mechanical properties were also found to be strongly enhanced. The nanofibers had a diameter of several nanometers and a length size of micrometer. It was proposed that the lateral hydrogen bonding between the urea groups induced stacking of the UPy-urea moieties and thus the formation of nanofibers. Further analysis with DSC and AFM suggested that the nanofibers were crystalline.

With the review of the past studies on hydrogen bonding functionalized polymers in the bulk state, we can see that in the bulk state they form various aggregates at the nanoscale instead of supramolecular polymer chains which are normally formed in dilute solution.

1.2 Supramolecular block polymers

Supramolecular block copolymers are block copolymers two or more blocks of which are linked by dynamic bonding instead of covalent bonding. To have the supramolecular block copolymer, two different polymers functionalized with complementary hydrogen bonding groups are mixed. To have a very stable supramolecular block copolymer, the dynamic bond should be strong enough to suppress the tendency of macrophase separation.

Binder [38] et.al reported that they synthesized two supramolecular PEK-PIB block copolymers with two kinds of hydrogen bonding linkers, as shown in Figure 1.7. With the weak hydrogen bonding linker, this supramolecular polymer survive up to 145 °C and above this temperature the supramolecular block copolymer macrophase separates and the structure is not reversible any more after cooling. With the strong hydrogen bonding linker, the supramolecular PEK-PIB block copolymer could survive up to 230 °C because of the stabler hydrogen bonding.

Another example of supramolecular block copolymer was observed by Meijer's group [39] recently. They synthesized the poly(dimethylsiloxane) functionalized with the urei-

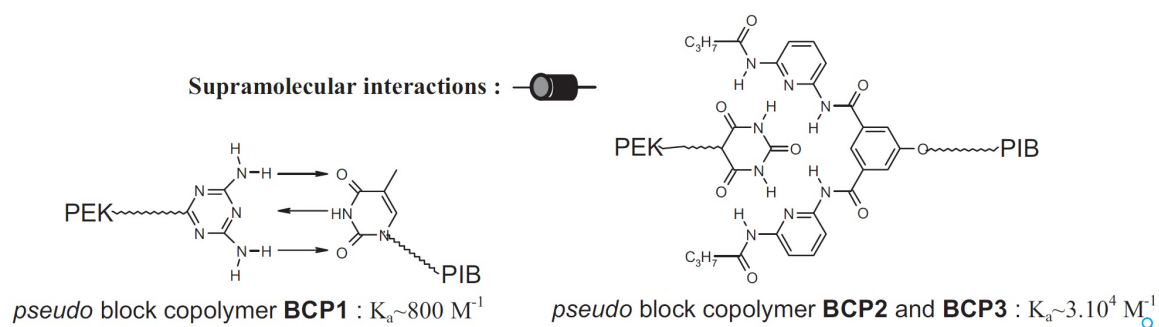


Figure 1.7: Supramolecular PEK-PIB block copolymer with two kinds of hydrogen bonding linkers: the thymine/triazine ($K_a=800 \text{ M}^{-1}$) and the hamilton wedge/barbituric acid ($K_a=3 \times 10^4 \text{ M}^{-1}$) [38].

doguanosine and the poly(DL-lactide) functionalized with 1,7-diamidonaphthyridines and mix them in a 1:1 stoichiometry. The supramolecular PDMS-PLA block copolymer linked with ureidoguanosine/2,7-diamido-1,8-naphthyridine (UG/Napy) hydrogen bonding was then obtained. With SAXS and the TEM measurements, the ordered lamellae structure was confirmed. This means that the UG/Napy hydrogen bonding is very strong that they have a strong binding energy compared with the demixing tendency for microphase separation between PDMS and PLA.

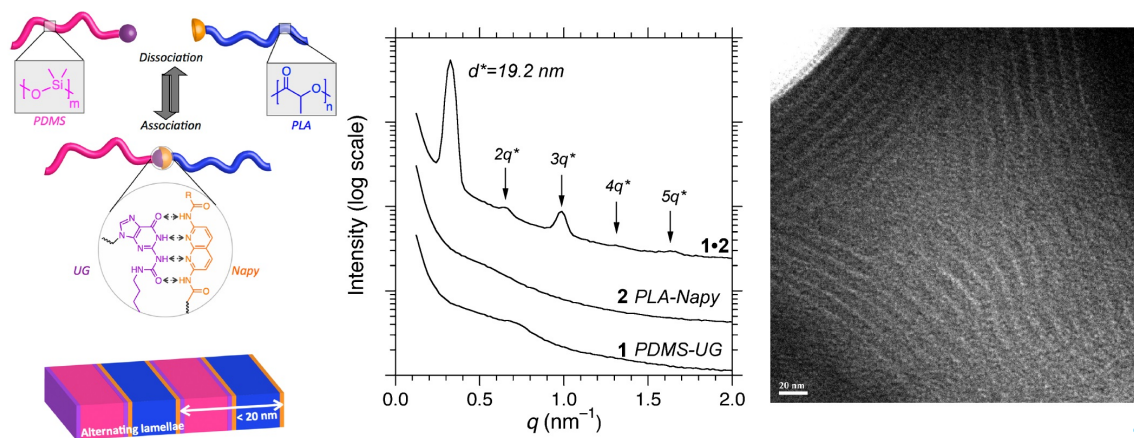


Figure 1.8: Left: Supramolecular PDMS-PLA block copolymer with ureidoguanosine/1,7-diamidonaphthyridines (UG/Napy) ($K_a = 10^7 \text{ M}^{-1}$; Middle: SAXS data of the supramolecular block copolymer shows several ordered peaks, corresponding to the lamellae structure; Right: the TEM image of supramolecular block copolymer shows ordered lamellae structure) [39].

Although a few cases of supramolecular block copolymer were reported already, detailed studies of supramolecular block copolymers are still rare. In one chapter of the thesis, we will focus on the studies of supramolecular block copolymers based on SAXS and rheological measurements.

1.3 Self-healing materials

As we discussed above, supramolecular polymers have many interesting potential applications. One important application is self-healing materials. Self-healing materials are functional materials that are able to heal after crack or broken. Such self-healing concept exists in the human body proverbially [40].

Self-healing concept was introduced to the material science more than 10 years ago by including the healing agents into the materials as microcapsules [40]. When the material got crack or damaged under external force, the monomers flow outside of the microcapsules and polymerize in the crack surfaces with the help of catalyst. Such self-healing method with microcapsules was also put into application, e.g. in the polymer coatings, and also bulk polymers.

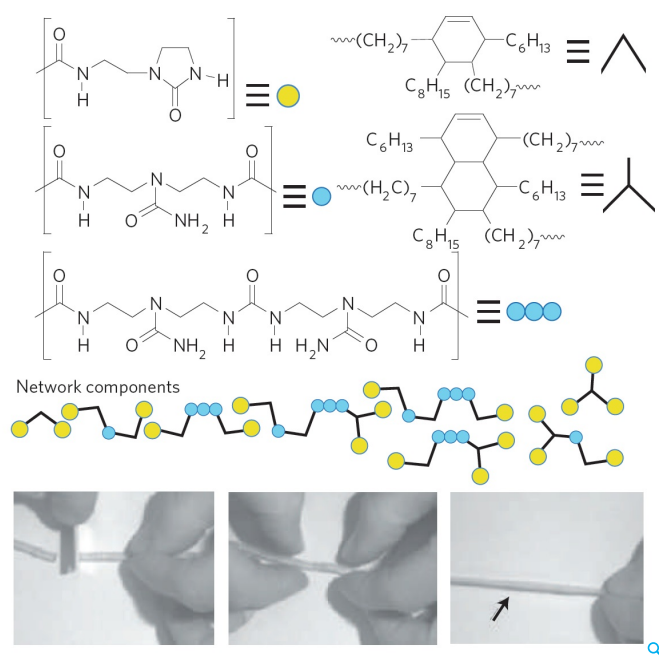


Figure 1.9: Self-healing rubber is based on several components of small molecules. With the chemical reaction and hydrogen bonding interaction, a dynamic network is obtained. The self-healing properties was proved with a test measurement [19].

Later, the supramolecular dynamic bonding was introduced into the self-healing materials to replace the effect of healing agent. For example, Leibler's system with small units composed of hydrogen bonding groups [19], Rowan's system with metal-organic bonds [20], and Binder's sample with hydrogen bonding [22]. Figure 1.9 shows the self-healing rubber system by Leibler's group. They took use of some fatty acids and diethylene diamine functionalized with urea to make an thermoplastic elastomer which shows prominent self-healing ability.

Compared to the self-healing materials with microcapsules, the self-healing materials with dynamic bonding have the advantage of repeated usage. Although many new self-healing materials based on supramolecular polymer networks are synthesized and reported,

the self-healing mechanism of the self-healing supramolecular polymer networks is not very clear till now.

1.4 Purpose and construction of the thesis

Purpose of the thesis

In this thesis, our work is mainly to take use of several supramolecular polymer systems to study the physical properties of hydrogen bonding functional polymers in the bulk state and also to study the supramolecular block copolymers in the bulk state and then finally the study of self-healing supramolecular polymer networks.

We have shown before that there are already some studies of hydrogen bonding functional polymers in the bulk state and they formed different kinds of aggregates. However, the detailed studies on correlation between structure and rheological properties and quantitative studies are still rare, which will be one of the aims of our studies of the first system in this thesis. The second aim is based on a question: now that hydrogen bonding functional polymers formed different kinds of aggregates in the bulk state, what is the role of the multiple hydrogen bonding? Is there any other factor that can influence the structural formation of hydrogen bonding functional polymers?

In the first system, the hydrogen bonding functional PIB contain PIB chains (around 3.5 kg/mol) as the spacers and thymine/triazine multiple hydrogen bonding groups as the stickers. With SAXS and rheological analysis, we (semi-)quantitatively studied the structural formation and rheological properties of different supramolecular PIB samples. The correlation between structural formation and rheological properties were also done.

Although there were already several cases which reported the successful synthesis of supramolecular block copolymers and the formation of the ordered structures, the detailed studies of temperature dependent SAXS analysis and rheological properties of supramolecular block copolymers are still in lack, which will be one aim of the studies of the second system. The second aim is to understand at which point the supramolecular block copolymer shows the "dynamic" behavior that covalently bonded block copolymer should not have due to the nature of the covalent bonding. In the second system, we took use of a supramolecular block copolymer Polyisobutylene-Poly(n-butyl acrylate)(PIB-PnBA) which is linked through hamilton wedge/barbituric acid (HW/BA) multiple hydrogen bonding. We studied the temperature dependent structural evolution and rheological properties by SAXS and rheology and try to understand the similar and different behaviors compared to the reported experimental results of covalently bonded block copolymers in the literature.

As we have shown before, self-healing materials were synthesized abundantly, while the mechanism of self-healing is not well understood. In the third system, we took use of a series of telechelic PIB samples functionalized with barbituric acid groups which shows self-healing properties. The aim of studies of the third system is to study the structural formation, linear, nonlinear rheological properties and self-healing kinetics of supramolecular polymer network.

Construction of the thesis

The structure of the thesis will be as following. In the second chapter, firstly we will give some basic knowledge about block copolymers. Small angle x-ray scattering and rheology are two main experimental methods used in our study, so the basics theory about SAXS and rheology will also be addressed.

In the third chapter, three experimental methods will be described, including the x-ray scattering instrument, the rheometer and Fourier transform infrared spectrometer (FTIR) and corresponding experimental methods.

In the fourth chapter, we will show our studies on several supramolecular PIB samples based on SAXS and rheological analysis. Because of the nonpolar PIB chains and polar hydrogen bonding groups, the demixing between PIB and hydrogen bonding groups happened, leading to the spherical micelles structure. The spherical micelles were further analysed based on colloidal suspension, and the SAXS analysis and rheological analysis results are consistent with each other.

In the fifth chapter, we will show our studies on a supramolecular block copolymer (PnBA-PIB) with SAXS and rheology. SAXS curve with higher ordered peaks shows that the lamellar structure was formed in the supramolecular PnBA-PIB block copolymers. Together with rheology, some differences were found between the real block copolymer and supramolecular block copolymer.

In the sixth chapter, we will show our studies on some supramolecular PIB samples with self-healing properties. Interconnected micellar network was formed in the sample. With nonlinear rheology, the network failure happened at higher shear strain and strain rate. The self-healing kinetics based on rheology was measured by modulus recovery.

In the seventh chapter, a summary is given to summarize our research results.

Chapter 2

Basic concepts

In this chapter, some basic concepts will be reviewed, aiming to give some knowledge about block copolymers, basics of small angle x-ray scattering (SAXS), linear rheology and non-linear rheology.

2.1 Block copolymers

Block copolymers are formed through connection of two or more different polymeric blocks. One important feature of block copolymers is that they can show microphase separated structure at length scale of nanometers due to the demixing tendency between different blocks.

2.1.1 Basics of thermodynamics

From the thermodynamic point of view, the free energy difference ΔG_m between the ordered state and disordered state can be calculated by [41]

$$\Delta G_m = G_d - G_o = \Delta H_m - T \Delta S_m \quad (2.1)$$

G_o and G_d are the free energies of block copolymers in ordered state and disordered state. ΔH_m and ΔS_m are the mixing enthalpy and entropy and they are individual functions of interaction parameters χ and polymerization degree of block copolymers N .

The state of block copolymer (ordered or disordered) depends on the sign of ΔG_m . ΔG_m equal to 0 corresponds to the order-disorder transition temperature (T_{ODT}). The kind of ordered structure mainly depends on volume fraction of one component f .

The factor that decide whether the block copolymer forms ordered phase or disordered phase is the product of the Flory-Huggins segmental interaction parameter χ and the polymerization degree N .

χ is the interaction parameter which is used to describe the enthalpy of demixing between two monomeric units and is defined in the following equation [42]

$$\chi = \frac{z}{2kT} (2u_{AB} - u_{AA} - u_{BB}) \quad (2.2)$$

z is the number of near interacting units around each monomer unit; u_{AB} , u_{AA} and u_{BB} represent individually the interaction energy between monomer units A/B, A/A and B/B. χ with the sign of plus means the repulsive interaction between A and B monomers. χ is temperature dependent as shown in the following equation $\chi = a + b/T$. (a and b are constants depending on the chemical structure of the block copolymer).

The phase state of block copolymer can be divided into three regimes related with the value range of χN : strong segregation limit ($\chi N > 100$), weak segregation limit ($\chi N \approx 10$) and the intermediate segregation limit (χN in the range of 10 to 100).

In the strong segregation regime [43], different blocks strongly demix and the block copolymers form different ordered structure depending on the volume fraction of one block. In the strong segregation regime, there is a narrow interface between two phases and the width of the interface is dependent on the χ parameter as $\propto \chi^{-1/2}$.

In the weak segregation regime, Leibler [44] did very important work. He considered the monodisperse diblock copolymer with interaction parameter χ , polymerization degree N , and volume fraction of one block f . The description of part of the work will be discussed later together with small angle x-ray scattering.

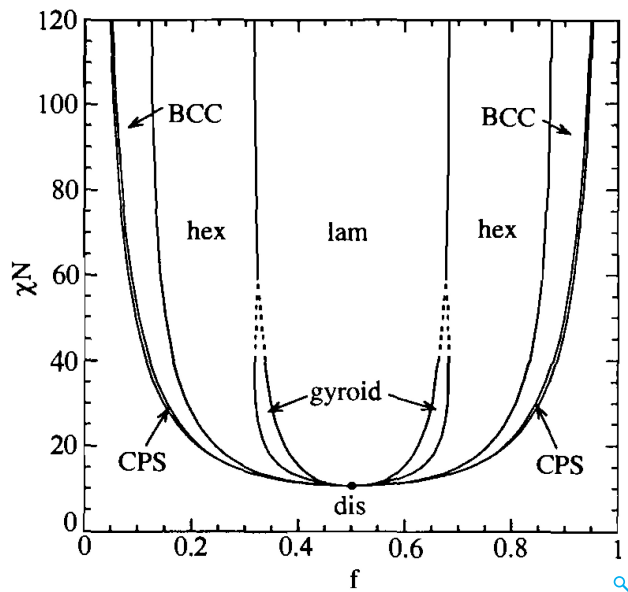



Figure 2.1: Phase diagram for a conformationally symmetric AB-type diblock copolymer predicted from the self-consistent mean-field theory [45,46]. There are several ordered morphologies: lamellar structure (lam); hexagonal cylindrical phase (hex); BCC, bicontinuous gyroid phase (gyroid); close packing spheres (CPS).

At intermediate segregation limit, Helfand [46] and coworkers developed the mean field theory for block copolymers. The theory is successful in predicting the more complex phases which were not predicted by the former theory. The phase diagram of the diblock copolymer is shown in Figure 2.1 [45,46]. From the phase diagram, the symmetric diblock copolymers form disordered phase for χN smaller than 10.5 and ordered lamellar phase for χN larger than 10.5. Different ordered phases are formed depending mainly on the volume fraction of one block f . For χN larger than 100, with increasing volume fraction of one block, BCC ordered

phase, hexagonal cylindrical phase, and lamellar ordered phase forms accordingly. Besides the three classical ordered phases, there are also two phases in the intermediate segregation limit: the gyroid phase between the lamellar and hexagonal phases and the CPS phase close to the order-disorder transition. From the phase diagram, with volume fraction of one block f and the χN , phase morphology of the block copolymers can be predicted.

2.1.2 Asymmetric Block copolymers

Asymmetric block copolymers are a kind of block copolymer where one block is much longer than the other one. Although Leibler was able to predict the direct transition from disordered Gaussian chains to body-centered-cubic (bcc) phase, an intermediate state of disordered micelles was not predicted and was observed experimentally [47, 48]. There are also two different views about the equilibrium phases of asymmetric block copolymers. Some argue that there are only two (bcc ordered micelles and a disordered phase) while some others argue three equilibrium states (bcc ordered micelles, disordered chains, and disordered micellar fluid). Later Lodge [49] experimentally found that the disordered micelle regime is only a part of the disordered phase and the transition between the disordered melt to the disordered micelle is not a **true transition**. 

For the disordered micelle state, Thomas et al [47] took the spherical micelles as hard spheres and use the Percus-Yevick hard sphere model to fit the SAXS patterns of disordered micelles. The fit worked well because of the strong entropic repulsive interactions between the near micelles from the micellar corona.

2.2 Small angle x-ray scattering

X-ray radiation was first discovered by Röntgen in 1890th, so it is also called Röntgen radiation. It is an electromagnetic radiation with wavelength from 0.01 to 10 nm. Due to its small wavelength and good penetrating ability, x-ray scattering can be used to study the structure with length scale from \AA to several nm . Laue, Ewald and Bragg were the first pioneers to use x-ray for the study of crystal structure and this opened the door for the wide application of x-ray. Later the x-ray scattering was also applied into polymer science by Guinier, Kratky and Porod et. al. During the last decades, SAXS technique has made a lot of progresses with the advances of detectors and x-ray sources, especially the rotating anode and synchrotron radiation. Till now SAXS is still one of the most important methods in the study of polymer science.

Small angle x-ray scattering is such a technique that when x-ray beam irradiates on the objects, the scattered x-ray is collected by the detector at the small scattering angle range and then the scattering data is used to resolve the structural information of the objects at nano-size scale.

Small angle x-ray scattering (SAXS), as a tool to detect the structural information at nano-scale, plays a very important role in the block copolymer research area.

If we only consider the coherent scattering, which normally happens at very small scattering angle, then the scattering pattern can be used to detect the structural information of the

heterogeneous structure. Some basics knowledge of x-ray scattering is needed to understand and analyse the SAXS data to resolve the structural information.

2.2.1 Scattering vector

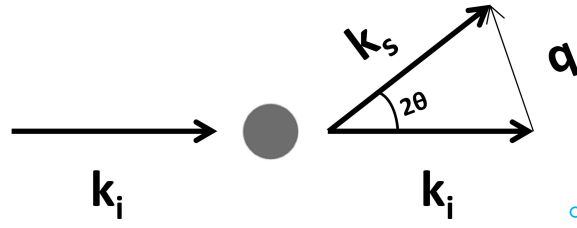


Figure 2.2: Schematic picture of x-ray beam scattered by a particle and the definition of scattering vector.

Imagine an incident x-ray beam with wavelength of λ and wave vector of \mathbf{k}_i is scattered by a particle (in Figure 2.2), and the scattered x-ray beam has a wave vector of \mathbf{k}_s . Scattering vector \mathbf{q} is defined in the following formula

$$\mathbf{q} = \mathbf{k}_s - \mathbf{k}_i \quad (2.3)$$

Assume the scattering is elastic, meaning there is no energy loss during the scattering and the wavelength is unchanged,

$$|\mathbf{k}_i| = |\mathbf{k}_s| = \frac{2\pi}{\lambda} \quad (2.4)$$

so the scattering vector $|\mathbf{q}|$ can be related to the scattering angle θ

$$|\mathbf{q}| = \frac{4\pi}{\lambda} \sin \theta \quad (2.5)$$

2.2.2 Form factor

Since the x-ray wave can be scattered by the electrons, the whole scattering intensity of a particle can be represented by the squared sum of scattering waves from all the electrons. The interference pattern depends on the shape (form) of the particle and the arrangement of the particles. In a dilute system of such particles, the whole scattering intensity is the sum of intensity from all particles. The scattering pattern from the particle is called form factor.

The scattering amplitude $A(\mathbf{q})$ from a single particle can be shown in the following equation [50]

$$A(\mathbf{q}) = \int_V \rho(\mathbf{r}) e^{-i\mathbf{q}\cdot\mathbf{r}} d\mathbf{r}. \quad (2.6)$$

where $\rho(\mathbf{r})$ is the scattering length density distribution.

The form factor $F(\mathbf{q})$ can be calculated by

$$F(\mathbf{q}) = |A(\mathbf{q})|^2 = \left| \int_V \rho(\mathbf{r}) e^{-i\mathbf{q}\cdot\mathbf{r}} d\mathbf{r} \right|^2 \quad (2.7)$$

For a solid sphere particle with radius of R and uniform density ρ_0 , the electron density at different position can be represented in the following

$$\rho(r) = \begin{cases} \rho_0, & |r| \leq R \\ 0, & |r| > R \end{cases}$$

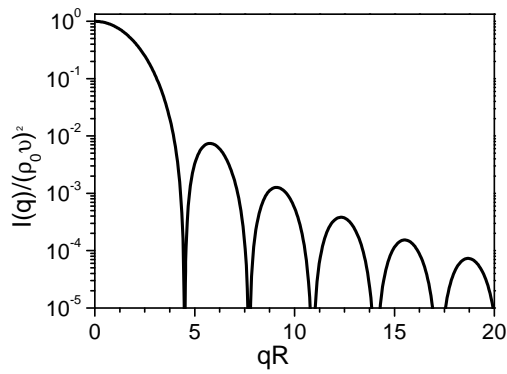


Figure 2.3: Scattering intensity of a spherical particle with radius R in dilute solution.

With further calculation,

$$A(q) = \rho_0 v \frac{3[\sin(qR) - qR\cos(qR)]}{(qR)^3} \quad (2.8)$$

where v is the volume of the sphere, $(4/3)\pi R^3$.

Then the form factor can be represented by

$$F(q) = \rho_0^2 v^2 \frac{9[\sin(qR) - qR\cos(qR)]^2}{(qR)^6} \quad (2.9)$$

The intensity of a sphere particle solution is plotted in Figure 2.3.

The scattering intensity $I(q)$ in dilute solution has such relation with the form factor $F(q)$

$$I(q) = \phi F(q) \quad (2.10)$$

Where ϕ is the volume concentration of the spheres.

2.2.3 Structure factor

Structure factor of block copolymers in disordered state

The structure factor $S(\mathbf{q})$ of the disordered phase was provided by Leibler [44] and is given by the following equation

$$\frac{1}{S(\mathbf{q})} = \frac{F(x, f)}{N} - 2\chi \quad (2.11)$$

where N is the degree of polymerization of the block copolymer, χ is Flory-Huggins interaction parameter, and

$$F(x, f) = \frac{D(1, x)}{D(f, x)D(1-f, x) - 1/4(D(1, x) - D(f, x) - D(1-f, x))^2} \quad (2.12)$$

where $D(f, x)$ is Debye function, defined as:

$$D(f, x) = \frac{2}{x^2}(fx - 1 + \exp(-fx)) \quad (2.13)$$

and

$$x = \frac{q^2 N b^2}{6} = q^2 R_g^2 \quad (2.14)$$

where f is the volume fraction of one block, b is the Kuhn length of two blocks, and R_g is radius of gyration of the random coil.

At $q=0$, $S(q)$ is 0 because the system is assumed to be incompressible. At large q ($qR_g \gg 1$), $S(q)$ is independent on χ and decrease with q as $1/q^2$:

$$S(q) = \frac{2N}{q^2 R_g^2} f(1-f) \quad (2.15)$$

At very small q ($qR_g \ll 1$), $S(q)$ is independent on χ and increases with q as q^2 .

$$S(q) \approx 2N f^2 (1-f)^2 \frac{q^2 R_g^2}{3} \quad (2.16)$$

With the equation of $S(q)$, it is know that the shape of the curve $S(q)$ v.s. x depends on χ and the peak position q^* at intensity maximum is independent on χ but on the volume fraction of one block f . The dependence of $q^{*2} R_g^2$ and the periodicity D ($D=2\pi/q^*$) on the volume fraction of one block f are plotted in solid line and dashed line respectively in Figure 2.4. At f around 0.5, $q^{*2} R_g^2$ and D change slowly with f . When the block copolymer is highly asymmetric, $q^{*2} R_g^2$ and D change rapidly with f . With such a relationship, the radius of gyration of the block copolymer in the disordered state can be estimated with the peak position q^* of the SAXS pattern.

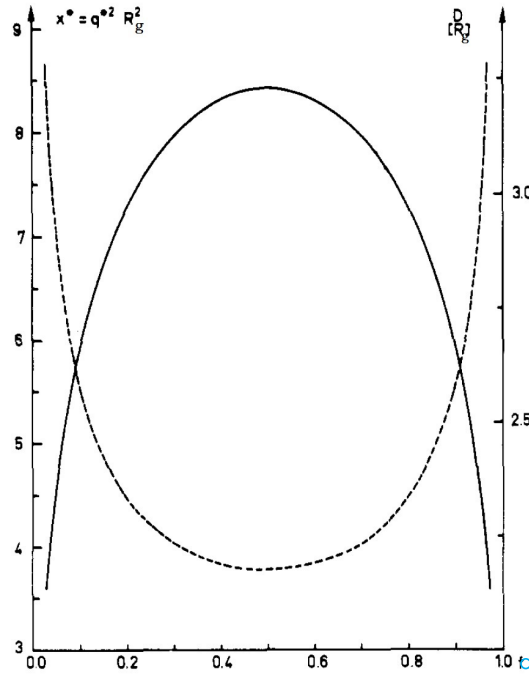


Figure 2.4: The plot of $q^*{}^2 R_g^2$ against f just above T_{ODT} is shown in solid line. The plot of the periodicity D ($D=2\pi/q^*$) against f just above T_{ODT} is plotted in dashed line [44].

Perkus-Yevick hard sphere model

When the particle solution is concentrated and the distance between the particles is comparable to the inverse of scattering vector $1/q$, the interference between the near particles also contributes to the scattering intensity and is called structure factor.

The model used to describe the structure factor of the colloidal sphere suspension is called Percus-Yevick model [47]. The structure factor of the hard sphere fluid model $S(qR_{hs})$ is shown in the following equation

$$S(qR_{hs}) = \left(1 + \frac{24fG(x)}{x} \right)^{-1} \quad (2.17)$$

where $x = 2qR_2$, and ϕ is the volume fraction of hard spheres.

$$\begin{aligned} G(x) = & \frac{\alpha}{x^2} (\sin x - x \cos x) \\ & + \frac{\beta}{x^3} (2x \sin x + (2 - x^2) \cos x - 2) \\ & + \frac{\gamma}{x^5} (-x^4 \cos x + 4[(3x^2 - 6) \cos x + (x^3 - 6x) \sin x + 6]) \end{aligned} \quad (2.18)$$

Here α , β and γ are functions of the volume fraction ϕ .

$$\alpha = (1 + 2\phi)^2 / (1 - \phi)^4, \quad \beta = -6\phi(1 + \phi/2)^2 / (1 - \phi)^4, \quad \gamma = 1/2\phi(1 + 2\phi)^2 / (1 - \phi)^4 \quad (2.19)$$

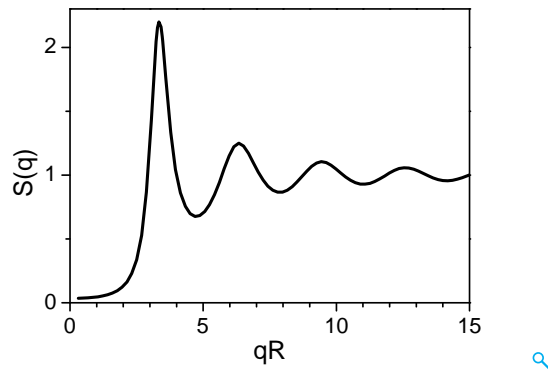


Figure 2.5: Structure factor of hard sphere system based on Percus-Yevick model.

An example of the plot with Percus-Yevick model is shown in Figure 2.5. The scattering intensity $I(q)$ can be represented by

$$I(q) = S(q)F(q) \quad (2.20)$$

2.2.4 Bragg equation

When the x-ray beam is scattered by a periodical structure, as shown in fig 2.6, the diffraction peak happens at the scattering angle which is dependent on the periodical length d and wavelength λ .

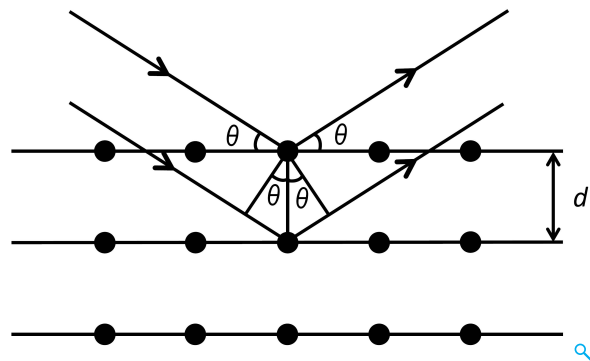


Figure 2.6: X-ray diffraction from an periodic structure with spacing of d . The corresponding scattering angle is 2θ

The phase angle difference between two scattered x-ray waves should be $2n\pi$ (n is integer).

$$2n\pi = \frac{2\pi s}{\lambda} = \frac{2\pi \times 2d \sin \theta}{\lambda} \quad (2.21)$$

where s is the path difference between two x-ray waves. Then we can get the Bragg equation

$$2d \sin \theta = n\lambda \quad (2.22)$$

We combine the equation (2.5) and equation (2.22), then we get the relation between scattering vector and the periodical space.

$$d = \frac{2\pi}{q} \quad (2.23)$$

2.2.5 Miller index

A crystal lattice can be described with three vectors **a**, **b**, **c** as shown in Figure 2.7 and three angles α (intersection angle between **b** and **c**), β (intersection angle between **a** and **c**), γ (intersection angle between **a** and **b**). A crystal lattice contains many crystal planes. The miller index is used to describe the crystal planes of the lattice and is written as (hkl). Taking

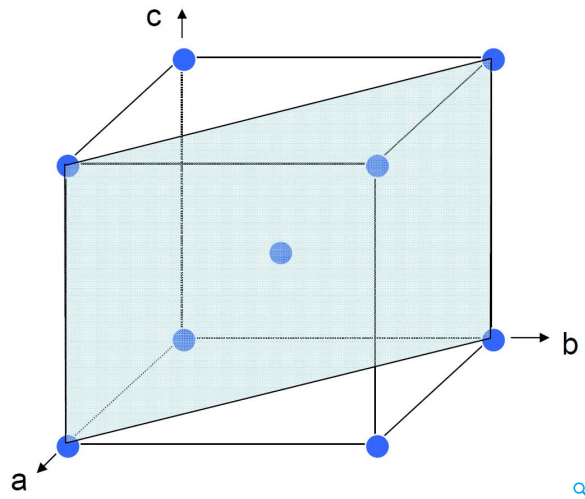


Figure 2.7: Crystal lattice of a bcc structure.

the crystal plane (blue) in Figure 2.7 as an example, the Miller index of a crystal plane can be determined by the following way: Firstly, get the intersection of the plane with a-axis, b-axis and c-axis. The unit of the intersection is the length of the vectors. So we can get the intersection of 1, 1 and ∞ . Secondly, take the lowest terms of the reciprocals of the intersections: 1, 1 and 0. Then the Miller index of the plan can be represented by (110).

The Miller index (hkl) includes not only one plane but a series of parallel planes and the near planes have the same distance d .

The plane distance d for Miller index (hkl) in the cubic lattice can be represented by

$$d_{hkl} = \frac{a}{\sqrt{h^2 + k^2 + l^2}} \quad (2.24)$$

2.2.6 Reciprocal lattice

Reciprocal lattice is an fundamental concept in crystallography. Similar as the crystal lattice, the reciprocal lattice can be represented by three vectors \mathbf{a}^* , \mathbf{b}^* , \mathbf{c}^* .

\mathbf{a}^* is perpendicular to the vectors of \mathbf{b} and \mathbf{c} in the crystal lattice and $\mathbf{a}\mathbf{a}^* = 1$. \mathbf{b}^* is perpendicular to the vectors of \mathbf{a} and \mathbf{c} in the crystal lattice and $\mathbf{b}\mathbf{b}^* = 1$. \mathbf{c}^* is perpendicular to the vectors of \mathbf{a} and \mathbf{b} in the crystal lattice and $\mathbf{c}\mathbf{c}^* = 1$.

As shown in Figure 2.8, a vector of \mathbf{c}^* in the reciprocal lattice is perpendicular to the plane of \mathbf{a} \mathbf{b} .

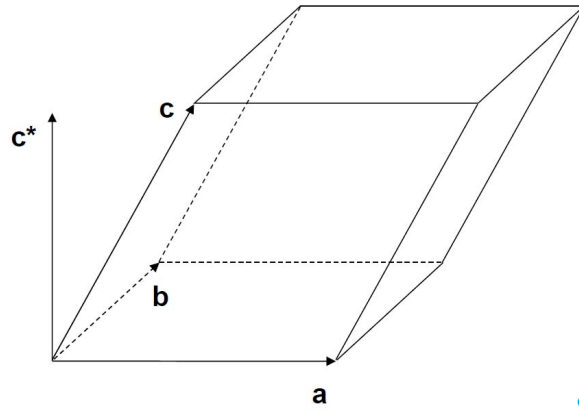


Figure 2.8: The crystal lattice and the lattice vectors \mathbf{a} , \mathbf{b} and \mathbf{c} and the corresponding vectors \mathbf{c}^* in the reciprocal lattice.

The volume of the unit cell in reciprocal lattice can be represented by

$$V^* = \mathbf{a}^* \cdot (\mathbf{b}^* \times \mathbf{c}^*) = \frac{1}{\mathbf{a} \cdot (\mathbf{b} \times \mathbf{c})} = \frac{1}{V} \quad (2.25)$$

The vector \mathbf{r}_{hkl}^* in reciprocal lattice is normal to the plane with Miller index (hkl) of the crystal lattice.

The vector $\mathbf{r}_{hkl}^* = h\mathbf{a}^* + k\mathbf{b}^* + l\mathbf{c}^*$ in reciprocal lattice is normal to the plane with miller index (hkl) of the crystal lattice and $|\mathbf{r}_{hkl}^*| = |1/d_{hkl}|$.

2.3 Rheological properties of polymer melt, network and colloidal suspension

2.3.1 Basic knowledge

Rheology is used to study the deformation and flow behaviors of the viscoelastic materials. Viscosity and frequency dependent dynamic modulus are two most important parameters to represent the viscoelastic properties of polymer materials, where viscosity is used to describe the flow properties and the dynamic modulus indicates the solid properties.

Dynamic modulus

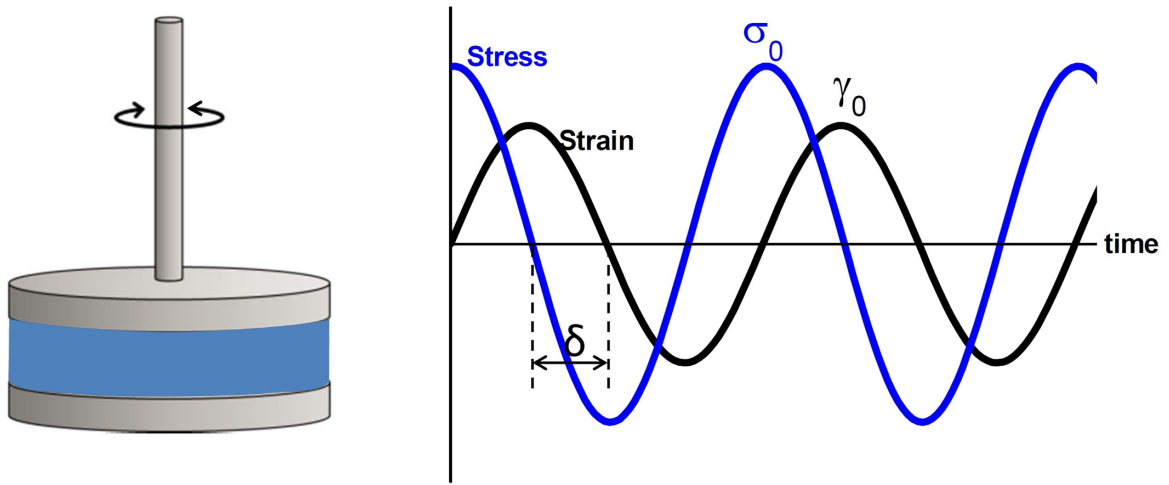


Figure 2.9: The left part is a schematic picture of the parallel plate for performing the rheological measurements. The right part is the stress/strain curve plotted against time during oscillatory measurements. The phase angle difference between stress and strain curve is δ .

In dynamic measurements, the most commonly calculated parameters are G' and G'' i.e. the storage modulus and loss modulus. Dynamic measurements are usually done to measure these two parameters. Figure 3.2 gives a schematic picture of the parallel plate geometry. A sinusoidal strain-time curve, as shown in Figure 3.2 is given to the sample with a frequency of ν or angular frequency of ω . The corresponding strain γ is

$$\gamma = \gamma_0 \sin \omega t \quad (2.26)$$

γ_0 is the strain maximum. If the viscoelastic behaviour is linear, then the stress is also sinusoidal curve.

$$\sigma = \sigma_0 \sin(\omega t + \delta) = \sigma_0 (\sin \omega t \cos \delta + \cos \omega t \sin \delta) \quad (2.27)$$

The stress curve can be decomposed into two parts with the same frequency: one is in phase with the strain curve and the other one is 90° out of phase with the strain curve.

$$\sigma = \sigma' + \sigma'' = \sigma'_0 \sin \omega t + \sigma''_0 \cos \omega t \quad (2.28)$$

where

$$\tan \delta = \frac{\sigma''_0}{\sigma'_0} \quad (2.29)$$

Then the modulus has also two parts,

$$G' = \frac{\sigma'_0}{\gamma_0} \quad (2.30)$$

$$G'' = \frac{\sigma_0''}{\gamma_0} \quad (2.31)$$

If we compare equation (2.27) and equation (2.28), we will get

$$\sigma_0' = \sigma_0 \cos \delta \quad (2.32)$$

$$\sigma_0'' = \sigma_0 \sin \delta \quad (2.33)$$

then the modulus can be given by:

$$G' = \frac{\sigma_0'}{\gamma_0} = \frac{\sigma_0}{\gamma_0} \cos \delta \quad (2.34)$$

$$G'' = \frac{\sigma_0''}{\gamma_0} = \frac{\sigma_0}{\gamma_0} \sin \delta \quad (2.35)$$

$$G^* = G' + iG'' = \frac{\sigma_0}{\gamma_0} (\cos \delta + i \sin \delta) \quad (2.36)$$

Maxwell model

The Maxwell model is a simple and widely used model to describe the viscoelastic properties of materials. The model includes a purely viscous damper with viscosity of η and a purely elastic spring with a elastic modulus of E and they are connected in series. The **scheme** of Maxwell model is shown in Figure 2.10.

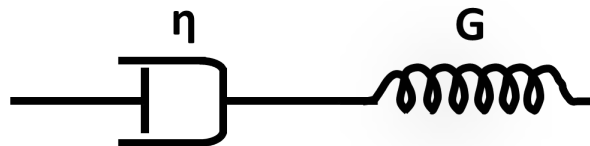


Figure 2.10: The scheme of Maxwell fluid model.

If a constant shear strain γ_0 is applied to such a Maxwell material, the applied stress σ decreases with time. Assume the stress at time 0 is σ_0 , $\sigma = \sigma_0 \exp(-tE/\eta)$ The characteristic time to describe the stress relaxation is the the relaxation time τ , which can be represented by η/E .

The storage and loss modulus curves for such a Maxwell material can be represented by

$$G'(\omega) = G\omega^2\tau^2/(1 + \omega^2\tau^2) \quad (2.37)$$

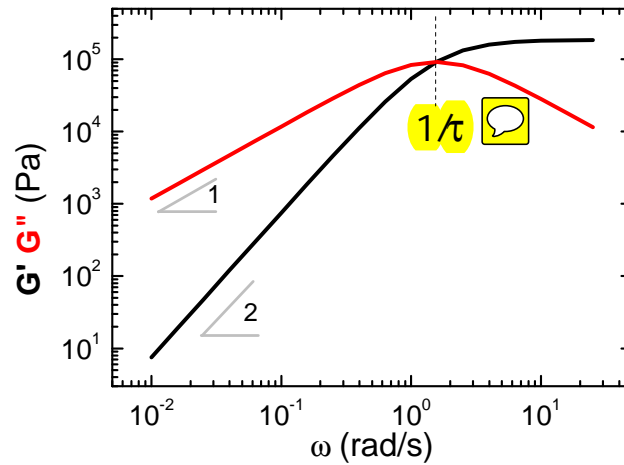


Figure 2.11: The modulus curves of the Maxwell fluid model.

$$G''(\omega) = G\omega\tau/(1 + \omega^2\tau^2) \quad (2.38)$$

When $\omega\tau \ll 1$, $G'(\omega)$ is proportional to ω^2 and $G''(\omega)$ is proportional to ω . At the crossover point of G' and G'' , the corresponding frequency is equal to $1/\tau$.

Relaxation spectrum

For the normal polymer melt with broad distribution of molecular weight, single Maxwell fluid model is not enough to describe the modulus curves. Multi-mode Maxwell model with a series of H_i and τ_i (where H_i represents the weight of the corresponding relaxation time τ_i) or a continuous function $H(\tau)$ [51] is needed. For such a multi-mode Maxwell model, the relaxation time shows a distribution.

$$G'(\omega) = \sum_{i=1}^n H_i \omega^2 \tau_i^2 / (1 + \omega^2 \tau_i^2) \quad (2.39)$$

$$G''(\omega) = \sum_{i=1}^n H_i \omega \tau_i / (1 + \omega^2 \tau_i^2) \quad (2.40)$$

From the curves of $G'(\omega)$ and $G''(\omega)$, the discrete spectrum of $H_i(\tau_i)$ can be calculated.

Master curve construction

To understand the mechanical properties of polymer materials at different time scales, complex modulus with a broad range of frequencies needs to be measured. Due to the limitation of angular frequency (the speed of the motor) and the time limitation for measurements, normally the dynamic modulus can only be measured at a limited frequency range from 0.01

rad/s to 100 rad/s. To get the modulus curve at a broad frequency range (broad time range), time-temperature superposition principle is a commonly used method.

For the non-crystalline amorphous polymer above glass transition temperature, the modulus curve measured at lower temperature has the same shape over frequency as that measured at higher temperature. They are only shifted on the frequency scale. So the modulus curve at the frequency range that is not able to be measured experimentally can be obtained by shifting the modulus curve measured at different temperatures.

$$G^*(T, \omega) = G^*(T_0, a_T \omega) \quad (2.41)$$

where a_T is the shift factors along the frequency axis.

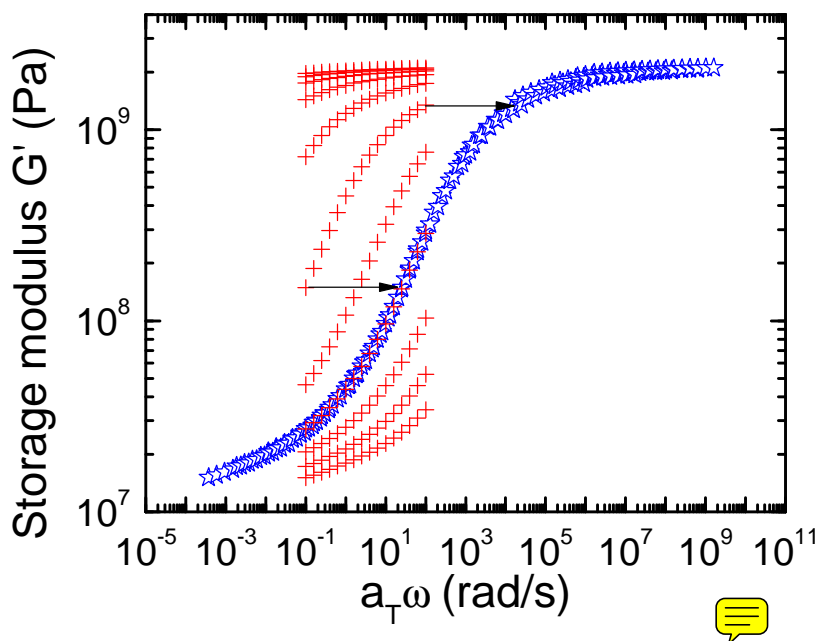


Figure 2.12: An example master curve construction of a crosslinked SBR sample measured by our own. The red symbols are original values measured at different temperatures and the blue symbols are the master curve constructed from the original data.

Figure 2.12 shows an example of master curve construction of a crosslinked styrene-butadiene rubber (SBR). The red symbols at the range of 0.1 rad/s to 100 rad/s are measured data at different temperatures, and the broad data curve in blue at the frequency range from 10^{-4} to 10^{10} rad/s is the master curve.

The relation between shift factors a_T and temperature can be described with an empirical relation Williams-Landel-Ferry Equation (WLF equation) [1]

$$\log(a_T) = \frac{-C_1(T - T_r)}{C_2 + (T - T_r)} \quad (2.42)$$

where T_r is a reference temperature and C_1 , C_2 are empirical constants depending on the polymer material.

Steady shear measurements

Steady shear measurements is a very basic method to measure the viscosity of a liquid sample. By shearing the liquid sample with a constant shear rate $\dot{\gamma}$, the shear stress σ can be measured. The viscosity is calculated by

$$\eta = \frac{\sigma}{\dot{\gamma}} \quad (2.43)$$

2.3.2 Rheological properties of polymer melt

For a homopolymer melt, the viscosity has such relation with the molecular weight as shown in Figure 2.13.

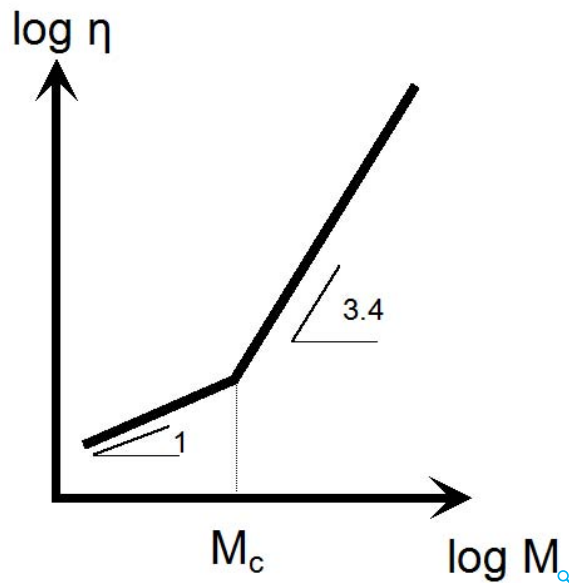



Figure 2.13: Viscosity of polymer melt vs. the molecular weight. Two regimes are observed, with the boundary at $M = M_c$. 

When the molecular weight is below M_c , the viscosity is proportional to the molecular weight. When the molecular weight is above M_c , the viscosity is proportional to the 3.4th power of molecular weight. M_c is the critical molecular weight for entanglement, around twice as much as the entanglement molecular weight M_e .

Unentangled polymer melt

The dynamics of unentangled polymer melt can be described by Rouse model [1]. In Rouse model, the polymer chains are taken as a string of beads connected by springs one by one.

The friction coefficient of each bead is ζ and the friction of each bead is independent with each other. So the whole friction of each Rouse chain is the sum of the friction of all the beads.

$$\zeta_R = N\zeta \quad (2.44)$$

where N is the number of beads in the Rouse chain.

The diffusion coefficient of the Rouse chain can be obtained with Einstein equation

$$D_R = \frac{kT}{\zeta_R} = \frac{kT}{N\zeta} \quad (2.45)$$

where k is Boltzmann constant and T is absolute temperature.

The characteristic time for a polymer chain to diffuse over the distance of its size is called Rouse time τ_R

$$\tau_R = \frac{R^2}{6\pi^2 D_R} = \frac{\zeta}{6\pi^2 kT} NR^2 \quad (2.46)$$

where R is the size of the Rouse chain.

Take the Rouse chain also as an ideal Gaussian chain, then

$$R \approx bN^{1/2} \quad (2.47)$$

where b is the size of a Kuhn segment.

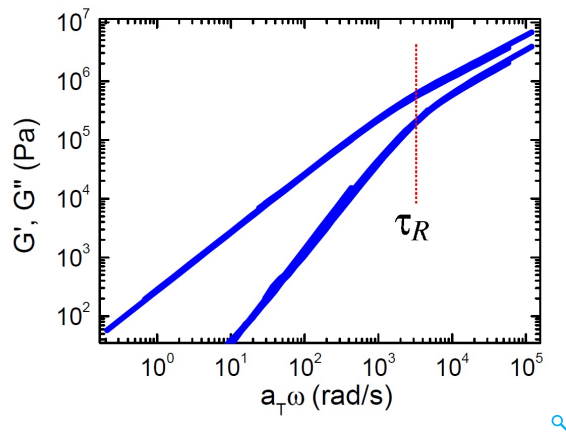


Figure 2.14: Master curve at 10 °C from oscillatory shear measurements at several temperatures for unentangled polymer PIB melt with molecular weight of 3.4 kg/mol. The experimental data was measured by our own. The upper curve is G'' and the lower curve is G' .

So the Rouse relaxation time is then

$$\tau_R = \frac{\zeta b^2}{6\pi^2 kT} N^2 = \tau_0 N^2 \quad (2.48)$$

where

$$\tau_0 = \frac{\zeta b^2}{6\pi^2 kT} \quad (2.49)$$

The Rouse relaxation time is proportional to the 2nd power of number of Kuhn segments.

Figure 2.14 shows the modulus master curves of an unentangled polymer melt. At lower frequency, the sample shows terminal flow behaviour while at higher frequency range, the Rouse relaxation is involved.

Entangled polymer melt

Figure 2.15 shows the complex modulus master curve of highly entangled 1,4-polybutadiene (PBD) with a reference temperature of 25 °C [52]. We can separate the frequency dependence of the rheological properties into three parts.

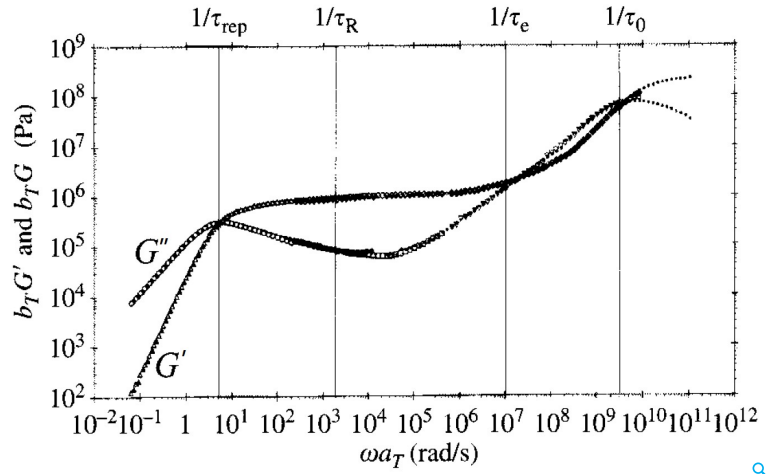


Figure 2.15: Master curve at 25°C from oscillatory shear measurements at several temperatures for 1,4-polybutadiene sample ($M_n = 130000$ g/mol) [52].

At very high frequency $\omega > 1/\tau_0$ (corresponding to low temperature), the polymer is in glassy state. At such shear frequency, the polymer is frozen, and there is no relaxation process. τ_0 is the relaxation time of Kuhn monomers.

$$\tau_0 = \frac{\zeta b^2}{6\pi^2 kT} \quad (2.50)$$

where ζ is the friction coefficient, b is the Kuhn length.

When $1/\tau_e < \omega < 1/\tau_0$, the Rouse relaxation of Kuhn units is involved. where τ_e is called the Rouse relaxation time of an entanglement strand.

$$\tau_e = \tau_0 \left(\frac{M_e}{M_0} \right)^2 \quad (2.51)$$

where M_0 is the molecular weight of Kuhn segment. When ω is smaller than $1/\tau_e$, the Rouse relaxation time of the entangled strand is also involved, the modulus goes into the plateau

region. The rouse relaxation process of entangled polymer strand is possible while disentanglement is not possible. This would lead to the effect that the sample is like a network where the junction points are very stable and the strand is free to move. In this process, the storage modulus is nearly flat and can be expressed in the following equation:

$$G_e = G(\tau_e) = \frac{kT}{\mu_0 N_e} = \frac{\rho kT}{M_e} \quad (2.52)$$

where μ_0 is the volume of a Kuhn segment.

When ω is lower than $1/\tau_{rep}$ (τ_{rep} is the disentanglement time of the whole chain), the whole chain has enough time to disentangle and the sample can flow.

$$\tau_{rep} = 6\tau_0 \frac{N^3}{N_e} = 6\tau_e \left(\frac{N}{N_e}\right)^3 = 6\tau_R \frac{N}{N_e} \quad (2.53)$$

In the modulus curves, the slope of $\log G'$ and $\log G''$ v.s. $\log \omega$ are 2 and 1 individually. The storage and loss modulus curve can be described with the Maxwell model, which was described before.

2.3.3 Rheological properties of dynamic network and critical gel

Dynamic network

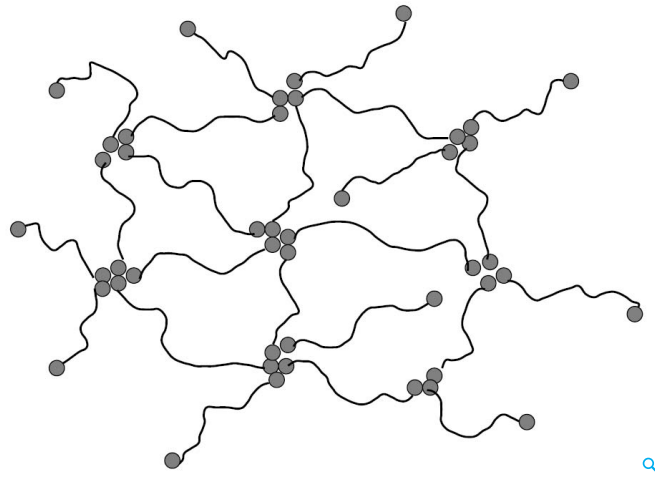


Figure 2.16: Model network made up of polymer chains with sticky end groups.

Polymers with attractive end blocks (groups) have drawn increasing attention due to the association of end blocks and formation of dynamic network and thus also the potential applications. Such polymers can be called associative polymer and they include amphiphilic polymers, asymmetric triblock copolymers and hydrogen bonding group functionalized polymers.

Such dynamic interaction is relatively weak and the activation energy to break such interaction is around $10-50 kT$ (k is Boltzmann constant) [9]. By tuning the temperature, the fraction of associated bonds and disassociation can be changed. The lifetime of the dynamic

bonding is in the range of around microseconds to thousand-seconds, which is also in the time range of experimental observation.

At short time scale, there is not enough time for the relaxation of physical cross-link network and the dynamic network behaves like a rubber, as shown in Figure 2.16.

With increasing time, the relaxation of the end groups is possible when t is equivalent to τ_i (the time of a single end group detached from the association state). With time further increasing, the dynamic network starts to flow when t reaches the longest relaxation time τ_d .

Critical gel

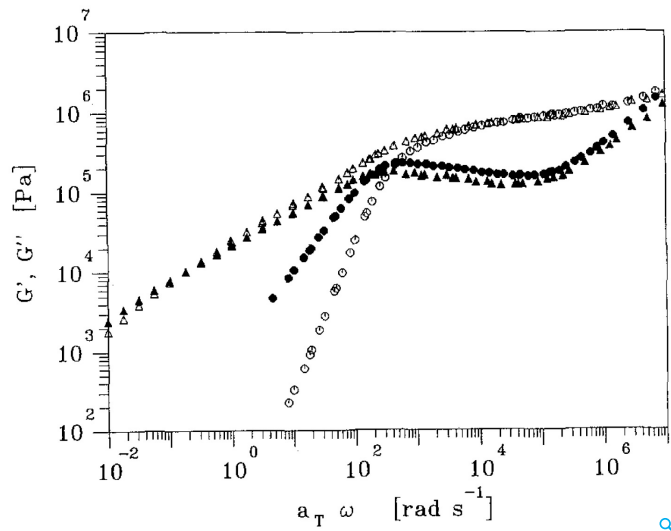


Figure 2.17: Comparison between the master curves of polybutadiene critical gel ($G' \triangle G'' \blacktriangle$) and the uncrosslinked diluted polybutadiene ($G' \circ; G'' \bullet$) [53].

When the polymer melt is partially cross-linked with chemical bonding, an intermediate state between liquid and solid can be observed at some point, and called critical gel.

Figure 2.17 shows the master curve comparison between the critical gel and polymer melt [53]. For the critical gel, the terminal flow behaviour is not observed while parallel G' and G'' curves are the characteristics.

At the gel point,

$$G'(\omega) \propto \omega^m \quad (2.54)$$

$$G''(\omega) \propto \omega^n \quad (2.55)$$

m and n are nearly the same.

2.3.4 Rheological properties of colloidal suspensions

Asymmetric block copolymers could form micellar aggregates which resembles the colloidal suspension system. The rheological properties of the micellar aggregates can be described

with the widely studied colloidal suspension system. Colloidal suspensions consist of colloidal particles with size of typically smaller than $1\mu\text{m}$, suspended in a liquid. Colloidal suspensions not only have important applications in industrial products such as foods, coatings, paints, papers and so on, but also can be used as model system of effective molecules.

The properties of a colloidal suspension depend strongly on the concentration (volume fraction) of colloidal spheres [54]. When the concentration is very low, the colloidal suspension is like a liquid and the viscosity increases with the concentration of colloidal spheres linearly. When the concentration is higher, the interaction between the spheres starts play a role and the mobility of the spheres is not as high as in very dilute suspension. At even higher concentration, the colloidal particles are localized in either equilibrium crystalline state or in metastable jammed/glassy state.

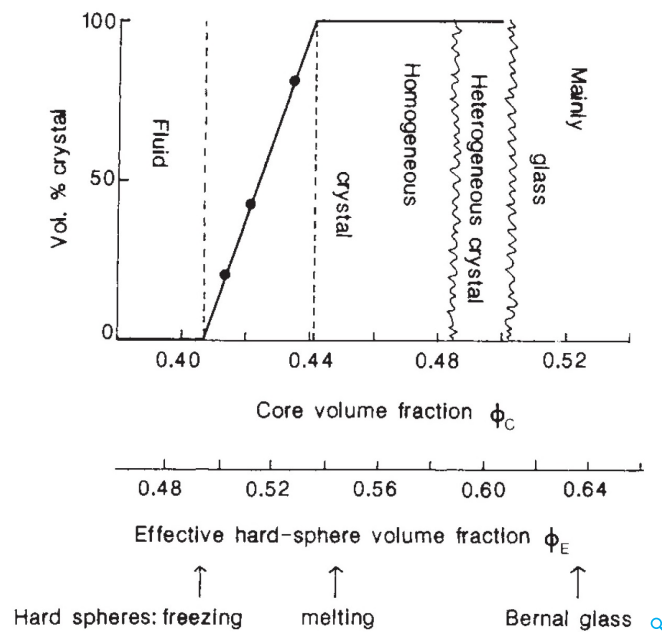


Figure 2.18: Phase diagram of colloidal suspension. [55]

Pusey and Megen [55] experimentally measured the phase diagram of the colloidal suspension as a function of the concentration of colloidal spheres, as shown in Figure 2.18. When the volume fraction of colloidal spheres is below 0.494, the system is a fluid. When the volume fraction of colloidal spheres is above 0.494, the crystal starts to appear and the content of crystal increases with increasing volume fraction of colloidal spheres. At the volume fraction of 0.536, all of the colloidal spheres form homogeneous crystals. Above the volume fraction of 0.59, heterogeneous crystal is observed instead of homogeneous crystal. At even higher volume fraction of colloidal spheres, the glass is formed.


For low concentration, Einstein gave the relation between the viscosity and volume fraction ϕ of colloidal spheres

$$\eta = \eta_0 [1 + 2.5\phi] \quad (2.56)$$

where η is the viscosity of colloidal sphere suspension with a volume fraction of ϕ , and η_0

is the viscosity of the solvent. For high concentration [54, 56], there are several empirical relations between the viscosity and the volume fraction of colloidal spheres: the Krieger-Dougherty equation

$$\eta = \eta_0(1 - \phi/\phi_m)^{-2.5\phi_m} \quad (2.57)$$

where η is the viscosity of colloidal sphere suspension with a volume fraction of ϕ ; η_0 is the viscosity of the solvent; ϕ_m is volume fraction at maximum packing. and Brady gave the equation of 

$$\eta = 1.3\eta_0(1 - \phi/\phi_m)^{-2} \quad (2.58)$$

where where η is the viscosity of colloidal sphere suspension with a volume fraction of ϕ ; ϕ_m is volume fraction at the maximum packing. Both of the equations were widely used to describe the relation between viscosity and volume fraction of colloidal spheres in the colloidal suspension.

2.4 Nonlinear rheology

Nonlinear rheological properties, like creep, fracture, breakage and fatigue are very important physical properties in selecting the materials for application. At the same time, they are also more complicated than the linear rheological properties. To have an idea about the nonlinear rheology, we will give a brief introduction into the non-Newtonian fluid, shear yielding and stress relaxation after a large strain.

2.4.1 Strain sweep in oscillatory shear measurement

For polymer melt, storage modulus, loss modulus and the complex viscosity can be measured through SAOS (small amplitude oscillatory shear) measurements. At small shear strain (γ_0), the structure of materials is not perturbed and the measured modulus doesn't change with the shear strain which corresponds to the linear region. At higher shear strain, the measured modulus may decrease with increasing shear strain, which denotes the nonlinear region. With such measurements, the shear strain can be selected for the SAOS measurements.

2.4.2 Startup shear

Beside the nonlinear rheological behavior of polymer melts at higher shear rates represented by viscosity-shear rate plot and the large strain sweep in oscillatory measurements, startup shear is another way to describe the nonlinear rheological properties of polymer melt and networks.

Startup shear measurements were done by shearing the sample with a strain at a constant shear rate. The experiments can be described in the Figure 2.19. At a shear rate $\dot{\gamma}$ which is smaller than the inverse terminal relaxation time $1/\tau$ or $Wi > 1$ ($Wi = \dot{\gamma}\tau$), shear stress **increase**

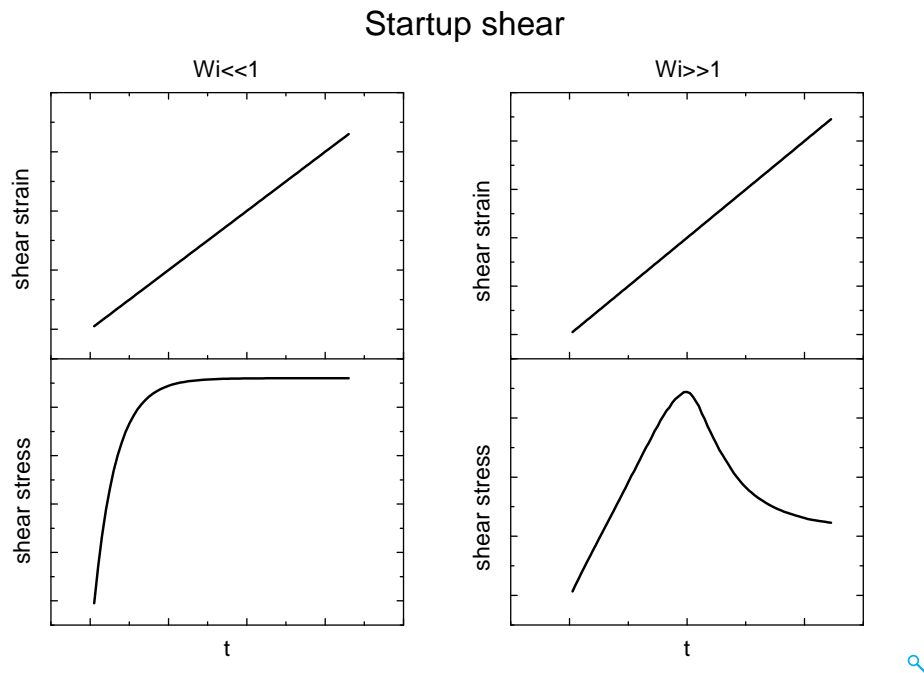


Figure 2.19: Startup shear measurements: shear strain increase linearly with time. For $Wi \ll 1$, shear stress increases with time and approaches constant value; for $Wi \gg 1$, shear stress first increases with time and then decreases.

with time and **approach** a constant stress value, which is characteristic of a fluid. For a Maxwell fluid, shear stress increases with time following the equation below:

$$\sigma = \eta \dot{\gamma} \left(1 - \exp\left(-\frac{G}{\eta} t\right) \right) \quad (2.59)$$

where σ is shear stress; η is viscosity; $\dot{\gamma}$ is shear rate; G is the plateau modulus; t is time.

At a shear rate which is larger than the inverse of the terminal relaxation time, a stress overshoot happens and the shear stress shows a maximum, which is also called shear yielding.

Entangled polymer melts and dynamic polymer networks both can show shear yielding behaviour at certain conditions. Figure 2.19 gives an example of shear yielding behaviour of the dynamic network formed by telechelic polymers. Shear yielding behaviour happens at high shear rate when $Wi > 1$ ($Wi = \dot{\gamma}\tau$ and τ is the terminal relaxation time). In the shear stress-shear strain curve, at high shear rate, shear stress increases linearly with shear strain in the beginning, and then start to drop at high strain till the shear stress comes to a plateau. The drop of shear stress from the peak point means the fracture of the network, which was observed through particle image velocimetry (PIV) [57].

Shear yielding in different systems can be due to different mechanisms and is not well-understood yet.

2.4.3 Stress relaxation at large step strain

The stress relaxation experiments were performed by measuring the time dependent shear stress with keeping the strain constant after a startup shear measurements.

For an entanglement network, when step shears with different strains are applied, different relaxation processes can happen.

At small step strain, the relaxation process (the top lines as shown in Figure 2.20) can be described with the following equation,

$$G_p(t, s) = G_p(0, s) \exp(-(t/\tau)^\alpha) \quad (2.60)$$

where $G_p(0, s)$ is the reduced relaxation modulus measured at time 0, τ is the relaxation time, α is the stretched exponent. Depending on the broadness of relaxation time distribution, α varies from 0 to 1. $G_p(t, s)$ is the reduced relaxation modulus measured at time t after a shear strain of s , defined as

$$G_p(t, s) = G(t, s) \rho_0 T_0 / \rho T \quad (2.61)$$

where $G(t, s)$ is the relaxation modulus, ρ is the density, T is the absolute temperature, ρ_0 is the density at the reference temperature T_0 . While at high step strain, the relaxation

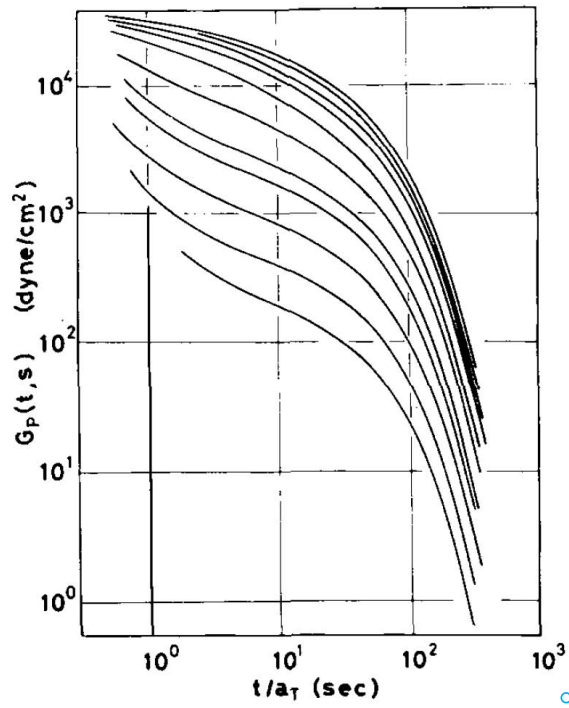


Figure 2.20: Reduced relaxation modulus $G_p(t, s)$ plotted against reduced time t/a_T for a polystyrene solution. The given shear strain increase from top to bottom lines (0.166, 0.222, 0.444, 1.11, 1.88, 3.34, 5.22, 6.68, 10.0, 15.3, and 20.5). [58]

process (the bottom lines as shown in Figure 2.20) shows a fast process followed by a normal relaxation process. It is suggested that the fast relaxation is due to the nonlinear rheological properties of the entanglement network.

Chapter 3

Experimental methods

In this chapter, we describe experimental methods that we used for our study. They are mainly the small angle X-ray scattering (SAXS) and rheology.

3.1 Small angle X-ray scattering

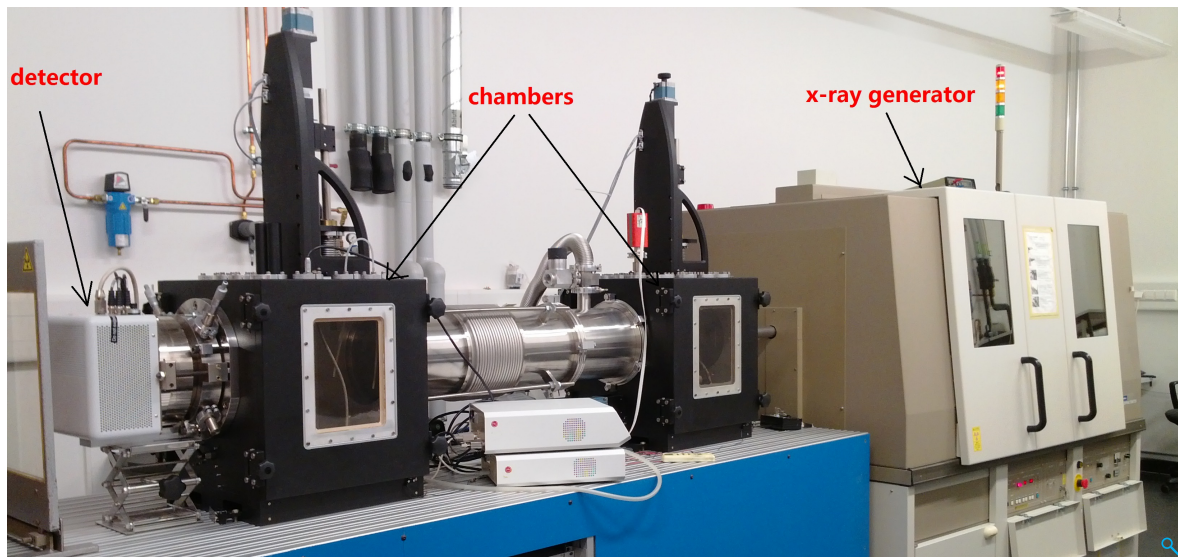


Figure 3.1: SAXS instrument in our group. From right to left: the x-ray generator (rotating anode), two sample chambers, and the X-ray detector.

Figure 3.1 shows the X-ray scattering machine used in our group. Visibly, there are mainly three parts: the X-ray generator part (the rotating anode), the measurement chambers, and the detector. The X-ray generator part produces the X-ray beam. With the help of optics and pinholes, the X-ray beam will be modified to small sized, collimated beam with narrow range of wavelength. The collimated X-ray beam then irradiates the sample and is scattered onto the detector.

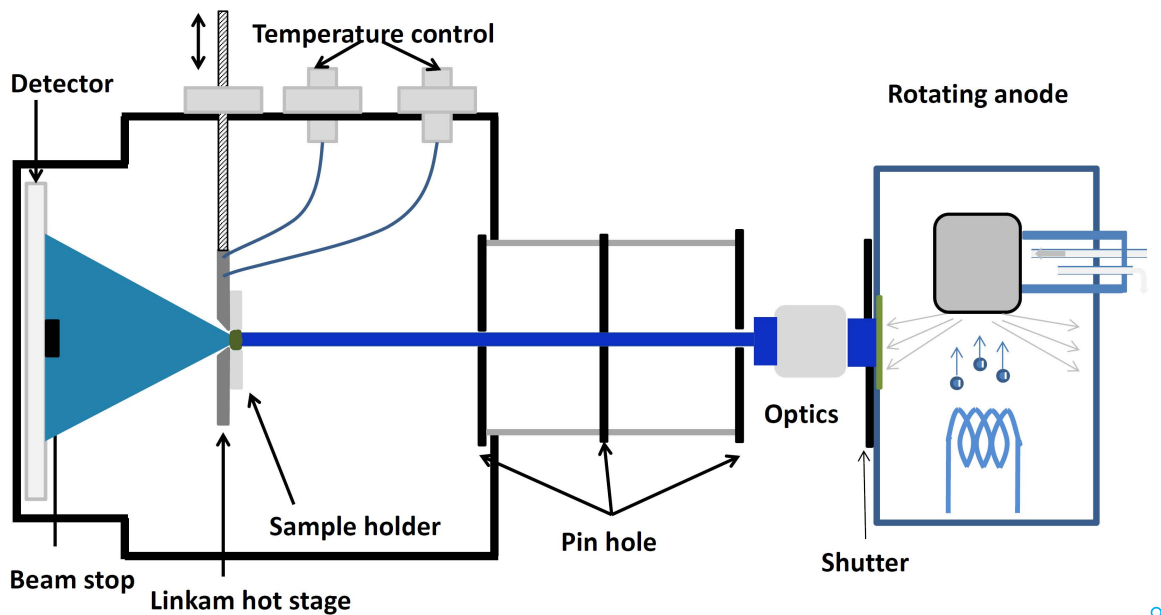


Figure 3.2: Structure of the SAXS instrument.

While the SAXS machine is much complicated and the whole structure can be shown in Figure 3.2. From the right side to the left, there are the **x-ray** generator, the pinholes, sample chamber, and the detector.

Inside the X-ray generator, there is a cathode which is made of tungsten filament and it is heated with applied current of 1 A. With the high temperature of 2000°C, the electrons are emitted from the hot filament, accelerated with the electric field applied between the cathode and anode and fly to the copper anode. The applied voltage between the cathode and anode is 40 kV and the current by the electrons is around 60 mA. The electrons with high speed hit the copper anode and the X-ray beam is then radiated from the anode. Only a small amount of incident electron energy converts into X-ray beam, and most of them convert into heat. To avoid the overheating of the anode a cooling system is needed. In the cooling system, the water flows inside the rotating anode.

The generated X-ray beam then passes the beryllium window and the shutter and exits from the rotating anode. The custom Confocal Max-Flux optics is an optic module which can make the X-ray beam collimated and monochromatic (Cu, 0.154 nm). The X-ray beam then passes through three pinholes to get collimated and small-sized. The first two pinholes with an aperture diameter of around 0.4 mm and 0.2 mm are used to reduce the X-ray beam divergence. The third pinhole with an aperture diameter of 0.7 mm is near to the sample chamber and is used to remove the parasitic radiation caused from the second pinhole. We have two sample chambers with distances of around 157 cm and 30 cm from the detector. The corresponding q vector range that can be measured in the two chambers is 0.01-0.15 / Å and 0.05-0.6 / Å.

Then the X-ray beam irradiates on the sample and is scattered onto the detector. The sample is placed in the hole of an aluminum plate. The aluminum plate with the sample

is attached onto a Linkam hot stage with thermal conductive paste. The temperature of the sample can be controlled by the Linkam hot stage. With the help of liquid nitrogen, the controlled temperature range is $-40\text{ }^{\circ}\text{C}$ to $300\text{ }^{\circ}\text{C}$. With the detector Bruker Hi-Star, 2-D SAXS pattern can be obtained. Through the processing software (SAXSGUI) and with the calibration of the standard sample silver behenate, the 2-D SAXS pattern can be converted into I vs. q .

3.2 Rheology

3.2.1 Introduction of the rheometer

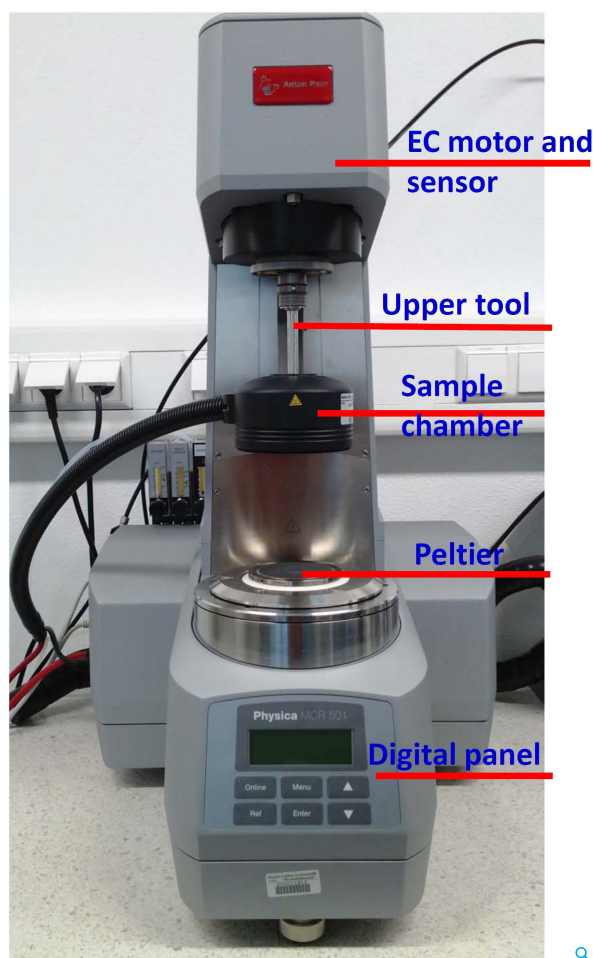


Figure 3.3: The picture of Anton Paar rheometer MCR 501. The rheometer mainly contains the following parts: (from top to bottom) the EC motor and sensor part, the upper tool, the sample chamber, Peltier and Digital panel. The sample chamber is shown open.

The rheometer that we used for our study is the Anton Paar MCR 501, as shown in Figure 3.3. The sample is placed in between the Peltier and the upper tool and enclosed in the sample

chamber. The temperature is controlled by Peltier and the nitrogen gas flow circulated inside the sample chamber to make the temperature distribution of sample uniform. With the Peltier, the sample can be heated up to the temperature of 200°C and cooled to -40°C. The upper tool can be plate or cone with different radius depending on the purpose of study. In the upper part of the rheometer, it includes the EC motor which rotates the upper tool and the sensor which could measure the deformation applied on the sample. The motor has a torque range from 0.05 to 200000 μNm . Different kinds of experiments can be done with the instrument: steady shear measurements, dynamic shear measurements, time-dependent measurements, etc. For steady shear measurements, the shear rate range is normally between 0.001 to 100 s^{-1} . For the dynamic shear measurements, the angular frequency is in the range of 0.001 to 100 rad/s .

3.3 Infrared spectroscopy

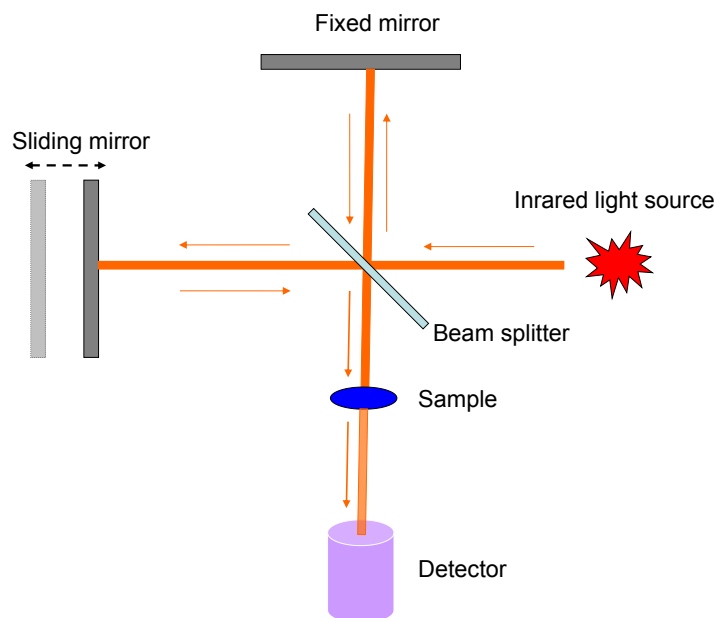


Figure 3.4: Fourier transform infrared spectroscopy (FTIR).

Infrared spectroscopy is a technique to obtain the infrared spectrum of materials. By analysing the infrared spectrum, the chemical groups inside the sample can be detected.

The technique used to measure the infrared spectrum is the Fourier transform infrared spectroscopy (FTIR). The infrared spectrometer that we used is Tensor 37 from Bruker.

When an infrared beam with broad wave number shines on the sample, the vibrational modes of the chemical bonds can be activated to a higher level by absorbing infrared beam with certain energy. The transmitted infrared beam thus shows an absorption peak.

The structure of the infrared spectrometer is shown in Figure 3.4. The infrared light source produces infrared beam and then the beam splitter splits the infrared beam into the transmitted beam and the reflected beam. The two beams will be transmitted to two mirrors (Michelson interferometer). One mirror is fixed and the other is moving. As the sliding mirror moves, the infrared beam with certain wavelength can be interfered and is blocked and transmitted and absorbed by the sample. The detector get a series of absorbing signals. By Fourier transform, the infrared absorption spectrum can be obtained.

When an infrared beam with broad wave number shines on the sample, the vibrational modes of the chemical bonds can be activated to a higher level by absorbing infrared beam with certain energy. The transmitted infrared beam thus shows an transmission peak.

The structure of the infrared spectrometer can be shown in Figure 3.4. The infrared light source produces infrared beam and then the beam splitter splits the infrared beam into the transmitted beam and the reflected beam. And then the two beams will be transmitted to two mirrors (Michelson interferometer). One mirror is fixed and the other is moving. As the sliding mirror moves, the infrared beam with certain wavelength can be interfered and is blocked and transmitted and absorbed by the sample. The detector get a series of absorbing signals. By Fourier transform, the infrared absorption spectrum can be obtained. The absorbance A is defined as

$$A = \log\left(\frac{\Phi_i}{\Phi_t}\right) = -\log T \quad (3.1)$$

where Φ_i is the radiant flux received by the materials; Φ_t is the radiant flux transmitted by the materials and T is the transmittance of the materials.

For the bulk sample measurements, the fluid samples are sandwiched between two KBr plates which have a thickness of 0.84 mm and diameter of 13 mm. For polymer solutions measurements, the polymers were dissolved into chloroform and the concentration were around 0.01 mol/L. The polymer solutions were then filled into the liquid cells.

Chapter 4

Nanostructure and Rheology of Hydrogen-Bonding Telechelic Polymers in the Melt: From Micellar Liquids and Solids to Supramolecular Gels

As we have shown in chapter 1 that hydrogen bonding functional polymers in solution have been studied extensively [8, 10] and are relatively well understood [13, 33] while hydrogen bonding functional polymers in the bulk are more complicated and the understanding is still not clear. Quantitative studies of hydrogen bonding functional polymers in the bulk state are still rare and the correlation between chemical structures of hydrogen bonding functional polymers, morphologies at nanoscale, and rheological properties still needs to be studied.

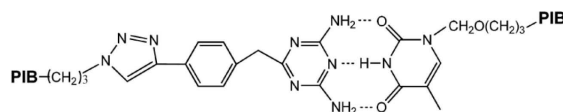
This chapter is based on our publication [59]. In this chapter, we will present our studies of a series of telechelic Polyisobutylene (PIB) samples with supramolecular hydrogen bonding groups triazine/thymine. With (semi-)quantitative analysis of SAXS and rheological data of telechelic PIB samples in the bulk, we found **four different** morphologies including ordered micelles, disordered micelles, interconnected micellar networks depending on the chemical structures of different telechelic PIB samples. The rheological properties and morphologies at nanoscale correlate with each other for all samples and they are determined mainly by the demixing tendency (between the PIB chains and the hydrogen bonding end groups) and the unspecific hydrogen bonds. In one case the effect of specific hydrogen bonding can be observed.

4.1 Samples

We have a series of telechelic PIB samples, as shown in Figure 4.1, which comprise of low-molecular weight (around 3.5 kg/mol) PIB functionalized with triazine/thymine (Tr/Th) groups at one or two ends and a homopolymer PIB with same molecular weight for comparison.

The Tr/Th groups form triple hydrogen bonding with an association constant of 10^3 M^{-1} in chloroform [32] and the self-association constants of both Tr/Tr and Th/Th are around 5

2,6-diaminotriazine (Tr) and thymine (Th) functionalized PIB



| Sample name | Schematic picture | Molecular weight (M_n in kg/mol) | PDI |
|---------------------|-------------------|-------------------------------------|---------|
| PIB | | 3.7 | 1.23 |
| Th-PIB | | 3.6 | 1.13 |
| Tr-PIB | | 3.96 | - |
| Tr-PIB+Th-PIB | | 3.96, 3.6 | -, 1.13 |
| Tr-PIB-Tr+Th-PIB-Th | | 3.7, 3.5 | -, 1.34 |

Figure 4.1: Sample information. Polydispersities ($PDI=M_w/M_n$) were obtained by GPC. The PDI of Tr-PIB sample could not be measured due to interaction with the GPC column. Additional information including synthesis methods can be obtained in reference [32]

M^{-1} . The molecular weights of PIB chains for all samples are around 3.5 kg/mol, well below the critical entanglement molecular weight ($M_c=13.1$ g/mol [60]). For the monofunctional mixture sample Tr-PIB+Th-PIB and the bifunctional mixture sample Tr-PIB-Tr+Th-PIB-Th, the mole ratios between two components in each mixture sample are 1:1 to make sure all the hydrogen bonding groups have a partner. The detailed information about the synthesis and preparation of the telechelic polymers can be found in the reference [32].

4.2 Results and Discussion

4.2.1 Analysis of the micellar superstructure of the monofunctional polymer Tr-PIB in the melt

Analysis of the scattering data in the ordered state

We start from the sample Tr-PIB which shows a well-defined ordered structure at nanoscale due to the aggregation of the hydrogen bonding end groups. Figure 4.2a shows the SAXS patterns of sample Tr-PIB measured at the temperature range from room temperature to 100 °C. Three peaks at q^* , $\sqrt{2} q^*$ and $\sqrt{3} q^*$ can be observed, indication of an ordered bcc (body-centered cubic lattice) structure. Such ordered bcc structure was observed very often in asymmetric block copolymers. In view of the chemical structure of Tr-PIB as shown in Figure 4.1, the weight fraction of the polar hydrogen bonding group (including the 2,6-diaminotriazine) is only around 7%, so the telechelic polymer Tr-PIB can be taken as an asymmetric diblock copolymer. The bcc ordered structure formation can be attributed to the microphase separation driven by the demixing between the polar hydrogen bonding groups

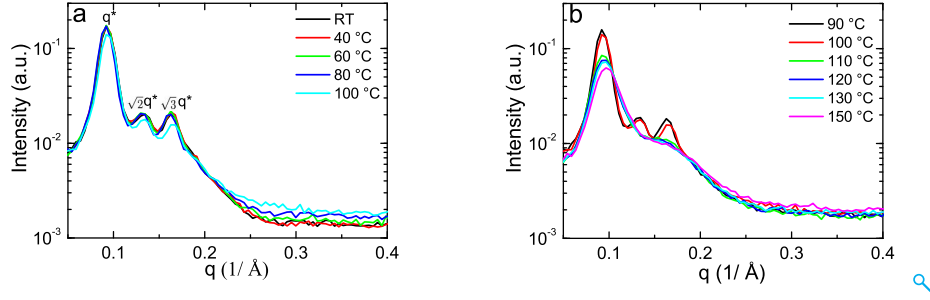


Figure 4.2: SAXS patterns of the melt of the monofunctional sample Tr-PIB. (a) Scattering intensity $I(q)$ vs. q for temperatures from room temperature to 100 °C ($q^* = 0.092 \text{ \AA}^{-1}$ at room temperature). (b) Scattering intensity $I(q)$ vs. q for temperatures around order-disorder transition temperature (110 °C).

and the nonpolar PIB chains. The minority blocks Tr aggregate and compose the micellar core while the majority blocks PIB compose the micellar corona. The high concentration of the spherical micelles makes them pack into the ordered bcc lattice. The first scattering peak at $q^* = 0.092 \text{ \AA}^{-1}$ in SAXS pattern corresponds to the lattice plane (110). The lattice parameter can be calculated by $d_{100} = d_{110} \cdot \sqrt{2} = 9.64 \text{ nm}$.

To check whether the relation between the molecular weight of the diblock copolymer and the size of the random coil in disordered state is consistent, we take use of Leibler theory [44] on microphase separation of block copolymer melts. The radius of gyration of the random coil R in disordered state can be calculated by $R = \sqrt{C}/q_0$, where C is a constant depending on the chain's composition and q_0 is the peak position in SAXS patterns from the disordered phase. Since the peak position doesn't change much during the order-disorder transition, we take q_0 to be approximate q^* from the ordered state. Since the weight fraction of one block is 7%, the corresponding C is 5.25. q^* is 0.094 \AA^{-1} at 100 °C, and the radius of gyration is calculated to be $R = \sqrt{5.25}/q^* \approx 2.44 \text{ nm}$. The radius of gyration of the PIB chains can be estimated by $R_{g,PIB} = \sqrt{Nb}/\sqrt{6} = 1.91 \text{ nm}$ (number of Kuhn segments $N = 13$, Kuhn length $b = 1.3 \text{ nm}$.) [61]. In consideration of the size of the end groups, we can see that the radius of gyration calculated by the two methods are consistent. The peak position q^* observed in the SAXS pattern of Tr-PIB in ordered state is quantitatively consistent with the assumption of a microphase separated structure.

To further analyse the SAXS data from the ordered bcc structure, we take the scattering intensity as a superposition of Bragg reflections from the bcc lattice $I_{Bragg}(q)$ and the diffuse scattering $I_{diff}(q)$ caused by spatial disorder [48]. Density fluctuations C are taken into account as a constant background.

$$I_{total}(q) = I_{Bragg}(q) + I_{diff}(q) + C \quad (4.1)$$

$$I_{Bragg}(q) = \sum_{hkl} \Phi(q_{hkl} R_1) \frac{j_{hkl}}{q^2} G_{hkl}(q; \sigma) \cdot \exp(-q_{hkl}^2 u^2 / 3) \quad (4.2)$$

$$I_{diff}(q) = \Phi(q R_1) \cdot (1 - \exp(-q^2 u^2 / 3)) \quad (4.3)$$

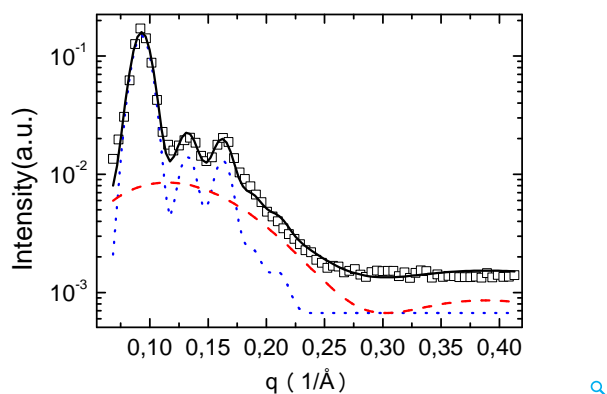


Figure 4.3: SAXS data of Tr-PIB at 25°C in the ordered state (unfilled squares) and fit curve (solid line). The diffuse scattering contribution is shown as a dashed curve in red and the Bragg diffraction contributions by the short dashed curve in blue. For a better presentation a background $C/2$ was added to both model curves (cf. equation 4.1).

$\Phi(q_{hkl}R_1)$ is the form factor of the micellar cores. R_1 is the radius of micellar cores. $G_{hkl}(q; \sigma)$ is a normalized Gaussian with center position q_{hkl} and width σ . j_{hkl} is multiplicity of the hkl reflection. u is the mean squared deviation. Figure 4.3 shows the data at 25 °C together with the fit curve. The resulting radius of the micellar core is 14.7 Å. The mean squared displacement u^2 of the micelles is about 13.5 Å².

Analysis of the scattering data in the disordered state

As it is known that the ordered state can be converted to disordered state at high temperatures for block copolymers and such transition is called order-disorder transition, similar behaviour was also observed in our telechelic polymer Tr-PIB. Figure 4.2b shows the SAXS patterns of Tr-PIB at elevated temperatures from 90 °C to 150 °C. At 110 °C, the first q peak drops significantly and the other two high order peaks disappear, indicating the order-disorder transition from the ordered bcc micelles to the disordered state. The structure recovery is possible after being cooled from 150 °C to 100 °C, meaning the transition is reversible. However, the indication of a shoulder in SAXS patterns at high temperatures suggests that it is not a disordered phase for which normally only a broad peak exists in the SAXS pattern. Rather, it might be the disordered spherical micellar structure and the shoulder represents the form factor of the spherical micelles, as reported in other asymmetric block copolymers [47, 48].

The structural transition from ordered micelles to disordered micelles is shown as a scheme in Figure 4.4. The red objects are the micellar cores formed by hydrogen bonding end groups. The green objects are the micellar corona composed of PIB chains. The grey objects are the free telechelic PIB chains.

Such a disordered micellar system can be taken as a colloidal suspension and treated with Percus-Yevick hard sphere model. The model assumes a suspension of hard spheres with repulsive interaction. The potential is infinity when two spheres touch each other. In our system, we assume the spherical micelles as hard spheres and the free telechelic polymer

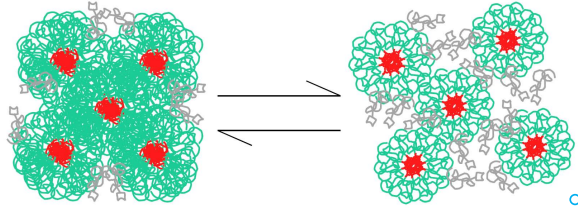


Figure 4.4: A schematic picture of the transition from an ordered to a disordered melt of micelles is shown. The red objects represent the dense core of functional groups, the green lines are the PIB corona chains and the light grey lines represent free matrix chains.

chains as the solvent. The scattering intensity of the disordered micelles can be attributed to two parts: form factor of spheres with radius of R_1 (the spherical micellar cores) and the structure factor of hard spheres (the disordered micelles) with a radius of R_2 . For the size of the spherical micellar cores, we assume a log-normal distribution. The whole scattering intensity can be represented by the following equation

$$I(q) = KS(qR_2) \int_{R_1=0}^{\infty} \Phi(qR_1) f_p(R_1, \bar{R}_1, \sigma) dR_1 + C \quad (4.4)$$

Here K is a factor depending on the electron density difference between the micellar cores and the matrix. C is a constant scattering background measured at high q . $S(qR_2)$ represents the structure factor of a system of hard spheres (spherical micelles) with radius of R_2 . $\Phi(qR_1)$ is the form factor of the spherical micellar core with a radius of R_1 . The detailed description of the form factor and structure factor are shown in chapter 2. $f_p(R_1, \bar{R}_1, \sigma)$ is the probability density function of the log normal distribution function of R_1 . \bar{R}_1 and σ are the mean value for the radius and the width of the distribution, respectively.

$$f_p(R_1, \bar{R}_1, \sigma) = \frac{1}{R_1 \sigma \sqrt{2\pi}} e^{-\frac{(\ln R_1 - \ln \bar{R}_1)^2}{2\sigma^2}} \quad (4.5)$$

Figure 4.5 shows the SAXS data (open symbols) of Tr-PIB at a series of temperatures and also the fitting curves (solid lines). Obviously, the fitting curves fit well with the experimental data well and the fitting function is successful to describe the SAXS data of the disordered state.

The fit parameters, including volume fraction of micelles (ϕ), the radius of micellar core (R_1) and the radius of micelles (R_2) can be obtained and they are plotted against temperatures as shown in Figure 4.6.

With increasing temperature, the volume fraction of micelles ϕ and the radius of micelles R_2 decrease while the radius of micellar core R_1 has a large error bar and shows no clear trend. The weakening demixing tendency between the end groups and the PIB chains at higher temperatures leads to dissolution of the micelles and thus a smaller volume fraction of micelles ϕ and a smaller radius of micelles R_2 . The trend of R_1 is not clear probably because the scattering intensity is insensitive to it, which causes a large error bar.

In the colloidal sphere suspension, one important parameter to control the phase transition is the volume fraction of colloidal spheres [55]. For Tr-PIB, at 110 °C which is around

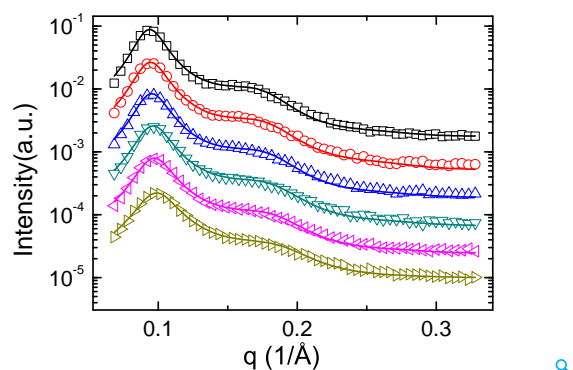


Figure 4.5: SAXS scattering data of Tr-PIB at a series of temperatures (110°C(□), 120°C(○), 130°C(△), 140°C(▽), 150°C(◁), 180°C(▷)). The data for different temperatures were shifted along the vertical direction for better visibility.

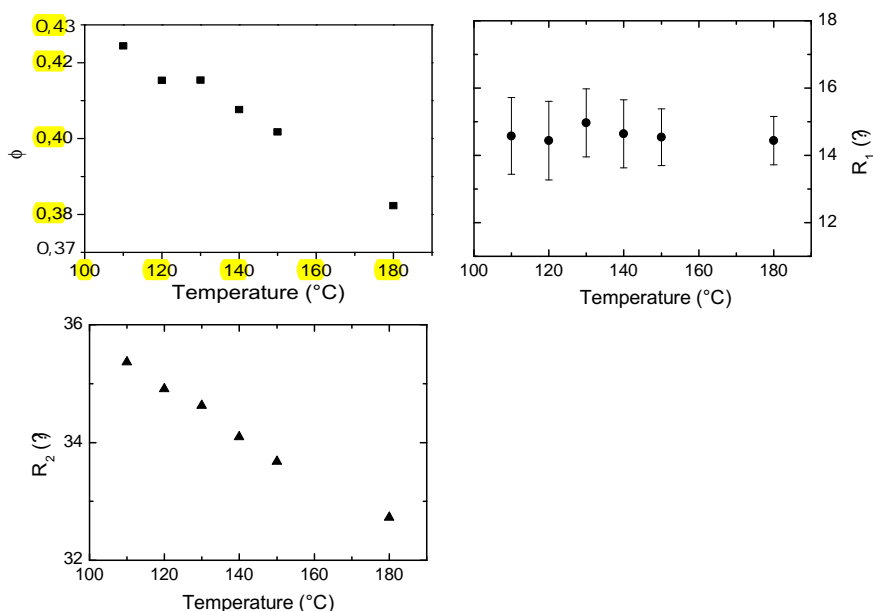


Figure 4.6: Volume fraction of micelles ϕ , radius of the micellar inner core R_1 and radius of the whole micelle R_2 in dependence on temperature for sample Tr-PIB. If not shown, the error bars are similar to symbol size.

the order-disorder transition temperature, the fit parameter ϕ is around 0.43, similar to the reported critical volume fraction of 0.494 for crystallization. The value of critical volume fraction depends sensitively on changes in the interaction between the micelles [62] or polydispersity [63]. Especially, attractive interactions decrease the critical volume concentration. All of the above facts could be the reason for a lower critical volume fraction in our system.

The aggregation number, defined as the number of end groups (telechelic chains) per

aggregate, is an important parameter to characterize the micelles. From the fit parameter R_2 , the aggregation number N can be calculated as $N = \frac{4\pi R_2^3 \rho N_A}{3M}$. Take the density of telechelic polymer melt $\rho = 0.9 \text{ g/cm}^3$ and the molecular weight of the single chain $M = 3960 \text{ g/mol}$, then N is calculated to be 25 at $110 \text{ }^\circ\text{C}$.

Analysis of the rheological data in the ordered state

From SAXS analysis we know that the sample shows ordered micelles at low temperatures and disordered micelles at high temperatures and there is a distinct order-disorder transition at around $110 \text{ }^\circ\text{C}$. Now we switch to the rheological modulus curves around $110 \text{ }^\circ\text{C}$ to see how the order-disorder transition influences the rheological properties.

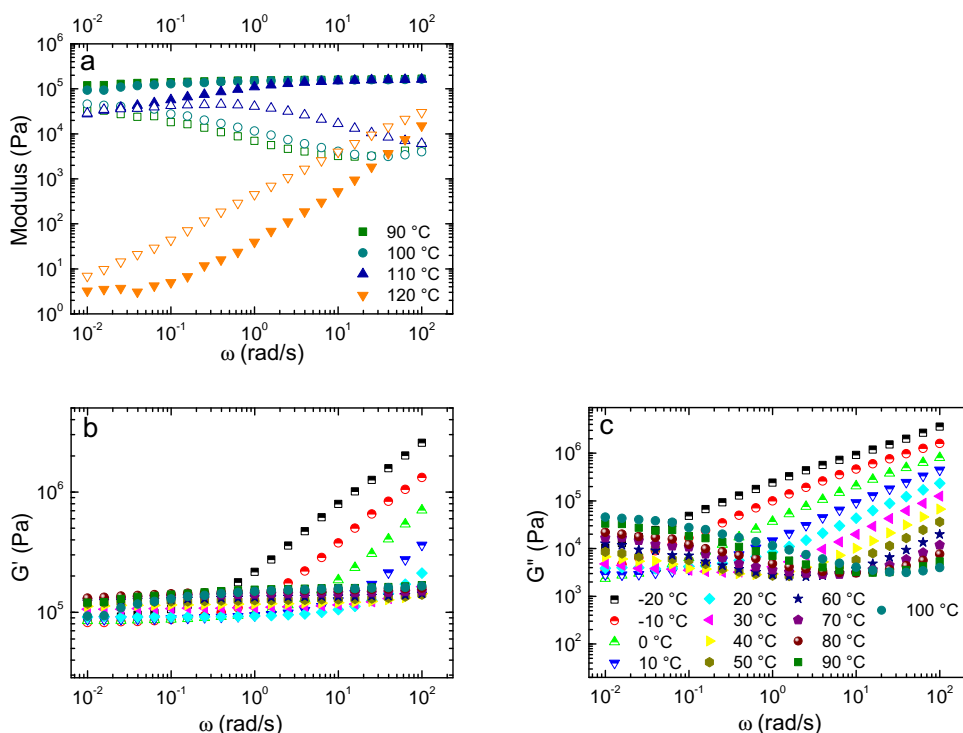


Figure 4.7: Shear modulus of Tr-PIB (a) around 110°C (closed symbols storage modulus G' , open symbols loss modulus G''), (b) storage modulus G' and (c) loss modulus G'' at lower temperatures. The symbols for the different temperatures are the same in all cases and given in part c.

As shown in Figure 4.7a, the storage modulus (filled symbols) and loss modulus (open symbols) are plotted against angular frequency. Below $110 \text{ }^\circ\text{C}$, a long storage modulus plateau can be observed, which corresponds to a solid-like structure and is consistent with the bcc-ordered micellar structure. While at $110 \text{ }^\circ\text{C}$ where the order-disorder transition happens in SAXS analysis, the storage modulus (blue symbols) decreases and terminal flow behavior can be observed at $120 \text{ }^\circ\text{C}$ (orange symbols), consistent with disordered micelles fluid.

Now we analyze the rheological data of Tr-PIB in ordered state. The storage modulus and loss modulus at a series of temperatures below 100 °C are shown individually in Figure 4.7b and Figure 4.7c. The storage modulus shows a long plateau with a plateau modulus of around 10^5 Pa. In consideration of the low molecular weight of PIB (smaller than M_e), the long storage modulus plateau can be attributed to the elastic properties of the bcc ordered structure. The spherical micelles sit on the bcc lattice and directly interact with the surrounding micelles. An elastic restoring force with entropic origin is produced due to the interpenetration of the near micellar corona [64]. It has been reported [65] that diblock copolymers with bcc ordered structure also show such elastic modulus. By systematically studying several different diblock copolymers with bcc ordered structure, an empirical relation between the storage plateau modulus G_{cubic} and the characteristic distance d^* of the bcc lattice was obtained. $\log(G_{cubic})$ is found to be a linear function of $\log(d^*)$.

By manually fitting the data in the reference, we found such a relation between $\log(G_{cubic})$ and $\log(d^*)$.

$$\log\left(\frac{G_{cubic}}{RT}\right) = (-3.14 \pm 0.36) \log(d^*) + (7.746 \mp 1) \quad (4.6)$$

Where G_{cubic} has a unit of mol/m^3 and d^* has a unit of Å.

We take the sample Tr-PIB as an asymmetric diblock copolymer and accordingly test whether the experimental data fit the equation. We take the experimental data of Tr-PIB measured at 30 °C as an example. The characteristic domain spacing can be calculated from SAXS data: $d^* = d_{110} = 68.2$ Å. The plateau modulus G_{cubic} can be calculated by substituting $d^* = 68.2$ Å into equation (4.6) as $10^{(5.37 \pm 0.33)}$ Pa (between 0.109 MPa to 0.535 MPa). The experimental plateau modulus can be taken from the experimental modulus curves as the G' value at the angular frequency where G'' shows a minimum. The obtained experimental storage modulus is found to be 0.11 MPa, lying in the calculated value range from the empirical relation. We conclude that the hydrogen bonding seems not play a role in influencing the rheological properties of the telechelic PIB sample Tr-PIB.

Analysis of the rheological data in the disordered state

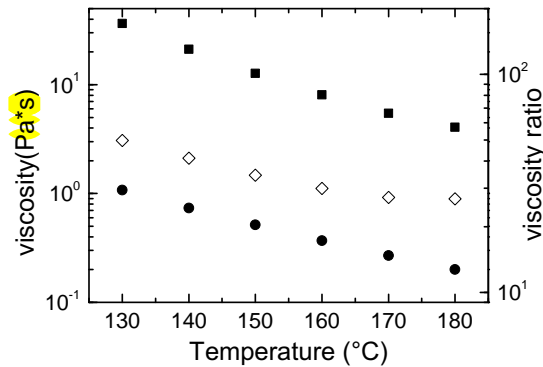


Figure 4.8: Temperature dependent viscosities of the monofunctional polymer Tr-PIB (■) and homopolymer PIB (●). The ratio between both viscosities is also given (◇).

According to the SAXS data analysis, above 110 °C, the sample shows disordered micellar structure, which can be supported by the viscosity analysis of Tr-PIB and the homopolymer PIB. Figure 4.8 shows the temperature dependent viscosities of Tr-PIB (square symbols) and homopolymer PIB (sphere symbols). Apparently, the viscosity of Tr-PIB is one to two orders of magnitude larger than the viscosity of homopolymer PIB although the homopolymer PIB has similar molecular weight to that of Tr-PIB. This is consistent with the SAXS analysis that above 110 °C Tr-PIB shows no disordered chains but disordered micellar aggregates. The viscosity ratio between Tr-PIB and homopolymer PIB is shown in Figure 4.8. It decreases with temperature, meaning the size or the volume fraction of micelles decreases with increasing temperature, also consistent with SAXS analysis.

4.2.2 Disordered phase of Th-PIB in the bulk state

Above we have shown that three samples are individually ordered micellar structure, disordered micellar structure and interconnected micellar network. Now we show the studies of sample Th-PIB.

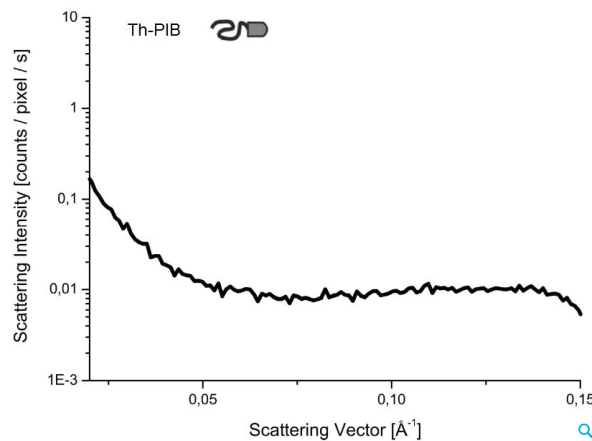


Figure 4.9: Scattering intensity vs. scattering vector q for sample Th-PIB in the bulk at room temperature.

Figure 4.9 shows the SAXS pattern of sample Th-PIB at room temperature. Different from the other three samples, SAXS pattern of Th-PIB doesn't show "a peak and a shoulder" structure but very weak scattering signal. By comparison of the chemical structure of thymine group and 2,6-diaminotriazine group shown in Figure 4.1, the thymine group has less conjugated rings and less polar. The demixing between the thymine group and PIB chain is weaker and no large aggregates formed.

Figure 4.10 shows the modulus master curve (black curves) of Th-PIB constructed with the shift factors from homopolymer PIB with a reference temperature of 20 °C. The modulus master curve of homopolymer PIB (blue curves) is also shown for comparison. The modulus curves of Th-PIB measured at different temperatures don't overlap after shifting, meaning that there are structural changes at different temperatures.

With increasing temperature (shown by the **arrow**), the modulus curves of Th-PIB come closer to homopolymer PIB. By combination of the SAXS analysis (no large aggregates)

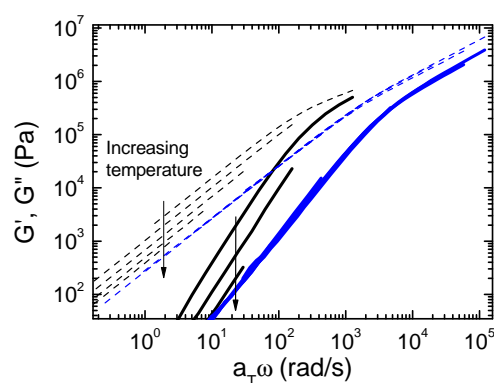


Figure 4.10: Master curve comparison between Th-PIB (G' : black curves; G'' : black dashed curves) and homopolymer PIB (G' : blue curves; G'' : blue dashed curves) with a reference temperature of 20 °C. The original modulus curves of Th-PIB were measured between 0 °C and 100 °C and the arrows indicate the direction of increasing temperature.

and rheological analysis, dimers of Th-PIB are expected to form at lower temperatures and disordered Th-PIB chains forms at higher temperatures. While at lower temperatures, the modulus master curves of Th-PIB is one order of magnitude higher than the homopolymer PIB, indication that pure dimers of Th-PIB are not enough to produce such a difference in the modulus curves. We suppose that there are also weak aggregates formed.

In conclusion, due to the weaker demixing tendency between PIB and thymine groups, dimers or weak aggregates were formed instead of large aggregates.

4.2.3 Micellar superstructure in a mixture of two complementary, monofunctional telechelic polymers Tr-PIB+Th-PIB

Now we switch to the monofunctional telechelic polymer mixture Tr-PIB+Th-PIB, which forms strong complementary hydrogen bonding in chloroform. The question then arises that how the strong hydrogen bonding influences the structural formation and rheological properties of the telechelic polymers in the bulk. Similarly, we start from the SAXS data analysis.

Analysis of the scattering data

Due to the strong complementary hydrogen bonding groups formed by Th/Tr, dimerization between two telechelic PIB chains would be dominant and it leads to the formation of a triblock copolymer where the PIBs are the end blocks and Tr/Th groups are the middle block.

Figure 4.11 shows the SAXS patterns (open symbols) of sample Tr-PIB+Th-PIB in the temperature range from 25 °C to 120 °C. The characteristic SAXS pattern of "a peak and a shoulder" shown in Tr-PIB at high temperature can be observed again for the sample Tr-PIB+Th-PIB. It seems that the complementary hydrogen bonding groups Tr/Th also show a

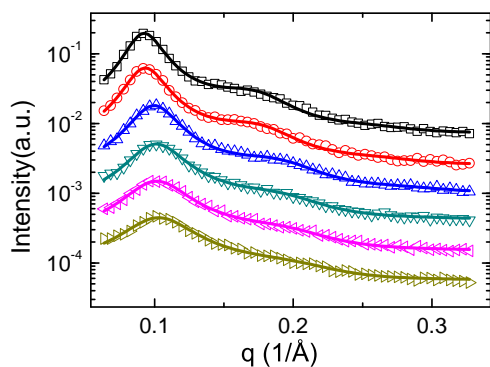


Figure 4.11: SAXS data (symbols) and model curves (solid lines) for sample Tr-PIB+Th-PIB at a series of temperatures (25°C(□), 40°C(○), 60°C(△), 80°C(▽), 100°C(◁), 120°C(▷)). All the curves were shifted along the vertical direction to have a better visibility.

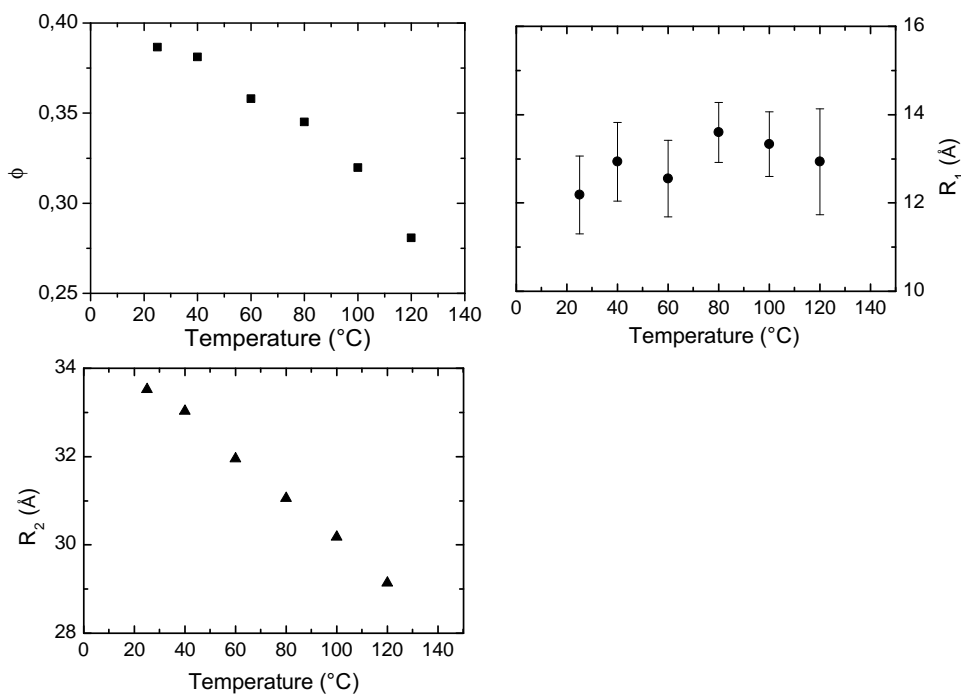


Figure 4.12: Temperature dependence of the volume fraction of micelles ϕ , the radius of the whole micelles R_2 and the radius of the micellar inner core R_1 for sample Tr-PIB+Th-PIB.

demixing tendency with the PIB main chain which causes the formation of spherical micellar aggregates. The demixing tendency between the PIB main chains and Tr/Th groups is not as strong as that between PIB main chain and Tr groups, thus even at the room temperature no ordered bcc structure can be observed.

The SAXS patterns of Tr-PIB+Th-PIB can be fitted with the same equation as for the SAXS patterns of Tr-PIB at high temperatures and the fitting curves are also shown in Figure

4.11 as solid lines. Again the fitting curves shows well agreement with the experimental data.

The resulting fit parameters including the volume fraction of micelles ϕ , the radius of micellar core R_1 , and the radius of micelles R_2 are plotted in Figure 4.12. All fit parameters behave similarly as the sample Tr-PIB. As we know that the factor that determines the phase behaviour in colloidal suspension is the volume fraction of micelles ϕ , disordered micelles state down to 25 °C for Tr-PIB+Th-PIB fits the volume fracion of only around 0.39 at around 25 °C, which is smaller than the critical volume fraction of 0.43 for order-disorder transition in Tr-PIB.

Analysis of the rheological data

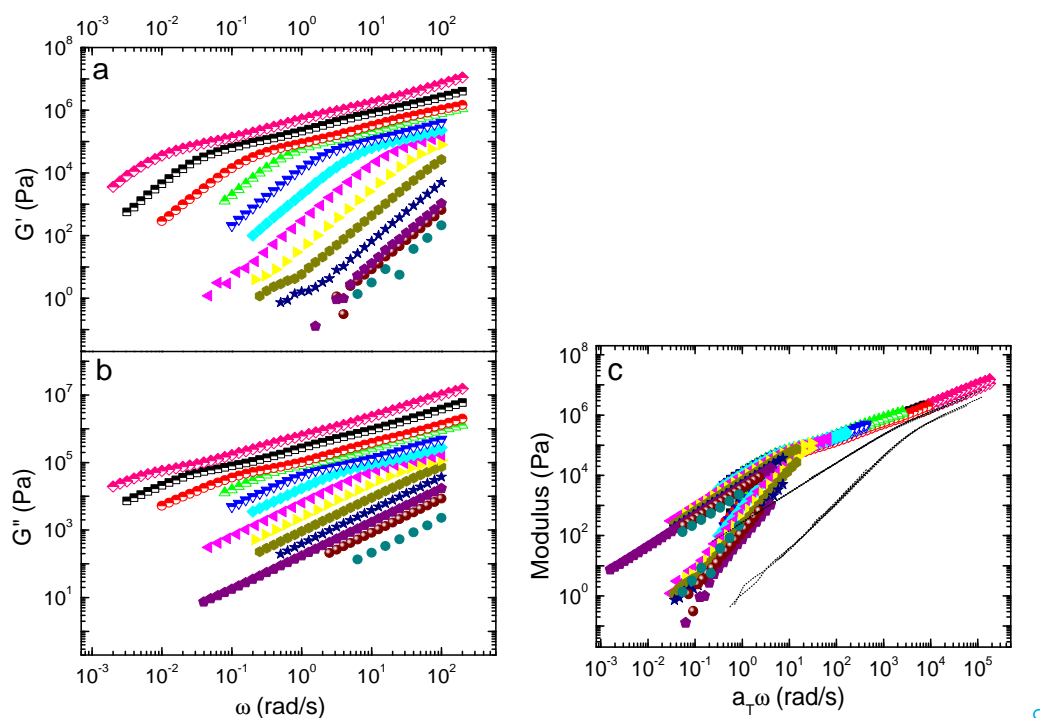


Figure 4.13: (a) Rheological measurements of Tr-PIB+Th-PIB at different temperatures. (a) Storage modulus G' and (b) Loss modulus G'' at different temperatures (same symbols as in Figure 4.7). (c) Master curve with a reference temperature of 25°C. The data for the homopolymer are included as dashed lines.

Now we switch to the rheological data of the sample Tr-PIB+Th-PIB to check the consistency with SAXS analysis. The storage and loss modulus curves of Tr-PIB+Th-PIB at a series of temperatures are shown individually in Figure 4.13a and 4.13b. Two regimes can be observed: the Rouse relaxation regime at high frequency (low temperature) and the terminal flow regime at low frequency (high temperature). In the Rouse relaxation regime, both the storage modulus and loss modulus show a slope of around 0.58 against angular frequency in a double-logarithmic scale. This is consistent with the unentangled spherical micellar structure as analysed from SAXS data. At lower frequency, the storage modulus and loss modulus

show slopes against angular frequency individually as 2 and 1 in a double-logarithmic scale. This is consistent with the terminal flow behaviour of the disordered micellar fluid structure.

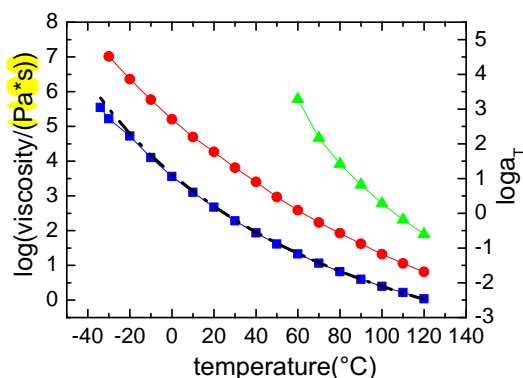


Figure 4.14: Temperature dependence of the viscosity of homopolymer PIB (■), the monofunctional mixture Tr-PIB+Th-PIB (●) and the bifunctional mixture Tr-PIB-Tr+Th-PIB-Th (▲). Additionally, the temperature dependence of horizontal shift factors from rheological measurements from literature [66] is shown (broken line).

The viscosity of sample Tr-PIB+Th-PIB and homopolymer PIB at a series of temperatures were measured with steady shear and are plotted in Figure 4.14. The shift factors of PIB from the literature are also plotted in Figure 4.14. It can be seen that the measured viscosity-temperature curve of our homopolymer PIB and the shift factor-temperature curve of PIB from the literature nearly overlap under the same scale, indication of the same chain dynamics of our PIB samples as in the literature. It can be observed that the viscosity of Tr-PIB+Th-PIB is one order of magnitude higher than the homopolymer PIB, which is consistent with the formation of spherical micellar aggregates.

Time-temperature superposition is valid for homopolymers to construct master curve since there is no structural changes in a broad temperature range. But for a self-assembling system whose structure might be sensitive to temperature, like our disordered micelles, time-temperature superposition is not valid any more for master curve construction. But if we keep shifting the original modulus curves of our disordered micelles with the shift factors of homopolymer PIB, then the nonoverlapping part in the "master curve" can be attributed to the structural changes due to temperature changes [67]. With this, we can try to separate the modulus contribution of chain dynamic and the structure assemblies. The deviation in the "master curve" constructed with shift factors of homopolymer can be attributed to the structural changes. Later on, we will use such a method to construct "master curve" for rheological analysis.

The "master curve" of Tr-PIB+Th-PIB constructed with shift factors from homopolymer PIB is shown in Figure 4.13c. Obviously, the Rouse relaxation regime at high frequency range overlaps very well while the terminal flow part does not. In the Rouse relaxation regime, mainly the chain dynamics are involved thus the overlapping of this part is possible after curve shifting. In the terminal flow part, not only the chain dynamics but also structural changes are involved. At high temperatures, the modulus curves at the same angular

frequency decrease due to decreasing volume fraction of micelles and smaller size of the micelles. Compared to the homopolymer PIB (shown in dashed lines), the terminal relaxation time of Tr-PIB+Th-PIB happens at a much smaller angular frequency, also indicating the formation of micellar aggregates.

From SAXS analysis we know that Tr-PIB+Th-PIB and Tr-PIB above 110°C in the bulk show disordered micellar structure which can also be treated as colloidal sphere suspension. We can take the spherical micelles as the colloidal spheres and the free telechelic polymer chains as the solvent. In the colloidal sphere suspension, the viscosity is dependent on the volume fraction of colloidal spheres and the viscosity of the solvent. To remove the influence of the viscosity of the solvent, normally the ratio between the viscosity of colloidal suspension and the viscosity of solvent is used. The relation between the viscosity ratio and the volume fraction of colloidal spheres were extensively studied and different empirical equations were obtained. We use an commonly used Krieger-Dougherty relation [54, 56] to fit our data

$$\frac{\eta}{\eta_0} = (1 - \phi/\phi_m)^{-[\eta]\phi_m} \quad (4.7)$$

where η is the viscosity of the colloidal suspension; η_0 is the viscosity of solvent; ϕ is the volume fraction of colloidal suspension; ϕ_m is the volume fraction of colloidal spheres at maximum packing at which the viscosity becomes infinite and $[\eta]$ is an intrinsic viscosity. $[\eta]$ is defined as $\lim_{\phi \rightarrow 0} (\eta - \eta_0)/(\eta_0\phi)$ where η is the viscosity with concentration of ϕ and η_0 is the viscosity without solute. In our case, the volume fraction of micelles is temperature dependent and can be obtained from SAXS fitting.

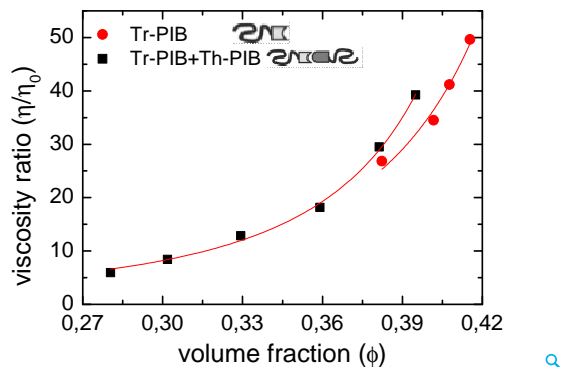


Figure 4.15: Ratio between the viscosity of the telechelic polymer melt and the homopolymer as a function of volume fraction of micelles for two different telechelic polymers: Tr-PIB and Tr-PIB+Th-PIB. Also shown is a fit with the empirical Equation 4.7.

The viscosity ratios for Tr-PIB and Tr-PIB+Th-PIB at different temperatures were plotted against volume fraction ϕ as shown in Figure 4.15. The viscosity-volume fraction curves were fitted with equation (4.7) as shown in solid lines in Figure 4.15. The fitting curves are in well agreement with the experimental data.

With the curve fitting, $[\eta]$ and ϕ_0 can be obtained. For Tr-PIB and Tr-PIB+Th-PIB, the fit parameters $[\eta]$ are 4.5 and 4.7 respectively; ϕ_0 are 0.52 and 0.48 respectively. By comparison, ϕ_0 for a system of colloidal spheres is still an open question and theoretical value range depending on the kinds of ordering (simple cubic, bcc, fcc) is between 0.524 to 0.74 [68]. For a bcc ordered geometry, the theoretical value for ϕ_0 is 0.68, larger than the fitting value in our systems. There are several reasons for such a deviation. Firstly, the extrapolation from our limited data range contains some uncertainty and a direct comparison between the fit value and the value from literature is difficult. Secondly, the spherical micelles in our system might have some unknown interactions which leads to the difference between our system to the repulsive colloidal sphere suspension. But the fitting value is still useful because the fit value is larger than the critical volume fraction of 0.43 at the order-disorder transition. In conclusion, also for this sample neither the Rouse-like chain dynamics nor the viscosity of the micellar fluid is directly related to specific hydrogen bonds. The SAXS data and rheological data were analysed (semi-)quantitatively and they correlate with each other.

4.2.4 Temperature dependent supramolecular networks of micellar aggregates

Above we have shown the analysis of monofunctional telechelic polymer Tr-PIB which shows ordered bcc micellar structure and the monofunctional telechelic polymer mixture Tr-PIB+Th-PIB which shows disordered micellar fluid, now we come to the studies of the bifunctional telechelic polymer mixture. The telechelic polymer is expected to form long telechelic polymer chains in dilute solution. Does the demixing tendency between hydrogen bonding groups and PIB chains also drive the spherical micellar aggregation? SAXS patterns can give the structural information of the telechelic polymer in the bulk. We start from the SAXS data analysis.

Analysis of the scattering data

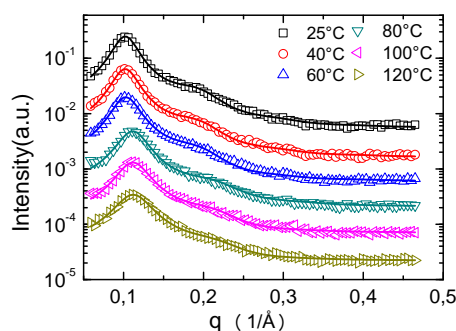


Figure 4.16: SAXS data (open symbols) of Tr-PIB-Tr+Th-PIB-Th at different temperatures (25 °C(□), 40 °C(○), 60 °C(△), 80 °C(▽), 100 °C(◄), 120 °C(►)) and fitting curves (solid lines). The data are shifted vertically.

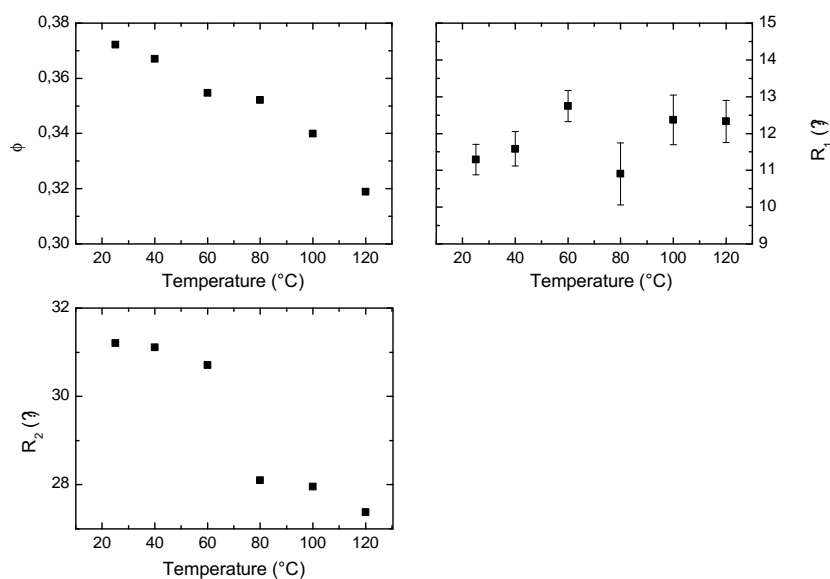


Figure 4.17: Volume fraction of micelles ϕ , radius of the whole micelles R_2 , radius of the micellar inner core R_1 in dependence on temperature for sample Tr-PIB-Tr+Th-PIB-Th.

Figure 4.16 shows the SAXS patterns (open symbols) of the sample Tr-PIB-Tr+Th-PIB-Th from 25 °C to 120 °C. Similar as the other two samples, the SAXS patterns again contain a peak and a shoulder. Accordingly, we conclude that the telechelic polymer chains again form micelles and we fit the SAXS curves with the Percus-Yevick model. The solid lines in Figure 4.16 represent the fitting curves for the SAXS data at different temperatures. One can see that the model fits the experimental curves well.

Figure 4.17 shows the fit parameters in dependence on temperature for sample Tr-PIB-Tr+Th-PIB-Th: the volume fraction of micelles ϕ , the radius of the whole micelle R_2 and the radius of micellar core R_1 . All parameters show the same trend as the other two samples. A volume fraction of 0.37 at 25 °C also explains the formation of disordered micelles structure instead of ordered micellar structure.

Analysis of the rheological data

Although the SAXS patterns of Tr-PIB-Tr+Th-PIB-Th look similar to the SAXS patterns of the other two samples, the rheological behaviour is very different because the bifunctional telechelic polymer mixture can form either long entangled dynamic chains or dynamic bonded spherical micelles.

Master curve construction for Tr-PIB-Tr+Th-PIB-Th was done with the shift factors from the homopolymer PIB, as shown in Figure 4.18. The reference temperature is 25°C. It is observed that the Rouse relaxation part overlaps well while the terminal flow part strongly changes with temperatures, different from the other two samples. A long storage modulus plateau is observed at low temperatures. Such a storage modulus plateau from the short unentangled telechelic polymers can be because of three reasons: entanglements due to the

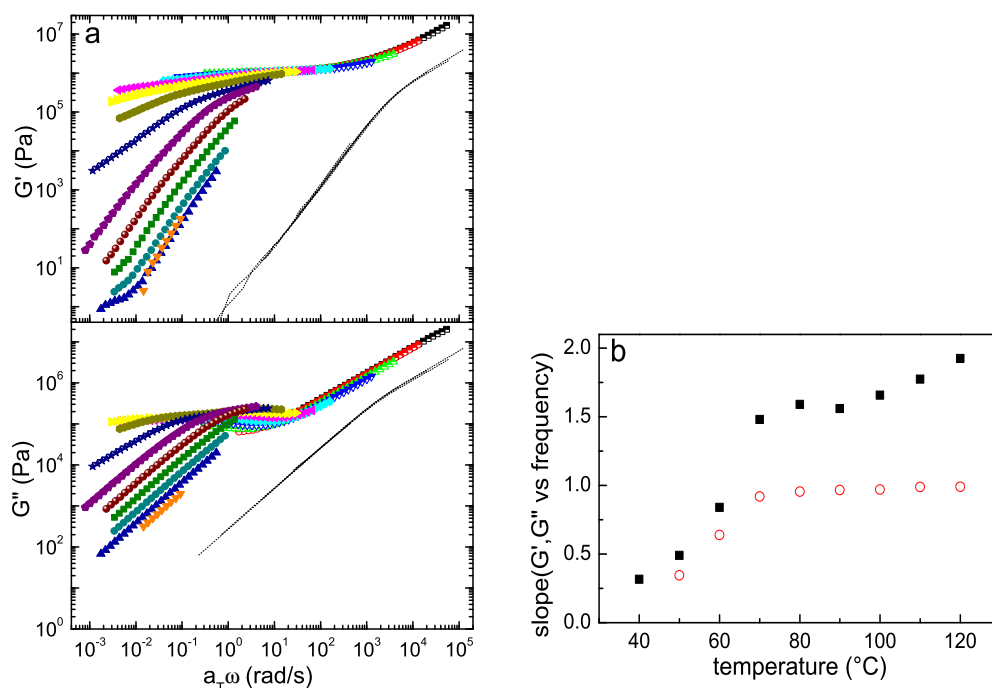


Figure 4.18: (a) Rheological master curve of Tr-PIB-Tr+Th-PIB-Th ($T_{ref} = 25^{\circ}\text{C}$). Different symbols represent the data measured at different temperatures (same symbols and colors as in Figure 4.7). The data for the homopolymer are included as dashed lines. (b) Slopes of $\log G'$ (filled square) and $\log G''$ (open circle) v.s. $\log \omega$ measured at low ω vs. temperature.

formation of long linear dynamic chains, elastic behaviour due to the formation of a ordered bcc lattice and network formation through dynamic hydrogen bonding. With the SAXS analysis we can conclude that the only possibility is the formation of interconnected dynamic network. At low angular frequency, the slopes of G' and G'' vs. angular frequency in double-logarithm scale at different temperatures are plotted in Figure 4.18b. The slopes increase gradually with increasing temperature and the slopes of G' and G'' are around 2 and 1 at high temperatures, meaning that the interconnected micellar network disassociates into isolated free micelles at higher temperatures. With decreasing temperature, both slopes decrease and they are close to each other at low temperatures, indication of a possible critical gel behaviour.

With the combination of SAXS and rheological data analysis, we know that Tr-PIB-Tr+Th-PIB-Th shows interconnected micelles at lower temperatures, as shown in Figure 4.19. The red objects are the end groups (clusters) and the green objects are the micellar corona composed of PIB chains. The grey objects are the free telechelic polymer chains. The micelles are interconnected via hydrogen bonding. Direct bridging chain connection is very unlikely, which can be seen from the similar SAXS peak positions as that of the other two monofunctional telechelic polymers.

The plateau modulus G_p of the interconnected micellar network at low temperatures is

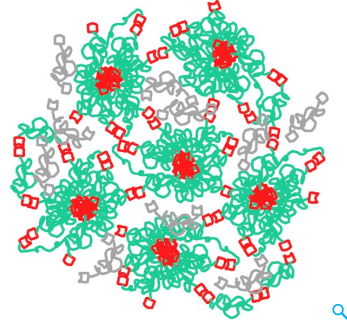


Figure 4.19: Scheme of crosslinked micelles of sample Tr-PIB-Tr+Th-PIB-Th. The light grey chains represent free matrix chains.

proportional to the mole density of network strands μ_s according to classical rubber theory [69].

$$G_p = \mu_s \cdot RT \quad (4.8)$$

Because the molecular weight of the PIB chains is smaller than critical molecular weight for entanglement M_c , entanglements don't contribute to the plateau modulus as in ref. [69]. By comparison of master curves between Tr-PIB-Tr+Th-PIB-Th and the homopolymer PIB, a horizontal shift at high frequency range can be observed which might be because of the higher glass transition temperature. The solid micellar core composed of hydrogen bonding groups can act as hard filler and enhance the modulus. Reference [70] gives a corresponding relation

$$G = G_p (1 + 2.5f_c + 14.1f_c^2) \quad (4.9)$$

where G is the storage modulus of the filled network, G_p is the modulus of the unfilled network, and ϕ_c the volume fraction of the filler. Take the sample at $T = 300$ K as an example, with the measured value of $G = 1$ MPa and $\phi_c = 0.15$ (ϕ_c estimated by the weight fraction of polar group), we get $\mu_s = 242$ mol/m³. We can compare it with the mole density μ of micelles which can be calculated from the radius of micelles from SAXS analysis.

Take the sample at 20°C as an example, substituting $R_2 = 3.12$ nm and $\phi = 0.37$ into the following equation, we can calculate the mole density μ of micelles

$$\mu = \frac{f}{N_A V_{micelle}} = \frac{f}{N_A \frac{4}{3} \pi R_2^3} = 5.21 \text{ mol/m}^3 \quad (4.10)$$

The ratio μ_s/μ gives the number of bridging chains per micelle $N_b \approx 46$. By comparison to the number of chains in one micelle, which is of the same order, we have a highly connected micellar network. The micellar network is linked through the hydrogen bonds which play a substantial role in this case. Only for this sample the rheological properties are primarily determined by the specific hydrogen bonds.

4.2.5 Unspecific hydrogen bonding by Infrared spectroscopy

As shown by SAXS and rheological data analysis, we know that three samples show micellar aggregates regardless of the association constant (measured in solution) of hydrogen bonding

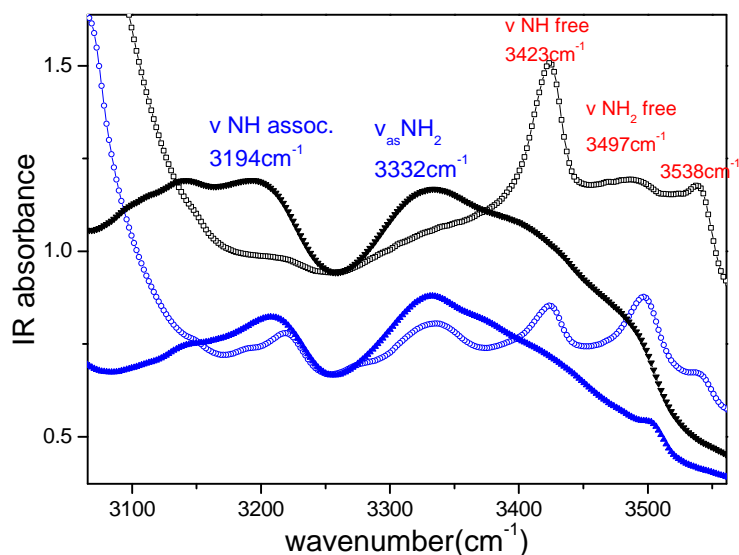


Figure 4.20: IR absorption spectroscopy for two samples in the bulk state and solution state: Tr-PIB in solution (unfilled black symbols), Tr-PIB in the bulk state (filled black symbols), Tr-PIB+Th-PIB in solution (unfilled blue symbols), Tr-PIB+Th-PIB in the bulk state (filled blue symbols). The black curves (Tr-PIB) were shifted upwards for better visibility.

end groups. In order to know whether the multiple hydrogen bonding is still dominant (or effective) in the telechelic polymer melt, we measured the infrared absorption spectroscopy of telechelic polymers (Tr-PIB and Tr-PIB+Th-PIB) in the bulk state. The infrared spectra of telechelic polymers in dilute solution are also measured and shown for comparison.

Figure 4.20 shows the IR absorption spectra for two samples in the bulk state and in dilute chloroform solution. Y-axis is the absorbance, given by $-\log T$. T is the ratio between the transmitted intensity and the received intensity. The absorbance can be quantitatively compared after the normalization with the thickness of the bulk samples and concentration of dilute solutions. It is known that triple hydrogen bonding forms in Tr-PIB+Th-PIB dilute solution. At high wavenumber range above 3000 cm^{-1} , the IR absorption normally corresponds to OH, NH groups. If the NH (OH) group forms hydrogen bonding with the partner, then the absorption wavenumber will appear at a lower wavenumber range [71], as shown in blue text in Figure 4.20. The IR absorption of free NH (OH) group lies normally in higher wavenumber range, as shown in the red text in Figure 4.20.

By comparison of IR spectrum between the solution and bulk state for two samples, we can see that samples in solution state shows a strong absorption at higher wavenumber range compared to the bulk state, meaning that in the dilute solution there is still a large amount of free NH groups. This is reasonable by analysing the triple hydrogen bonding as shown in Figure 4.21a.

In dilute solution, although nearly all the hydrogen bonding groups form triple hydrogen bonding, there are still free NH groups left as marked in blue curves in Figure 4.21a. These

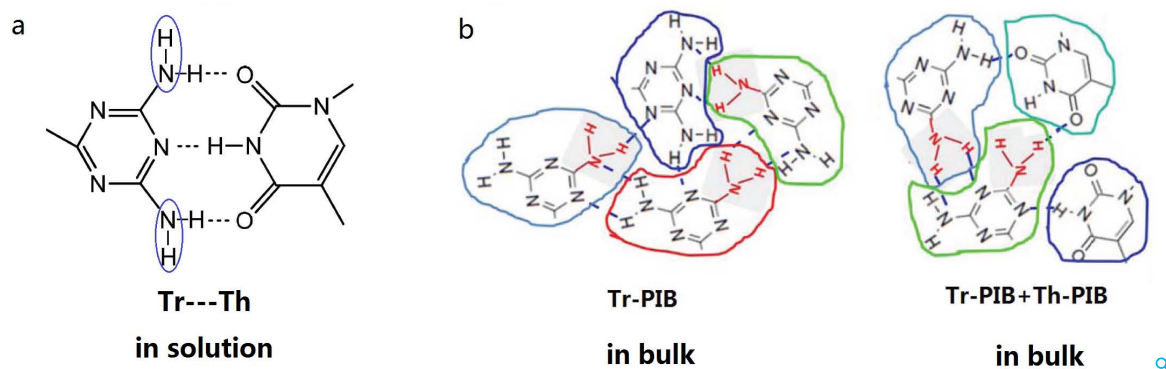


Figure 4.21: (a) a scheme of triple hydrogen bonding formed by triazine/thymine groups in dilute solution (b) hydrogen bonding networks formed in the bulk state of Tr-PIB and Tr-PIB+Th-PIB.

free NH groups might also form hydrogen bonding when the concentration of telechelic polymer is high, as shown in Figure 4.21b and 4.21c. This explains why the amount of free NH groups in the bulk state is so small compared to that in the solution.

By comparing the IR absorption spectra of Tr-PIB and Tr-PIB+Th-PIB in the bulk state, we can see that although Tr/Tr shows a very small association constant compared to the Tr/Th in dilute solution, the amount of hydrogen bonding formed in Tr-PIB in the bulk state is comparable to that of Tr-PIB+Th-PIB. This means that in the bulk state, the amount of hydrogen bonding formed in equilibrium state is not dependent on the association constant due to the large amount of unspecific hydrogen bonding.

4.3 Conclusion

Four different model polymer systems combining the ability to form specific telechelic bonds with a tendency for microphase separation were studied by quantitative structural and rheological analysis. In three cases unspecific interaction between hydrogen bonding groups and polar interactions led to the formation of micellar aggregates. For monofunctional systems the rheological properties are analogous to ordered colloidal solids at low temperatures and colloidal fluids at high temperatures. The system with bifunctional telechelic chains showed a rubbery plateau without ordering indicating the formation of a hydrogen bonded micellar network. Only in this case the hydrogen bonds play a direct role for the rheological properties. The results show exemplarily how important a detailed structural analysis is for a microscopic understanding and modeling of rheological properties of complex telechelic polymers, as the mechanical properties depend sensitively on chain association by dynamic linkages as well as on aggregation and self-assembly phenomena.

Chapter 5

Supramolecular PnBA-PIB block copolymer

In the last chapter (chapter 4), we have shown our studies on supramolecular PIB samples in melt state and found different kinds of micellar structures which were caused by the demixing tendency between PIB chains and hydrogen bonding groups and the unspecific hydrogen bonding. To reduce the demixing tendency between the polymers and the hydrogen bonding groups, more polar polymers PnBA modified with also thymine/triazine hydrogen bonding groups were synthesized by Florian Herbst [72] and studied with SAXS and rheology by Friedrich Lüders [73]. It was found that there are no large aggregates in the high-molecular-weight supramolecular Poly(n-butyl acrylate)(PnBA) polymers and there seems some aggregates in the low-molecular-weight PnBA polymers. In this chapter, two different polymers functionalized with complementary hydrogen bonding were mixed to construct a supramolecular block copolymer. The stronger hydrogen bonding groups Hamilton wedge/barbituric acid groups were used instead of thymine/triazine groups because macrophase separation can be observed with thymine/triazine hydrogen bonding groups meaning the thymine/triazine hydrogen bonding is not strong enough.

Although several groups have reported that supramolecular block copolymers can be formed through hydrogen bonding linkage of different blocks and ordered structure formation can be observed, similar as the covalent block copolymers [38, 39], there were only a few cases which reported the ordered structure formation of the supramolecular block copolymers and detailed studies are still needed, like the difference in structural formation and rheological properties between the covalently bonded block copolymers and supramolecular block copolymers. In our study, the temperature dependent SAXS and rheological measurements were done to study the structural information and rheological properties of supramolecular block copolymers. The structural and rheological properties of the supramolecular block copolymer were also compared with the reported results of normal covalently bonded block copolymers from the literature.

5.1 Sample

The supramolecular block copolymer was synthesized by Florian Herbst and the detailed synthesis and characterization can be found in the thesis [72]. Figure 5.1 shows the chemical structure of the supramolecular block copolymer PnBA-PIB. It contains two parts with 1:1 mole ratio of the Hamilton wedge functionalized PnBA (PnBA-HW) and the Barbituric acid functionalized PIB (PIB-BA). One block is PIB, which was also used in our studies in chapter 4. The other block is PnBA, which is more polar and liable to microphase separation with PIB blocks.

The molecular weight of PnBA-HW and PIB-BA are around 4000 g/mol and 3800 g/mol from NMR measurements, well below the critical entanglement molecular weight of PnBA ($M_c=20000$ g/mol [74]) and PIB ($M_c=13000$ g/mol [75]). The PDIs are both around 1.1 from GPC measurements. Hamilton wedge and Barbituric acids can form sextuple hydrogen bonds in solution and the corresponding association constant is around $3 \times 10^4 M^{-1}$ [38]. With the strong association between the Hamilton wedge and Barbituric acids [38], we expect that the supramolecular block copolymer PnBA-PIB forms.

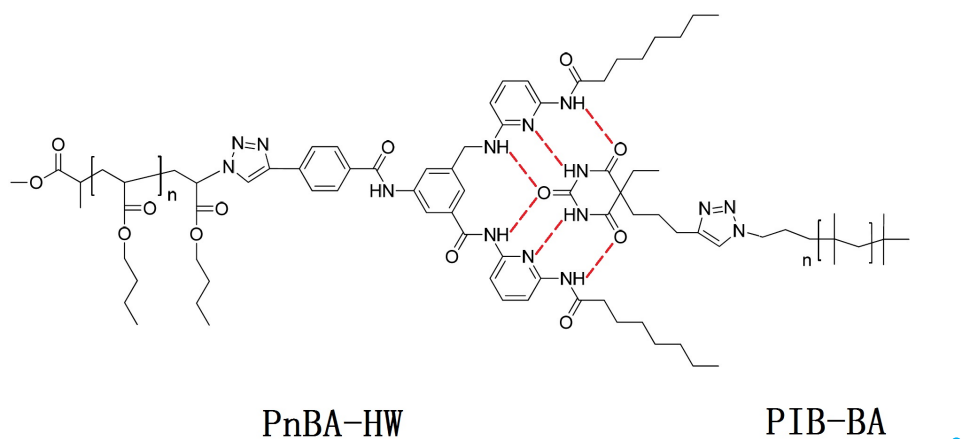


Figure 5.1: Chemical structure of Supramolecular block copolymer PnBA-PIB with the dynamic connection of hydrogen bonding group Hamilton wedge/Barbituric acids. The hydrogen bonding is represented by the red dashed lines.

5.2 Structural information from SAXS analysis

To know the structure of supramolecular PnBA-PIB at nano-scale, we start with SAXS data analysis.

SAXS measurements were done in the temperature range from -40 °C to 180 °C with an interval of 10 °C. The sample was annealed at 120 ° before the SAXS measurements. Figure 5.2 shows four selected SAXS patterns of supramolecular PnBA-PIB block copolymer at temperatures from -40 °C to 80 °C. Five peaks can be observed. The ratio of the peak positions q_1 , q_2 , q_3 , q_4 and q_5 is around 1:2:3:4:5, which is the characteristic of ordered

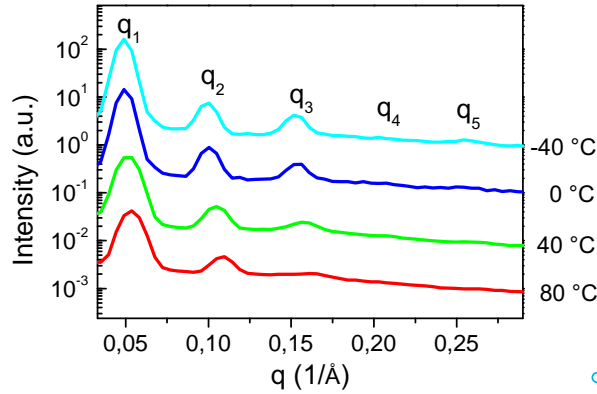


Figure 5.2: SAXS patterns of supramolecular block copolymer PnBA-PIB at a series of temperatures. The curves were shifted vertically for a better visibility.

lamellar structure. This indicates the formation of a stable supramolecular block copolymer PnBA-PIB.

To confirm the consistency between the size of supramolecular block copolymers and the long period of the ordered structure, we try to estimate these values and compare them. The size of supramolecular block copolymer PnBA-PIB includes three parts. We will calculate the size of two blocks based on Gaussian chain. The first part is PnBA block and the radius of gyration $\sqrt{\langle R_{g,1}^2 \rangle} = (M_w / (g/mol))^{1/2} \times 600 \times 10^{-4} / \sqrt{6}$ nm = 1.63 nm [76]. The second part is the PIB block and the radius of gyration $\sqrt{\langle R_{g,2}^2 \rangle} = \sqrt{Nb} / \sqrt{6} = 2.12$ nm (number of Kuhn segments $N = 14$, Kuhn length $b = 1.3$ nm) [61]. The third part is the hydrogen bonding groups HW/BA and the radius of the end groups is estimated to be around $l \approx 0.5$ nm. We estimate the radius of gyration of the supramolecular block copolymer approximately with the following equation $R = \sqrt{\langle R_{g,1}^2 \rangle + \langle R_{g,2}^2 \rangle} + l = 3.17$ nm.

Similar as the method that we used for calculation of the radius of gyration in chapter 4, the radius of gyration of the block copolymer R in disordered state can also be calculated based on Leibler theory [44] as $R = \sqrt{C}/q_0$, where C is a constant depending on the chain's composition and q_0 is the peak position in SAXS patterns from the disordered phase. Since the peak position doesn't change much during the order-disorder transition, we take q_0 to be approximate q_1 from the ordered state. Since the weight fraction of each block is 50%, and q_1 is 0.0536 ^{-1} at $80 \text{ }^\circ\text{C}$, the radius of gyration is calculated to be $R = \sqrt{8.42}/q_1 \approx 5.41$ nm. By comparison of the two values calculated based on Random coils and Leibler theory, we know that the result is reasonable that these two values are in the same length scale. The calculated value based on Random coils is a little smaller than the value calculated based on Leibler theory, which can be because the PIB and PnBA chains are in a little stretched state.

With this we can conclude that the ordered lamellar structure forms due to the formation of the supramolecular block copolymer and the microphase separation between PnBA and PIB blocks.

Figure 5.3 shows the schematic picture of the ordered lamellar structure. The blue lines and the red lines represent the PIB chains and the PnBA chains individually. The grey

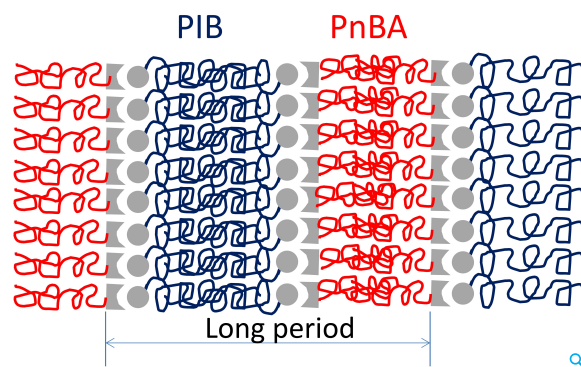


Figure 5.3: Schematic picture of ordered lamellar structure. The red lines represent the PnBA blocks and the blue lines represent the PIB blocks. The grey spheres and the wedges represent the hydrogen bonding groups Barbituric acids/Hamilton wedge.

symbols are the linkers of hydrogen bonding groups HW/BA.

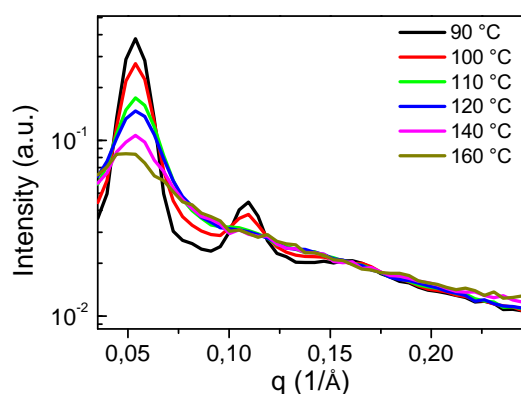


Figure 5.4: SAXS curves of supramolecular block copolymer PnBA-PIB at the temperatures around order-disorder transition temperature (T_{ODT}).

Figure 5.4 shows the SAXS patterns of supramolecular PnBA-PIB block copolymer at higher temperatures from 90 °C to 160 °C. Below 110 °C, the higher order peaks can be clearly observed. While at 110 °C, the higher order peaks disappear, indication of the formation of disordered state. The transition between 100 °C and 110 °C from ordered lamellar structure to disordered structure is the so-called order-disorder transition which happens universally in the covalent block copolymers [45]. After heating the sample to 180 °C and cooling back to 100 °C, the higher order peaks appear again, meaning the structure is reversible up to 180 °C and there is no macrophase separation up to this temperature.

The full width at half maximum (FWHM) of the first SAXS peak as a function of temperature is plotted in Figure 5.5a. Between 100 °C and 110 °C, there is a discontinuity which also indicates the order-disorder transition.

The inverse intensity of the first scattering peak $I(q_1)^{-1}$ and the corresponding position of the first scattering peak $2\pi/q_1$ are plotted against the inverse temperature, as shown in Figure

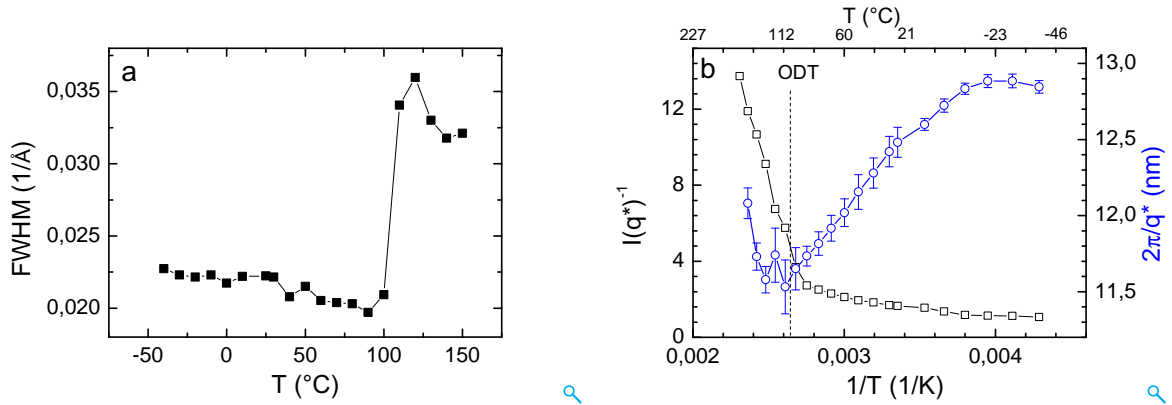


Figure 5.5: (a) FWHM of the first scattering peak v.s. temperature. (b) $I(q_1)^{-1}$ and $2\pi/q_1$ plotted against $1/T$.

5.5b. At higher temperatures, $I(q_1)^{-1}$ is inverse proportional to the inverse temperature $1/T$, which seems consistent with the mean field theory by Leibler [44]. The order-disorder transition temperature analyzed from FWHM is between 100 °C and 110 °C and lies also in the range of deviation.

Around T_{ODT} , the relation between $2\pi/q_1$ and $1/T$ shows a sharp change: below T_{ODT} , $2\pi/q_1$ is proportional to $1/T$ while above T_{ODT} , the trend become opposite. The result is inconsistent with the reported results [77, 78] of covalent block copolymers. For them, there is no discontinuity in the relation of $2\pi/q_1$ vs. $1/T$, only the slopes are slightly different below and above the order-disorder transition temperature. The difference between the supramolecular block copolymer and the covalently bonded block copolymer can be due to the weakening of hydrogen bonding above the order-disorder transition temperature. We hypothesize that an increasing fraction of supramolecular block copolymer disassociates into single components of PnBA-HW and PIB-BA which can act as the "solvent" surrounding PnBA blocks and PIB blocks respectively. The "solvent" swelling increases the mean distance between the supramolecular block copolymers.

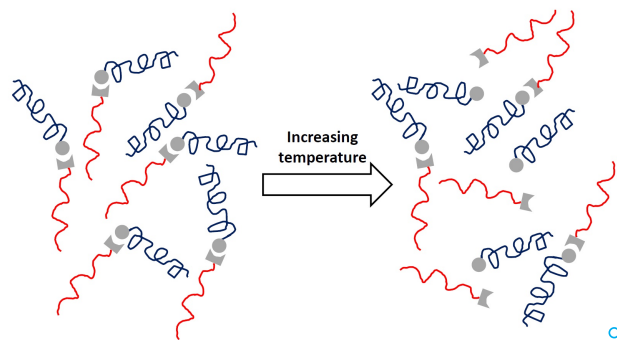


Figure 5.6: Schematic picture of disordered state during increasing temperature: an equilibrium state of a mixture of supramolecular block copolymer chains PnBA-PIB and the disassociated chains above (T_{ODT}).

As shown in Figure 5.6, we give a schematic picture to show how the disordered structure changes with increasing temperature.

The Landau theory predicts that χN at the order disorder transition temperature is around 10.5 for an symmetric block copolymer. For a polymer blend with volume fraction of 0.5, the critical value of χN is around 2 at the spinodal decomposition temperature. Even just above the order-disorder transition temperature, PIB and PnBA blocks are immiscible. Since there are still a large amount of supramolecular block copolymers PnBA-PIB, the macrophase separation between the disassociated PIB and PnBA chains is prevented.

5.3 Rheological data of supramolecular block copolymer PnBA-PIB

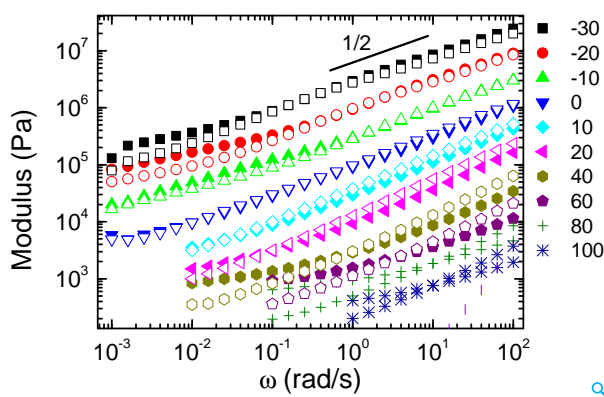


Figure 5.7: Dynamic shear storage (filled symbols) and loss (unfilled symbols) modulus curves for supramolecular block copolymer PnBA-PIB at a series of temperatures.

After the analysis of SAXS data, now we switch to the analysis of the rheological data of supramolecular PnBA-PIB block copolymer. Figure 5.7 shows the original shear modulus curves at the temperature range from 20 °C to 100 °C. We can see that G' is parallel to G'' at nearly all the temperatures over a certain frequency range and $G' \approx G'' \propto \omega^{0.5}$, which is consistent with the ordered lamellar structure formed by the symmetric block copolymers [78–80].

With both SAXS and rheological analysis, we can then confirm the ordered lamellar structure formation of supramolecular PnBA-PIB block copolymer at lower temperatures.

Master curve construction for shear modulus curves below T_{ODT} were done by manual horizontal shifting and the shift factors for storage modulus and loss modulus are the same. The master curve is shown in Figure 5.8a and the corresponding shift factors of supramolecular block copolymer PnBA-PIB together with shift factors of homopolymer PnBA and PIB depending on temperature $\log a_T \propto 1000/T$ are shown in Figure 5.8b. From the literature, in the ordered state, master curve construction is possible [45, 81] and the modulus curves measured at different temperatures overlap well after horizontal shifting. Compared to the

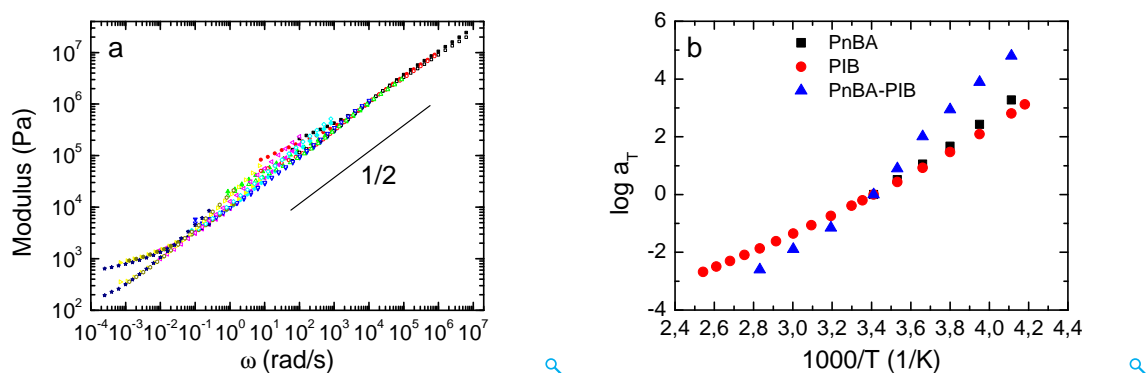


Figure 5.8: (a) Master curve construction of supramolecular block copolymer PnBA-PIB with the reference temperature of 20 °C. The symbols in different colors represent shear modulus measured at different temperatures. The storage modulus G' and loss modulus G'' are represented with filled and open symbols respectively. (b) Shift factors of homopolymer PnBA, homopolymer PIB and supramolecular block copolymer PnBA-PIB.

homopolymer PnBA and PIB, supramolecular block copolymer PnBA shows a larger slope in the plot of $\log a_T \propto 1000/T$. This indicates that the activation energy for supramolecular block copolymer PnBA-PIB increases due to the connection of two blocks through multiple hydrogen bonding.

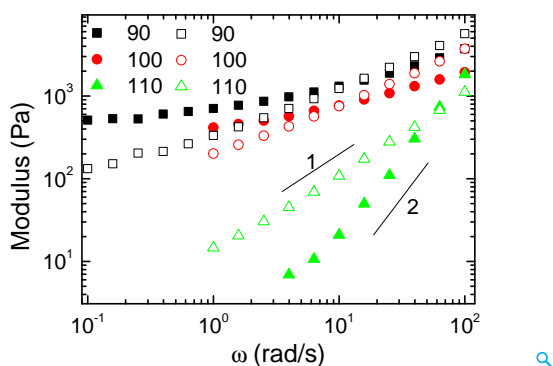


Figure 5.9: Shear storage (filled symbols) and loss modulus (unfilled symbols) data at temperatures around T_{ODT} .

Figure 5.9 shows the shear modulus curves of supramolecular polymer PnBA-PIB between 90 °C and 110 °C. We can clearly see that there is an abrupt change for the modulus curves from 100 °C to 110 °C. At 100 °C, there is a storage modulus plateau while at 110 °C the terminal flow behaviour can be observed from the slopes of G'' and G' against ω at the double logarithmic scale. The results indicate also the transition from ordered lamellar structure to disordered fluid structure as concluded from SAXS analysis.

We can conclude that the results obtained from SAXS and rheological analysis are consistent and both indicate the order-disorder transition at 110 °C.

5.4 Conclusion

With SAXS and rheological analysis, we can conclude the supramolecular block copolymer shows ordered lamellar structure at lower temperatures and it becomes disordered state via order-disorder transition. These behaviors are all similar to the covalently bonded block copolymers. While there are still one thing which the covalently bonded block copolymer does not show: in the disordered state, the supramolecular block copolymers gradually become disassociated and there is an equilibrium state of disassociated chains and supramolecular block copolymer chains even above 180 °.

Chapter 6

Nonlinear Rheology and Self-healing properties of Supramolecular PIB network

Dynamic gels (dynamic polymer networks) were studied extensively in the past decades [17, 82–87]. They can be formed either by different dynamic bonding (Hydrogen bonding [88, 89], metal-ligand coordination [11, 12], ionic interactions [15, 16]) or the solvent (midblock)-end block demixing [86, 90]. The dynamic gels were normally used as functional materials [23]. Many different gels were synthesized and the physical properties depending on the length of different blocks, the concentration, PH value, temperature, bonding strength were studied [86].

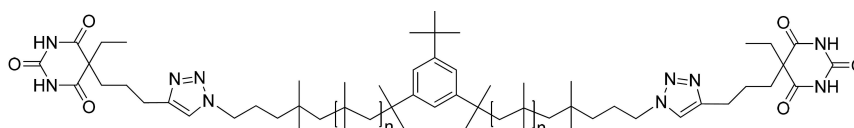
Recently dynamic gels were also used as self-healing materials [19, 91–94]. Skrzyszewska et al [95] synthesized a telechelic polypeptide functionalized with collagen-like triple helices and found the sample can self-heal after breakage by strong shear. Leibler [19] also synthesized a gel-like rubbery material by mixing fatty acids and urea and the sample can self-heal after being cutted into parts. Rowan [94] synthesized a metallosupramolecular polymer network and found the material is self-healable after exposure to ultraviolet light.

Although many dynamic polymer networks were synthesized and analyzed, most of them contain solvent [86, 90, 95] and the mechanical strength is low. To improve the mechanical properties of dynamic network and broaden the potential industrial application, dynamic network without solvent [96] can be an important choice. One aim of the chapter is to take a series of supramolecular polymer networks as model systems and study the structure-rheological properties with a combination of SAXS and rheology. Based on the structural information and linear rheological properties, nonlinear rheological behavior, as an important property in industrial application, was also studied, which is the second aim.

The third aim is to study the self-healing behaviour and probe the possible mechanism of self-healing in supramolecular polymer network. Usually the method to test the self-healing properties of the materials is to cut the sample into parts and then put them together for some time and then do tensile measurements [97, 98]. With such method, it is possible to measure whether one sample is self-healable or not. But it is hard to measure with such a method the self-healing kinetics and also to understand the self-healing mechanism. Here we take

the fractured sample after nonlinear startup shear as the initial state and then use the normal rheometer to test the self-healing kinetic in-situ by modulus measurements after breakage of the network.

6.1 Samples



| Samples | | M_n (NMR) [$\text{kg}\cdot\text{mol}^{-1}$] | M_n (GPC) [$\text{kg}\cdot\text{mol}^{-1}$] | PDI | Volume fraction of the end block |
|------------------------|------------|--|--|-----|-------------------------------------|
| telechelic polymers | PIB4K-BA2 | 3.9 | 4 | 1.3 | 0.13 |
| | PIB8K-BA2 | 8.7 | 7.9 | 1.2 | 0.065 |
| | PIB14K-BA2 | 14 | 13.8 | 1.2 | 0.038 |
| | PIB28K-BA2 | 28.4 | 26.7 | 1.1 | 0.019 |
| homopolymer | PIB30K | 30 | - | - | |

Table 6.1: Sample characteristics of four telechelic PIB samples and a homoPIB. Polydispersities ($\text{PDI} = M_w/M_n$) were obtained by GPC. Volume fraction of the end block was calculated with the assumption of the same density for the end block and PIB. Additional information was given in the reference [99]

We investigated a series of barbituric-acid terminated Polyisobutylenes (PIB) with different molecular weights: 4 kg/mol, 8 kg/mol, 14 kg/mol and 28 kg/mol. The molecular weights of the telechelic PIBs vary from below entanglement molecular weight ($M_e = 6.9$ kg/mol) to above critical entanglement molecular weight ($M_c = 13.1$ kg/mol) [60]. A homoPIB with a molecular weight of 30 kg/mol was also investigated for comparison. Table 6.1 gives the table of sample information. The polar groups including barbituric acid and 1,2,3-triazole were taken as the end groups to calculate the volume fraction of end block with the assumption that the densities of the end block and PIB are the same, as shown in Table 6.1. The detailed synthesis information of the telechelic PIB samples was described in the former paper [99].

6.2 Results and Discussion

6.2.1 Evidence for Interconnected micellar network from SAXS and rheological analysis

SAXS data analysis

Since small angle X-ray scattering (SAXS) can give structural information of the telechelic PIB sample at nanoscale, we start from the SAXS data analysis. Figure 6.1a shows the SAXS

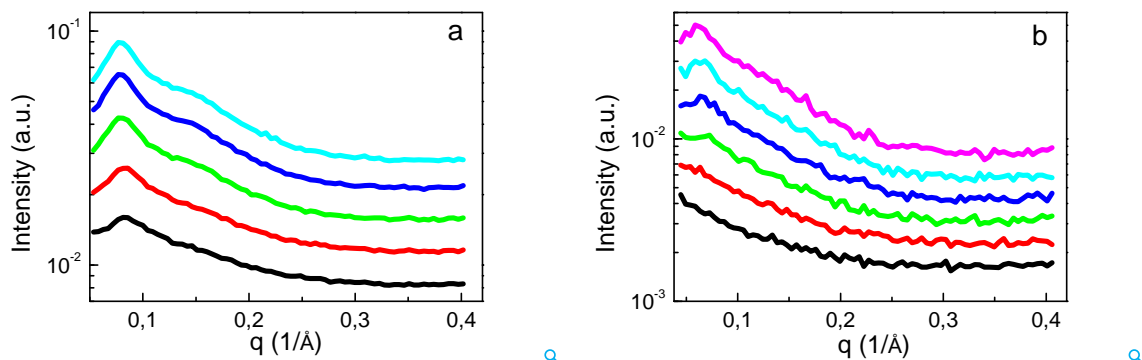


Figure 6.1: (a) SAXS curves of PIB14K-BA2 at a series of temperatures (120 °C —; 80 °C —; 40 °C —; 0 °C —; -40 °C —). The curves are shifted vertically to overlap the curves at high q . (b) SAXS curves of PIB28K-BA2 at a series of temperatures (120 °C —; 100 °C —; 80 °C —; 60 °C —; 40 °C —; 20 °C —). The curves are shifted vertically for better visibility.

patterns of sample "PIB14K-BA2" at different temperatures.

A peak at a q value of around 0.08 \AA^{-1} and a shoulder at q value of around 0.15 \AA^{-1} are observed in the SAXS pattern. With increasing temperature, intensity of both the peak and shoulder decreases.

The SAXS patterns of sample PIB4K-BA2 and PIB8K-BA2 are very similar to that of PIB14K-BA2 and the data are shown in the appendix. However, the sample with highest molecular weight PIB28K-BA2 shows different SAXS patterns. As shown in Figure 6.1b, at 20 °C and 40 °C, there are a weak peak at $q \approx 0.075 \text{ \AA}^{-1}$ and a very weak shoulder at $q \approx 0.13 \text{ \AA}^{-1}$. With increasing temperature, the intensity of both the peak and shoulder gradually decrease and they disappear at around 100 °C. After cooling from 120 °C, the SAXS patterns for all samples are reversible.

We take the telechelic polymers as asymmetric triblock copolymers. The peak and shoulder in the SAXS patterns of sample PIB14K-BA2 also suggest that the telechelic polymers are neither in disordered state where normally only a correlation hole could be observed in SAXS patterns, nor in the ordered state where normally higher order peaks can be observed in SAXS patterns. In chapter 4, we know that the SAXS patterns including a peak and a shoulder were also observed in the triazine/thymine functional PIB samples and there the structure was analyzed to be the disordered micelles structure.

For sample PIB14K-BA2, similar structure was supposed to form. The nonpolar PIB chains and the polar barbituric acid groups are expected to demix and the low-volume-fraction barbituric acid groups tend to assemble and form spherical aggregates. The longer PIB chains act as the micellar corona. One special thing for the bifunctional PIB sample PIB14K-BA2 is that the micelles can be connected by the telechelic PIB chains which makes it difficult to distinguish the near micelles and judge the boundary between the micelles.

Figure 6.2 shows a schematic picture of the micellar structure formed by telechelic PIB. The spherical micellar core is composed of barbituric acid groups and the corona is com-

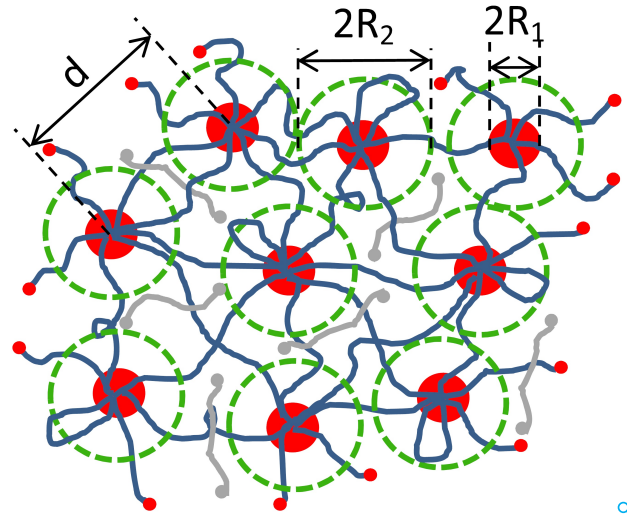


Figure 6.2: Schematic picture of micelles formed by telechelic PIB. The red spheres are the spherical core formed by barbituric acid groups and the blue lines are the PIB chains. The green dashed circles give the repulsive interaction boundary of "hard sphere". d is the distance between near micellar cores; $2R_1$ and $2R_2$ are the diameters of the spherical core and the "hard sphere". The grey lines outside of the green spheres are the free telechelic PIB chains.

posed of PIB chains. The radius of micellar core and the distance between the micelles are represented by R_1 and d respectively. The green dashed lines around the red spherical cores were drawn to describe the effective radius of the spherical micelles and it will be useful for the later discussion of the SAXS curve fitting model. In consideration of the high concentration of telechelic polymers (no solvent), the barbituric acid groups of one chain are more likely located in two different micellar cores because in the telechelic polymer melt the distance between the micellar cores is comparable to the end-to-end distance of the telechelic polymer chains, which will be shown in the following discussion. This leads to the effect that there are a large amount of bridging chains in the system which are used to connect the spherical micelles. Such hypothesis can be supported by the reported experimental and simulation results [100,101] on spherical-phase forming triblock copolymer that the fraction of bridging chains is around 50% to 80%. There are also disassociated free chains in the system and with increasing temperature the amount of the free chains also increase which can be conclude from the weakening peak and shoulder in the SAXS curve at high temperatures. Besides the bridging chains and free chains, there can also be dangling chains and loop chains, which are also shown in Figure 6.2. Due to the presence of the bridging chains, there are not only repulsive interaction but also attractive interaction between the micelles.

We take the peak position from SAXS pattern as q^* and then $2\pi/q^*$ corresponds to the average distance between the micellar cores and thus also to the end-to-end distance of the bridging telechelic polymers. We plot $2\pi/q^*$ and the end-to-end distance of a Gaussian chain R v.s. M_w for four samples at 20 °C in Figure 6.3. R is calculated with the equation $R = \sqrt{N}b$ (the molecular weight of Kuhn segments $M_{Kuhn} = 273g/mol$; the number of Kuhn segment $N = M_w/M_{Kuhn}$; the Kuhn length $b = 1.3$ nm.) [61].

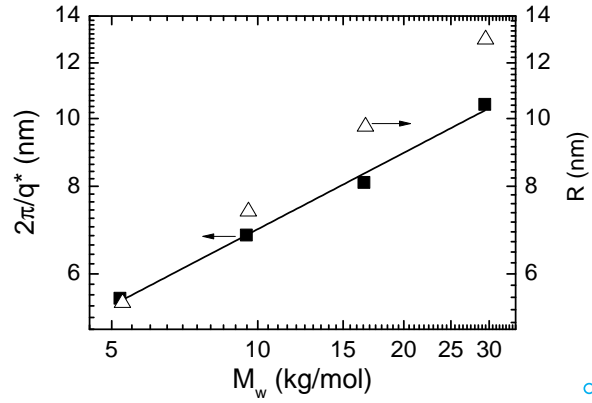


Figure 6.3: Distance between micellar cores ($2\pi/q^*$) (■) and the end-to-end distance R calculated based on Gaussian chain (Δ) in dependence on the mass average mole mass M_w for four samples.

By a linear fit for $\log(2\pi/q^*) \sim \log M_w$, a slope of 1/3 is obtained. The growth exponent of 1/3 between the end-to-end distance and the molecular weight suggests that the bridging telechelic polymer chains are not Gaussian chains (random coil) but more dense packing chains with less interpenetration. This may well fit the spherical micellar structure from the SAXS analysis and will be a reason that the dense spherical micelles can be taken as hard spheres and the SAXS patterns can be modeled with hard sphere model.

The SAXS pattern, as we discussed before, suggests that the sample forms disordered micellar structure. To further analyze the SAXS data, we imagine the telechelic polymer system as spheres (spherical micelles in our case) surrounded by solvent (free chains in our case) and then use Perkus-Yevick hard sphere model [47, 48] to fit the SAXS curve. The scattering intensity is given by the following equation:

$$I(q) = KS(qR_2) \int_{R_1=0}^{\infty} \Phi(qR_1) f_p(R_1, \bar{R}_1, \sigma) dR_1 + C \quad (6.1)$$

It includes mainly two parts: the structure factor of interacting repulsive hard spheres (interacting spherical micelles in our case) $S(q, R_2, f)$ based on Perkus-Yevick model and the form factor of the spherical micellar cores $\Phi(qR_1)$. q is the scattering vector; R_2 is the effective hard sphere radius of the spherical micelles; R_1 is the radius of micellar core; ϕ is the volume fraction of micelles. Both K (prefactor) and C (the scattering background) are constants.

Similar as the thymine/triazine functional PIB system in chapter 4, we assume the size of the micellar core show a log-normal distribution and the probability density distribution $f_p(R_1, \bar{R}_1, \sigma)$ can be represented by the following equation

$$f_p(R_1, \bar{R}_1, \sigma) = \frac{1}{R_1 \sigma \sqrt{2\pi}} e^{-\frac{(\ln R_1 - \ln \bar{R}_1)^2}{2\sigma^2}} \quad (6.2)$$

The integration range for R_1 in 6.1 was chosen from 1 Å to 80 Å. The parameter σ is in the

range of 0.06 to 0.15, i.e. the width of the radius distribution is quite narrow.

Note: Although we use Perkus-Yevick hard sphere model to fit the imagined "hard sphere" system, there is no distinct boundary between the "hard spheres" and the surrounding matrix. Since the micelle is not really "hard sphere" and the interaction between the micelles is not purely repulsive and it also includes the attractive interaction as we discussed before, ϕ and R_2 from the curve fitting are only approximate and effective values. But we think the repulsive interaction is dominant and the SAXS curve fitting with Perkus-Yevick hard sphere model is effective. The detailed fitting equation can be found in our previous work [59].

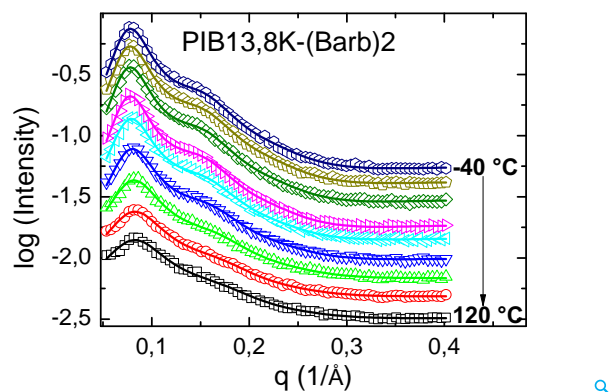


Figure 6.4: SAXS curve fit with Perkus-Yevick model for PIB14K-BA2 at a series of temperatures with an interval of 20 °C. Open symbols represent the original data and the solid lines represent the fit curves. The data are shifted vertically for different temperatures for better visibility.

The SAXS patterns for PIB14K-BA2 at different temperatures and the corresponding fit curves are shown in Figure 6.4. Obviously, the selected hard sphere model fits the data well.

The fit results for four samples in dependence on temperatures are shown in Figure 6.5. The error bars of R_1 are based on the error from the curve fit. ϕ and R_2 have very small errors and thus the error bars are not shown. We can see that the volume fraction and the radius of the hard sphere decrease with increasing temperature. The radius of micellar core shows more noise and the trend is not clear. With increasing temperature the demixing between the nonpolar PIB block and the polar barbituric acid block weakens, which makes the corresponding micelles become smaller and the volume fraction of the micelles also become smaller and leads to higher volume fraction of free chains and dangling chains.

For such telechelic polymers, which can be taken as highly asymmetric triblock copolymers, higher molecular weight of PIB blocks leads to the lower volume fraction of the end blocks. According to the phase diagram of the block copolymers [44, 46], with decreasing volume fraction of the minor block $(\chi N)_{ODT}$ at the order-disorder transition (ODT) strongly increases. Lower volume fraction of the end block goes into the direction of the disordered state (less volume fraction of micelles) when χN is constant. Higher molecular weight of the telechelic polymer leads to a higher N which facilitates the ordered state (larger fraction of micelles), but at the same time a lower volume fraction of the minor blocks which facilitates the disordered state (less volume fraction of micelles). From the SAXS curve fit, the volume

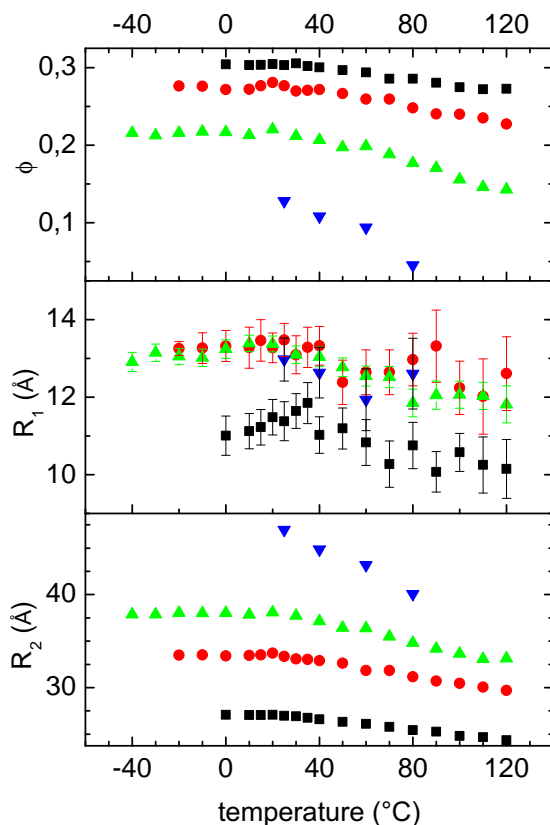


Figure 6.5: Fit results (volume fraction of hard spheres ϕ , radius of inner core R_1 , radius of hard sphere R_2) for four samples (PIB4K-BA2 ■; PIB8K-BA2 ●; PIB14K-BA2 ▲; PIB28K-BA2 ▼.) at different temperatures.

fraction of micelles decreases with increasing molecular weight of the telechelic polymers, meaning that the negative effect that that decreasing volume fraction of the end block shows on the volume fraction of micelles is even stronger than the positive effect that the increasing molecular weight of telechelic polymers shows on the volume fraction of micelles.

In the telechelic polymer melt, with increasing molecular weight of the telechelic polymers, the size of telechelic polymers, which act as the micellar corona, also increases. In consideration of the dense packing micelles, the radius of micelles is expected to increase with the molecular weight of telechelic polymers. The result that increasing molecular weight of block copolymers leads to increasing radius of spherical micelles was also observed for the block copolymer melt [102].

The radius of micellar core from curve fit shows noise and no clear trend with increasing molecular weight of the telechelic polymers and temperatures. The radius of the micellar core is nearly independent on the molecular weight for the three high molecular weight samples while the sample PIB4K-BA2 has a smaller radius of the micellar core. The reason is not clear till now.

Beforehand, we take our system as colloidal suspension and the fitting parameters are

obtained based on SAXS curve fitting with the Perkus-Yevick model. To come back to the real interconnected micellar network and understand quantitatively the aggregation state of the micellar network, we try to estimate the aggregation number. The aggregation number (g) is defined as the number of end groups in each micellar core.

The aggregation number can be estimated based on the volume of the micellar core by dividing the volume of the micellar core by the mole volume of the end group.

$$g = \frac{\frac{4}{3}\pi R_1^3 \rho N_A}{M_{end}} \quad (6.3)$$

where ρ is the density of end groups (we assume $\rho \approx 1 \text{ g/cm}^3$); N_A is Avogadro's number; R_1 is the radius of the micellar core from the SAXS curve fitting; $M_{end}=264 \text{ g/mol}$ is the molecular weight of the Barbituric acid group. For sample PIB14K-BA2 at $20 \text{ }^\circ\text{C}$, R_1 from the fit is 13.3 \AA , and the calculated aggregation number is around 22.

The calculated aggregation number for different samples at different temperatures is shown in Figure 6.6.

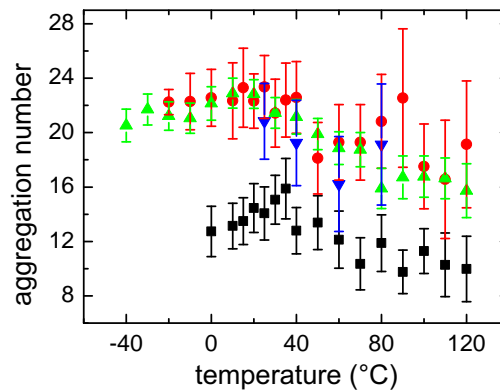


Figure 6.6: Aggregation number v.s. temperature for four samples (PIB4K-BA2 ■; PIB8K-BA2 ●; PIB14K-BA2 ▲; PIB28K-BA2 ▼.)

Since the calculation of the aggregation number is based on the radius of micellar core, the trend of the aggregation number looks very similar to the that of the radius of micellar core. There is large noise in the data of aggregation number and trend of the aggregation number is not clear with temperature and molecular weight of telechelic polymers. With increasing molecular weight of telechelic polymers, the size of micelles increases, while the volume fraction of micelles shows a different trend. The sample PIB4K-BA2 has a smaller radius of the micellar core compared to that of the other three high molecular weight samples. The reason is not clear till now.

Now we estimate the total number of chains available per volume. We start from the spherical micelles and assume the spherical micelles pack in some ordered structure so that we can do the calculation based on the unit cell. Since we found body centered cubic (bcc) ordered structure in our former hydrogen bonded telechelic PIB samples [59] and the peak position is only slightly shifted around the order-disorder transition temperature, we also assume the bcc packing in our case. The bcc unit cell is shown in Figure 6.7. The blue spheres

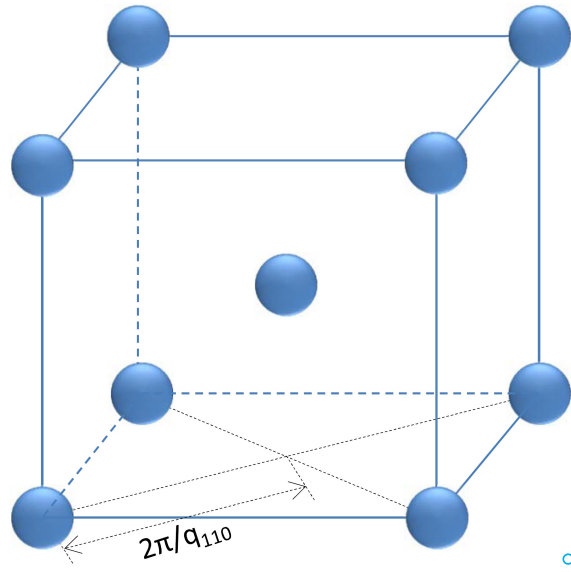


Figure 6.7: Unit cell of the body centered cubic (BCC) crystal lattice.

represent the spherical micelles but the size of the spheres in the figure is reduced to increase the visibility. Each unit cell is composed of two spherical micelles and the surrounding matrix. We name a single spherical micelle and its surrounding a micelle unit. For this volume we want to calculate the number of chains within.

We take q^* as the first peak (q_{110}) shown in SAXS pattern from bcc ordered phase. The lattice parameter l is equal to $2\sqrt{2}\pi/q^*$. Then we can calculate the number of chains per micellar unit (g') based on the lattice parameter and compare it with the aggregation number calculated before. Since one telechelic polymer chain contains two end groups, the number of end groups per micelle unit (g') can be calculated by dividing the volume of one micelle unit (half volume of the unit cell) by the half volume of telechelic polymer chain (corresponding to one end group), as shown in the following equation.

$$g' = \frac{(2\sqrt{2}\pi/q^*)^3/2}{M/(2\rho N_A)} \quad (6.4)$$

where ρ is the density of polyisobutylene [103] (0.92 g/cm^3); N_A is Avogadro's number; q^* is the peak position in the SAXS pattern; M is the molecular weight of telechelic polymer. If we take PIB14K-BA2 at 20°C as an example, $q^* = 0.078 \text{ \AA}^{-1}$, the calculated g' is around 60.

In consideration of the various states of the telechelic polymer chains (bridging chains, loop chains, dangling chains and free chains) as we mentioned before and by comparison of g and g' , we know that not all of the end groups in the micellar unit are aggregated in the micellar core as for the bridging chains and there are also a fraction of free chains in the micellar unit, which is consistent with the disordered micellar fluid structure from SAXS analysis. The fraction of aggregated end groups in each micellar unit is around $22/60 = 0.36$, meaning 36% of the end groups of telechelic polymer chains aggregate in the micellar cores for this sample.

With SAXS analysis, we can conclude that the telechelic PIB samples form disordered spherical micelles. With SAXS curve fitting with Perkus-Yevick model, the size and the volume fraction of micelles and the aggregation number can be estimated.

Linear rheology analysis

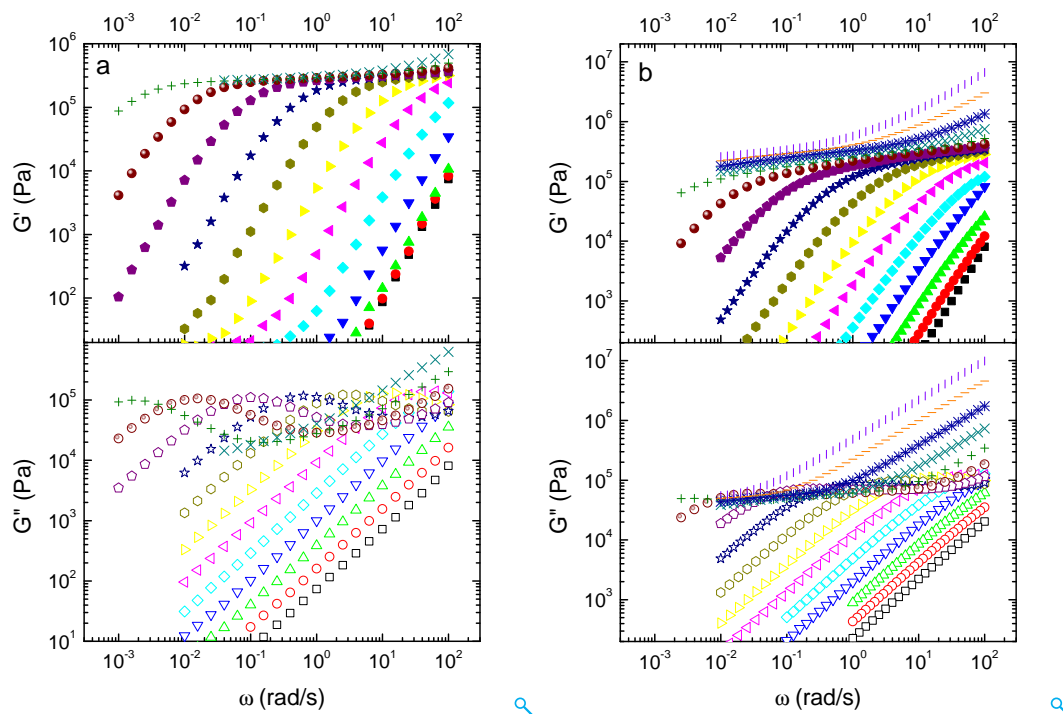


Figure 6.8: Complex modulus (G' , G'') v.s. angular frequency ω for (a) sample PIB14K-BA2 and (b) sample PIB28K-BA2 at different temperatures ($-30\text{ }^{\circ}\text{C}$ |, $-20\text{ }^{\circ}\text{C}$ —, $-10\text{ }^{\circ}\text{C}$ *, $0\text{ }^{\circ}\text{C}$ x, $10\text{ }^{\circ}\text{C}$ +, $20\text{ }^{\circ}\text{C}$ o, $30\text{ }^{\circ}\text{C}$ pentagon, $40\text{ }^{\circ}\text{C}$ star, $50\text{ }^{\circ}\text{C}$ diamond, $60\text{ }^{\circ}\text{C}$ square, $70\text{ }^{\circ}\text{C}$ triangle, $80\text{ }^{\circ}\text{C}$ diamond, $90\text{ }^{\circ}\text{C}$ inverted triangle, $100\text{ }^{\circ}\text{C}$ triangle, $110\text{ }^{\circ}\text{C}$ circle, $120\text{ }^{\circ}\text{C}$ square).

Figure 6.8 shows dynamic rheological data for sample PIB14K-BA2 and PIB28K-BA2 from $120\text{ }^{\circ}\text{C}$ to $-30\text{ }^{\circ}\text{C}$. The experimental results of sample PIB4K-BA2 and PIB8K-BA2 are very similar to that of PIB14K-BA2 and are shown in the Appendix. From the modulus curves of PIB14K-BA2, we can see terminal flow at lower frequency or higher temperature and a plateau modulus at higher frequency or lower temperature. In consideration of the low molecular weight of PIB (just above M_c) and the long rubbery plateau, the only possibility to show a plateau modulus is to form a dynamic network through physical crosslink of end groups, which is consistent with hypothesized bridging chains interconnected micellar network structure from the SAXS analysis. At even higher frequency, the Rouse relaxation process is also involved.

The modulus curves of sample PIB28K-BA2 seem a little different: in the "rubbery" plateau part, there is no obvious minimum in G'' , meaning there is some extra relaxation process involved. This is probably because the fraction of free end groups (lower volume

fraction of micelles from SAXS) is higher and the molecular weight of PIB is higher than critical entanglement molecular weight (M_c) and they introduce reptation relaxation process from micellar corona. Further discussion will be addressed later.

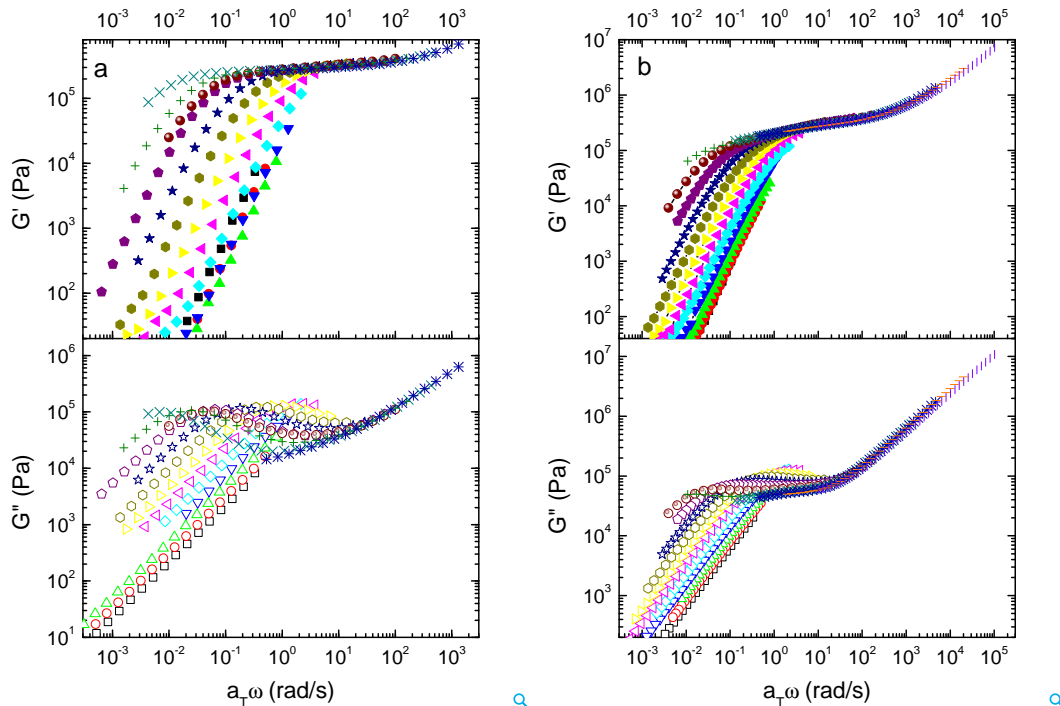


Figure 6.9: Master curves of (a) sample PIB14K-BA2 and (b) sample PIB28K-BA2 with a reference temperature of 25 °C.

The master curves of sample PIB14K-BA2 and PIB28K-BA2 were constructed with shift factors from homoPIB and are shown in Figure 6.9. The Rouse relaxation part overlaps while the flow part not. They correspond to two different relaxation modes. The Rouse relaxation is related to the chain dynamics of PIB and the terminal flow is controlled by dynamic bonding.

One special thing is the master curve of the highest molecular weight sample PIB28K-BA2. By zooming in to the plateau modulus part and plotting G'' in the same figure as shown in Figure 6.10, one can see that between α relaxation to terminal relaxation there is an additional maximum in G'' which means an extra relaxation process. The master curve of homoPIB ($M=30$ kg/mol) is also shown in Figure 6.10 for comparison with the telechelic PIB sample. We can see that the extra small shoulder in loss modulus master curves of telechelic PIB and the terminal relaxation peak of the homopolymer seems in the similar range.

It was reported in the literature [104, 105] that a peak of G'' in the loss modulus curve of the entangled star polymer besides the longest relaxation time (crossover between G' and G'') exists, which corresponds to the reptation relaxation time of the arm chains. So we can attribute the extra relaxation process to the reptation relaxation process of the dangling polymer chains, i.e. the corona of the micellar aggregates.

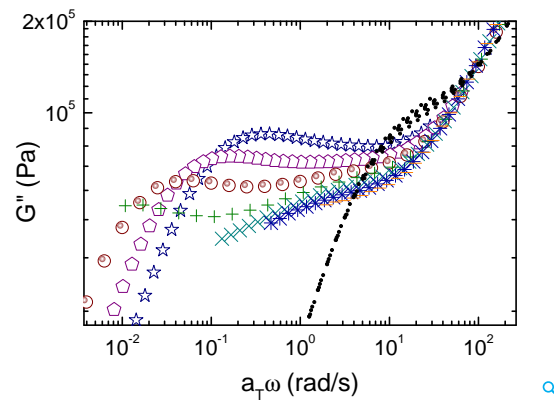


Figure 6.10: Master curve comparison of loss modulus between PIB28K-BA2 (G'' : colored symbols) and homopolymer PIB30K (black symbols). The reference temperature is 25 °C.

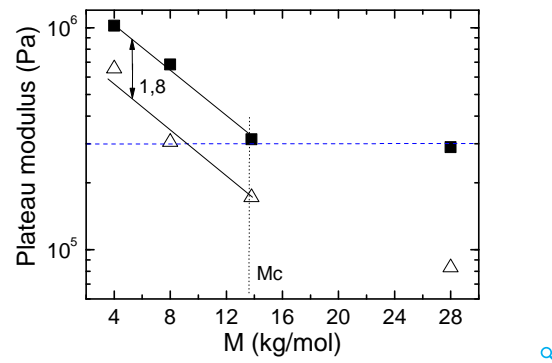


Figure 6.11: Experimental plateau modulus (■) and calculated plateau modulus (△) v.s. molecular weight at room temperature.

The storage plateau modulus was taken at the frequency where the loss modulus shows a minimum. The plateau modulus for four samples with different molecular weight is shown in Figure 6.11. With increasing molecular weight, the experimental plateau modulus first decreases. Above the critical molecular weight of entanglements M_c for a corresponding homopolymer, the plateau modulus becomes nearly constant at around the value of 0.3 MPa (dashed line) which is the plateau modulus of well-entangled homoPIB melt.

To estimate the plateau modulus, the rubber theory is used with the assumption that all the telechelic polymer chains are used as active polymer strands (bridging chains) and the estimated plateau modulus is shown in Figure 6.11. The equation for calculation of the estimated plateau modulus is shown in the following

$$G_{p,calculated} = \frac{\rho RT}{M} \quad (6.5)$$

Where ρ is the density of telechelic polymer (we take the density [106] of PIB ≈ 0.92 g/cm³), R is the Boltzmann constant, T is absolute temperature and M is the molecular weight between two crosslink points, i.e. the molecular weight of the polymers.

By comparison of the experimental plateau modulus and the calculated plateau modulus, we can see that the calculated plateau modulus predicts the trend of the experimental plateau modulus while the experimental values are significantly higher than the calculated values (approximate 1.8 times higher) for all samples although we already took all the telechelic polymer chains as bridging chains. Similar results were also reported [59, 107]. At higher molecular weight, the reason is that entanglements are not considered for modulus calculation. At low molecular weight part, the reason can be that there exists constraint topological entanglements in the short-chain melt because of the fixed chain ends.

To analyze the terminal flow part, the relaxation spectrum, described in chapter 2, was calculated with the software of Anton Paar rheometer. Two different relaxation spectrums ($H(\tau)$ vs. τ ; $H(\tau)\tau$ vs. τ) of sample PIB14K-BA2 at a series of temperatures are shown in Figure 6.12. The peak widths for both spectra are around 1 decade, meaning the dynamic bonding relaxation has a broad distribution.

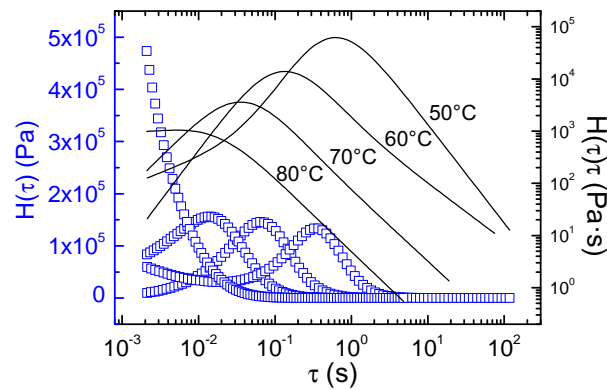


Figure 6.12: Relaxation spectrums ($H(\tau)$ vs. τ : solid lines; $H(\tau)\tau$ vs. τ : unfilled squares) obtained with the software from Anton Paar rheometer.

We take the peak of the relaxation time distribution from the relaxation spectrum ($H(\tau)\tau$ vs. τ) and compare this relaxation time with the relaxation time from the inverse of the crossover frequency of G' and G'' and the relaxation time calculated by η/G (η and G from dynamic rheological measurements) according to the single-mode Maxwell model.

The results are shown in Figure 6.13. We can see they are similar and comparable. By taking account of the limitation of calculation of relaxation spectrum, we will take the reciprocal of crossover (G' and G'') frequency $1/\omega$ as the terminal relaxation time for further use.

In Figure 6.14a, we plot the natural logarithm of the relaxation time from the inverse of the crossover frequency at different temperatures for four telechelic polymers with different molecular weights. We can see that for the four telechelic polymers, the relaxation times are very similar and not strongly molecular weight dependent, which is consistent with the prediction by Tanaka [108] that the modulus-frequency master curve depends only weakly on the molecular weight of the polymer chains. For comparison, the natural logarithm of terminal relaxation time of homopolymer PIB with molecular weight of 30 kg/mol is also plotted vs. $1000/T$. Obviously, the temperature dependence of the relaxation time of the

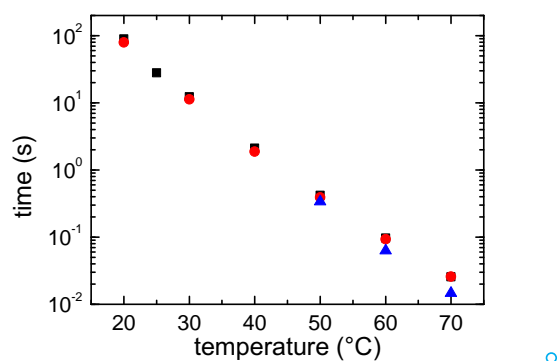


Figure 6.13: Comparison of relaxation time from crossover frequency(■), Maxwell model (●) and the relaxation time from relaxation spectrum (▲) depending on temperature for sample PIB14K-BA2.

homopolymer is considerably smaller than that of the telechelic polymers. This is again an indication that in the case of the telechelic polymers the terminal flow dynamics is controlled by hydrogen bonding instead of chain dynamics.

We can further fit the data with linear function and get the flow activation energy which is shown in Figure 6.14b. The flow activation energy of the homopolymer is much smaller compared to the telechelic polymers, suggesting the different flow mechanisms. For the four telechelic polymers, the flow activation energy decreases with increasing molecular weight. This could be explained by the reason that the fraction of aggregated chains decreases and thus a smaller volume fraction of micelles are involved in the dynamic network with increasing molecular weight. The terminal relaxation process is likely to be related to the cooperative process of the hydrogen bonding. The analysis above further indicates that the terminal flow dynamics of the supramolecular polymer network is controlled by hydrogen bonding instead of chain dynamics.

6.2.2 Nonlinear rheological analysis

In the former section, we did SAXS and linear rheological analysis and found that the telechelic polymers form dynamic interconnected micellar network. For commercial application, study of nonlinear rheological properties of the materials is very important. The nonlinear rheological measurements are useful for the further study of self-healing analysis of the dynamic networks. The nonlinear rheological measurements were performed with startup shear experiments. In startup shear, the samples were sheared with constant shear rate for some time, during which the shear stress and shear strain were recorded.

At a shear rate which is smaller than the reciprocal of terminal relaxation time, the dynamic network has enough time to reconstruct and shows flow behavior. Shear stress first increases with shear strain and becomes constant at high shear strain, indication of terminal flow behavior. The Weissenberg number is defined as $Wi = \dot{\gamma}\tau$.

At a shear rate which is larger than the reciprocal of terminal relaxation time, the dynamic network has no time to reconstruct. With increasing shear strain, shear stress first increases

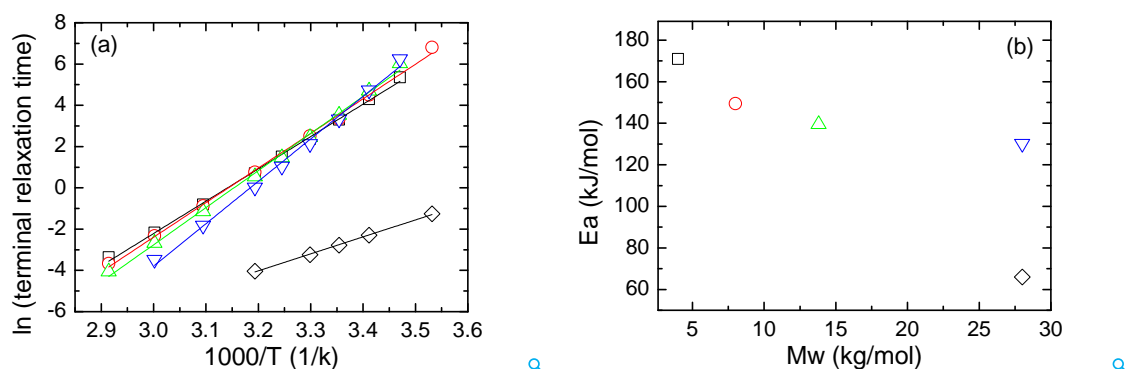


Figure 6.14: (a) Logarithm of terminal relaxation time vs. $1000/T$ for four telechelic samples (PIB4K-BA2: \square ; PIB8K-BA2: \circ ; PIB14K-BA2: \triangle ; PIB28K-BA2: ∇) and a homopolymer PIB with molecular weight of 30 kg/mol (\diamond) and the corresponding linear fitting curves; (b) Flow activation energy vs. molecular weight for four telechelic samples and the homopolymer (the same symbols as shown in (a)).

due to the extension of the network strands. Gradually, shear stress on the network strands and hydrogen bonding clusters is large enough that the dynamic bonding cluster will break at non-equilibrium state at high strain and it leads to the fracture of the dynamic network, which can be manifested as shear yielding.

Startup shear measurements of sample PIB14K-BA2 at 25 °C and 10 °C and sample PIB14K-BA2 at 20 °C and 15 °C with a series of shear rates are shown in Figure 6.15a, b, c and d. The terminal relaxation time from the linear response measurements of sample PIB14K-BA2 at 25 °C is 33 s at 25 °C. At lower shear rate ($Wi=0.33$), we see the shear stress gradually increases and becomes constant at some strain, indication of the viscoelastic fluid. At higher shear rate ($Wi > 1$) [109, 110], the shear stress first increases and then decreases, causing a stress maximum, which is called shear yielding.

The yield stress and strain both increase with the applied shear rate. This is contradictory with the theoretical results from Tanaka [111] which predicts that the yield strain is weakly dependent on the shear rate in the associative dynamic network. In the reported work on nonlinear rheological results of associative polymer network, yield strain can either increase [95, 112] and decrease [113] with increasing shear rate or be independent [114] on shear rate. But the mechanism is still unclear.

Figure 6.15b shows the startup shear measurements of sample PIB14K-BA2 at 10 °C. The results look similar to that at 25 °C. One difference is that at higher Weissenberg number, strain hardening at higher strain before yielding point can be observed. This can be due to the nonlinear stress response of the bridging PIB chains at higher strain. At higher shear rate, the stress grows very fast, during which hydrogen bonding disassociation is relatively slow, so the stress is mainly applied on the bridging chains and the stress-strain relation becomes nonlinear at higher strain [1], which leads to the strain hardening behavior at high strain.

Figure 6.15c and 6.15d show the startup shear measurements of sample PIB4K-BA2 at 20 °C and 15 °C. The stress-strain curves look similar to that of sample PIB14K-BA2 at 25 °C and there is no strain hardening. The difference is that the yielding strain is smaller than

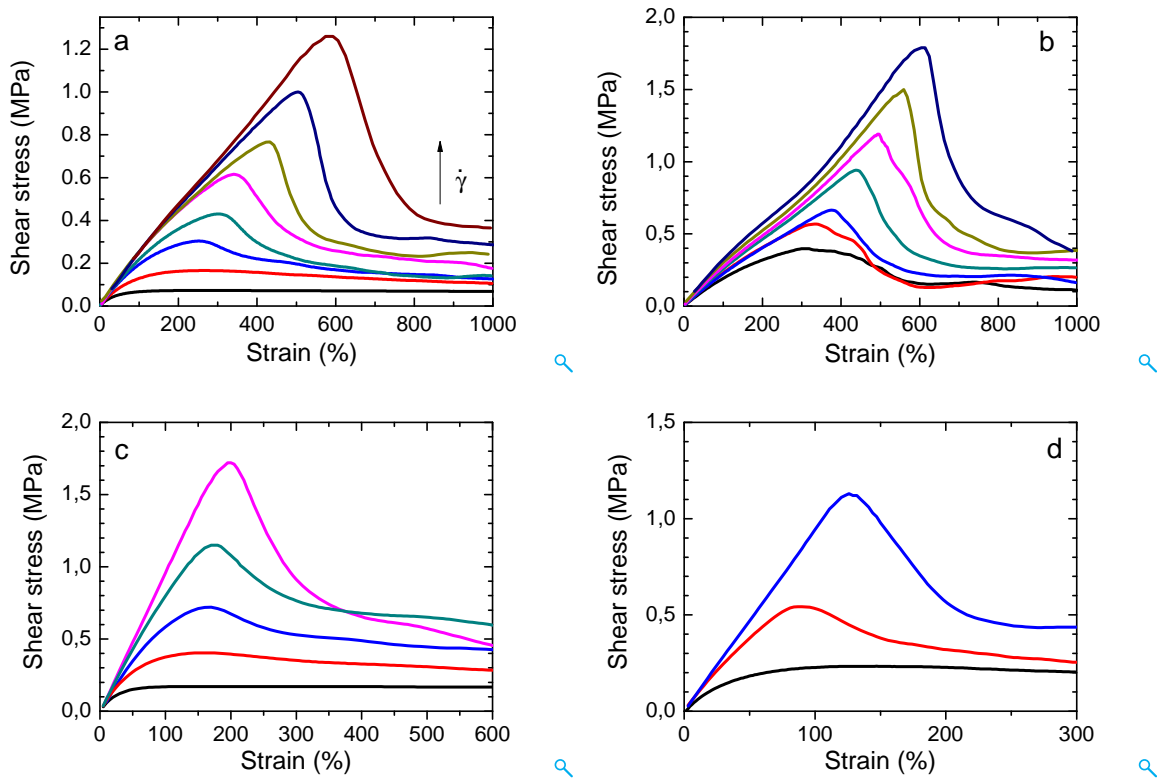


Figure 6.15: (a) Stress-strain curves for PIB14K-BA2 at 25 °C for different shear rates ($Wi=0.33$ —, $Wi=1.04$ —, $Wi=3.3$ —, $Wi=10.4$ —, $Wi=33$ —, $Wi=100$ —, $Wi=330$ —, $Wi=1000$ —). (b) Stress-strain curves for PIB14K-BA2 at 10 °C for different shear rates ($Wi=9$ —, $Wi=28$ —, $Wi=90$ —, $Wi=280$ —, $Wi=900$ —, $Wi=2800$ —, $Wi=9000$ —). (c) Stress-strain curve for PIB4K-BA2 at 20 °C for different shear rates ($Wi=1.1$ —, $Wi=3.5$ —, $Wi=11$ —, $Wi=35$ —, $Wi=110$ —). (d) Stress-strain curve for PIB4K-BA2 at 15 °C for different shear rates ($Wi=0.5$ —, $Wi=5$ —, $Wi=50$ —).

that of sample PIB14K-BA2 at the same Weissenberg number. This is related to the chain length of the bridging chains. Here we try to estimate the maximum length of the bridging chains and compare it with the yielding strain. In the stretched state, the PIB chains can be in the zig-zag conformation and the maximum length can be calculated as $R_{max}=nl\cos(\theta/2)$, where n and l are the number and the length of the skeleton C-C bonds; θ is the angle between neighboring C-C bonds ($\approx 68^\circ$). With calculation, R_{max} of sample PIB14K-BA2 and PIB4K-BA2 are 63.1 nm and 18 nm respectively. We take the distance between micelles as the length of the bridging chains. From the distance between the micelles obtained in SAXS measurements in Figure 6.3, the maximum extension ratios can be calculated as $\lambda_{max} = \frac{R_{max}}{2\pi/q^*} - 1$. The maximum extension ratios of samples PIB14K-BA2 and PIB4K-BA2 are 687% and 227%. From Figure 6.15, all the yielding strains are reasonably smaller than the maximum extension ratios although it's hard to compare these two parameters in different geometries quantitatively.

The startup shear data of sample PIB8K-BA2 also show similar shear yielding behavior and are shown in Appendix. The startup shear results of sample PIB28K-BA2 are more complicated and the yielding points are not very obvious, which might be due to the involving of chains entanglement because the molecular weight is higher than M_c . The startup shear data of PIB28K-BA2 will not be discussed further and are also shown in Appendix.

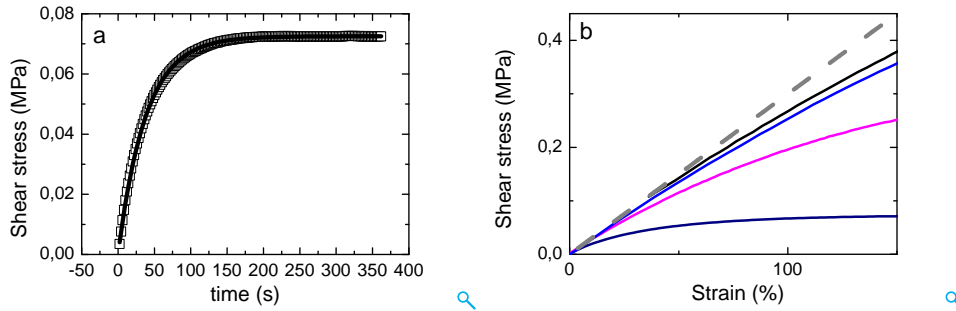


Figure 6.16: (a) Shear stress-time data (\square) and fitting curve ($—$) for startup shear measurement with $Wi=0.33$ at 25 °C. (b) Shear stress-strain curves (solid lines) of startup shear measurements for a series of shear rates at small strains ($Wi=0.33$ —, $Wi=3.3$ —, $Wi=33$ —, $Wi=330$ —) of sample PIB14K-BA2 at 25 °C. The linear curve with a slope of the plateau modulus from linear dynamic measurements ($G=3 \times 10^5$ Pa) is shown in dashed line.

For the startup shear measurements with strain rate smaller than the inverse terminal relaxation time, the sample shows flow behavior. We then use Maxwell model to fit the stress-time curve of PIB14K-BA2 with $Wi=0.33$ at 25 °C

$$\sigma = \eta \dot{\gamma} \left(1 - \exp\left(-\frac{G}{\eta} t\right) \right) \quad (6.6)$$

where σ is shear stress; η is viscosity; $\dot{\gamma}$ is shear rate; G is the plateau modulus; t is time.

The fitting curve is shown in Figure 6.16a. The Maxwell model fits the experimental data well. The fit parameters $G=1.9 \times 10^5$ Pa and $\eta=7.25 \times 10^6$ Pa \times s are comparable to the measured value $G=3 \times 10^5$ Pa and $\eta=9 \times 10^6$ Pa \times s from linear rheological measurements.

With Maxwell fluid model, there is no yielding point with startup shear. For the startup shear curves with higher Weissenberg number, we compare the beginning part of the startup shear curve with a purely elastic model. As shown in 6.16b, startup shear curves of sample PIB14K-BA2 at a series of Weissenberg numbers at 25 °C are shown together with the linear curve with a slope of the plateau modulus of PIB14K-BA2 from linear dynamic measurements. We can see that at small strain and high shear rates, the startup shear curve overlaps with the linear curve. Although at higher strain, it is not possible to fit the stress-strain curve, the initial part can be fitted with elastic model.

The dependence of yield strain on Weissenberg number for two samples at different temperatures is plotted in Figure 6.17. We can see that with increasing Wi , the yield strain increases. The yield strain also increases with increasing molecular weight of the telechelic PIB samples.

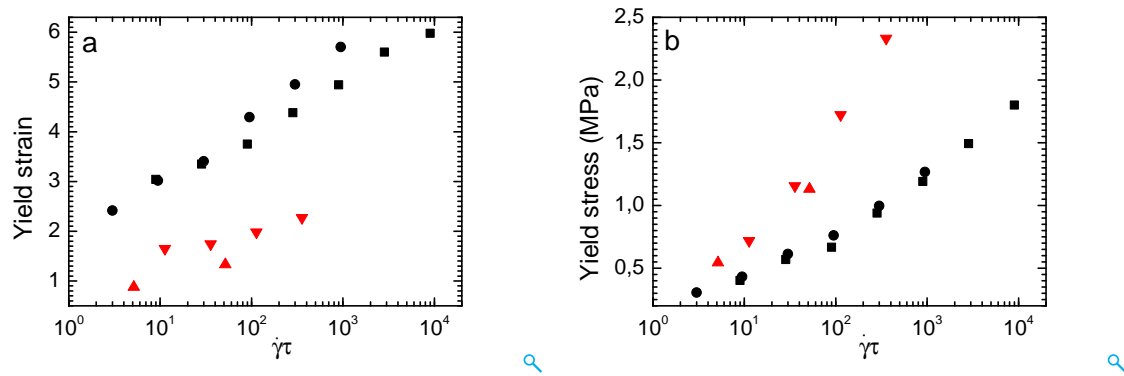


Figure 6.17: (a) Yield strain-shear rate data for two samples at different temperatures (PIB14K-BA2: 10 °C (■) and 25 °C (●); PIB4K-BA2: 15 °C (▲) and 20 °C (▼)). (b) Yield stress-shear rate data for the same samples at different temperatures (the same symbols as in (a)).

The dependence of yield stress on Weissenberg number for two samples at different temperatures is also plotted in the right plot in Figure 6.17b. We can see that the data measured at different temperatures for each sample nearly overlap. But the yield stress increases with decreasing molecular weight at the same Weissenberg number. In summary, the yielding stress-shear rate curves measured at different temperatures can be superposed after including the relaxation time τ into the shear rate. We can conclude that the yield stress shows a logarithm dependence on the Weissenberg number.

To quantitatively understand the shear yielding, we use a model from the literature to deal with the relation between the yielding stress and shear rate [95].

The model deals with the shear yielding during startup shear of dynamic network. The dynamic bonding has certain life time and it decreases as a function of shear stress. Assuming shear stress grows linearly with strain and at the yield point the life time of the bonds corresponds to the duration of the experiments, and the stress is found to be proportional to the logarithm of shear rate ($\sigma_c \delta / G_p \xi \propto \ln(\delta \dot{\gamma} \tau / \xi)$), consistent with the experimental results of our system. σ_c is the yield stress; δ is the length that characterizes the width of the bond potential, i.e. the size of the micellar cores from SAXS curve fitting; G_p is the plateau modulus of the dynamic network obtained from the linear dynamic rheological measurements; ξ is the typical distance between junctions in the network, i.e. the distance between the micelles d from SAXS patterns; τ is terminal relaxation time from linear dynamic rheological measurements; the slope of the linear curve fitting is a constant K , which is a factor to describe the local stress intensification at the crack tip and the fitting value of K is 3.82 in our case.

The corresponding new plot $\sigma_c \delta / G_p \xi - \ln(\delta \dot{\gamma} \tau / \xi)$ is shown in Figure 6.18. The corresponding parameters are shown in Table 6.2.

As we can see from the plot, the scaled yielding stress and shear rate data give a master plot. We can confirm that the network fracture is related to the breakage of the dynamic bonding which is dependent on the applied force. The results can not be described with the classical Griffith model which predicts the brittle fracture of materials with the viewpoint of energy at the crack tip. The possible reason could be that in Griffith model, the relaxation

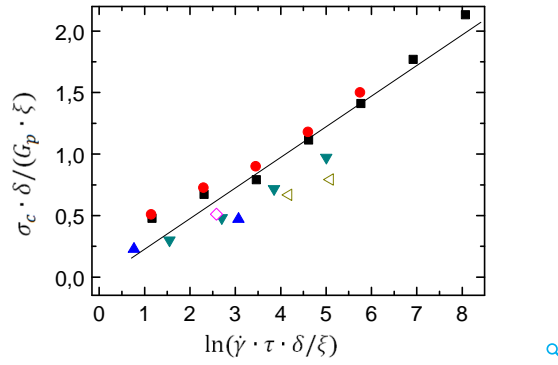


Figure 6.18: Scaled yielding stress vs. scaled shear rate data for two samples at different temperatures.

| Samples Parameters | PIB4K-(Barb)2 | | PIB14K-(Barb)2 | |
|-----------------------|---------------|-------|----------------|-------|
| | 15° C | 20° C | 10° C | 25° C |
| δ | 2.25 nm | | 2.7 nm | |
| ξ | 5.4 nm | | 7.6 nm | |
| τ | 517 s | 113 s | 900 s | 33 s |

Table 6.2: A list of parameters used for the calculation.

time of chemical bonds is extremely high and the fracture of chemical bonds is nearly independent on the shear rate. And thus the energy for fracture is independent on the shear rate. In our case, we need to break the dynamic bond to break the materials. The breakage of such dynamic bonding can be influenced by the applied stress at high shear rate.

Stress relaxation in nonlinear region

The stress relaxation measurements were done by keeping the strain constant after startup shear for different final shear strains with constant strain rate of 1 s^{-1} for sample PIB14K-BA2. As shown in Figure 6.19a and 6.19b, with a startup shear strain of 150% which is smaller than the yield strain at 25 °C and 10 °C, the following stress relaxation shows a slow process which corresponds to a Maxwell fluid. When the strain is larger than the yield strain (strain=500%), the stress relaxation shows two processes: the first one is the fast collapse of the hydrogen bonding network and the second one is the normal terminal relaxation of a Maxwell fluid.

At small shear strain, we use the stretched exponential function to fit the stress relaxation curve.

$$\sigma(t) = \sigma_0 \exp(-(t/\tau)^\alpha) = G_p \gamma \exp(-(t/\tau)^\alpha) \quad (6.7)$$

where $\sigma(t)$ is the the stress measured at time t after cessation of shear; σ_0 is the shear stress just after cease of the startup shear; G_p is the plateau modulus; γ is the startup shear strain; τ is the relaxation time; α is the stretched exponent.

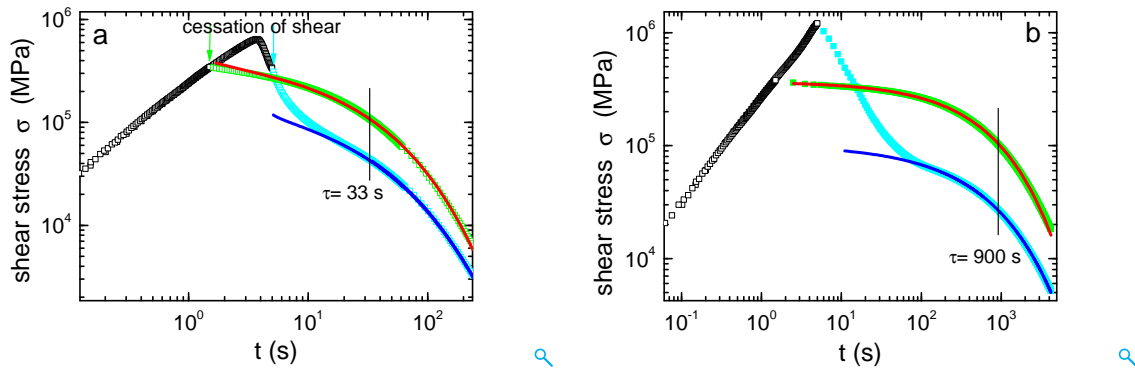


Figure 6.19: Startup shear (black squares) and the following stress relaxation data (green symbols for 150% and cyan symbols for 500%) after startup shear with strain of 150% and 500% (with a shear rate of 1 s^{-1}) for sample PIB14K-BA2 at 25 °C (left figure) and 10 °C (right figure) and the corresponding fitting curve (red curve for 150% and blue curve for 500%).

The corresponding fitting curves are shown in Figure 6.19. We can see that the model fits the experimental data very well.

| Parameters Conditions | 25 °C | | | 10 °C | | |
|--------------------------|-------------------------------------|-----------------|-----------------|-------------------------------------|-----------------|-----------------|
| | Measured from linear rheology | Fit parameters | | Measured from linear rheology | Fit parameters | |
| | | Strain 150 % | Strain 500 % | | Strain 150 % | Strain 500 % |
| G_p (MPa) | 0.314 | 0.263 | 0.087 | 0.314 | 0.245 | 0.067 |
| τ (s) | 33 | 19.96 | 344 | 900 | 619.7 | 533 |
| α | - | 0.58 | 0.47 | - | 0.59 | 0.53 |

Table 6.3: Comparison of fitting parameters and experimental values for sample PIB14K-BA2 at 10 °C and 25 °C.

The fit parameters are shown in Table 6.3. The fit parameter for the slow process are comparable with the values obtained from linear rheology. The small stretch exponents α mean broad distributions of the relaxation time.

At higher startup shear strain, the stress relaxation process can not be fitted for the whole relaxation process but only after the fast relaxation process, as we can see from the fitting curve (blue line). This means that the Maxwell fluid model is not applicable to describe the stress relaxation process after startup shear with high shear strain.

6.2.3 Modulus recovery (Self-healing) analysis after sample failure

Self-healing measurements for sample PIB14K-BA2 and PIB4K-BA2 were done by measuring the dynamic storage modulus G' 30 seconds (a similar time as the terminal relax-

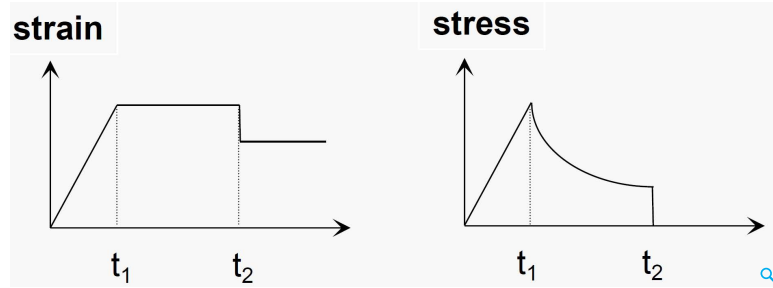


Figure 6.20: Modulus recovery experiments were done following this experimental procedure.

ation time) after startup shear measurements with shear strains larger than the yield strain, as shown in Figure 6.20. With a startup shear strain just above the yield strain, the dynamic network failed. Then the shear strain was kept constant till time $t_2=t_1+30s$ for all temperatures, which is smaller than the time of fast relaxation as shown in the stress relaxation measurements. During the waiting time (from t_1 to t_2), shear stress decreases due to fast fracture of the network. Then the shear stress was reduced to zero by reducing the strain and the dynamic oscillatory measurements were started to measure the storage modulus recovery. The

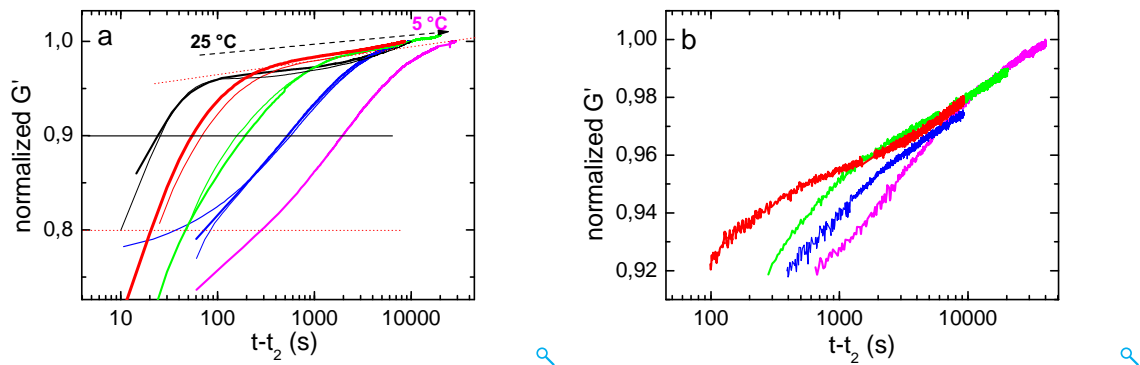


Figure 6.21: Normalized storage modulus curves for (a) sample PIB14K-BA2 and (b) sample PIB4K-BA2 at different temperatures (25 °C —, 20 °C —, 15 °C —, 10 °C —, 5 °C —).

measured storage modulus of sample PIB14K-BA2 and PIB4K-BA2 were then normalized with the reference modulus at the longest measuring time and they are plotted in Figure 6.21. We can see the recovery storage modulus curves for different temperatures differ a lot. With decreasing temperature, the recovery is much slower. As we can see from Figure 6.21a, the starting points of normalized G' for all the curves are around 0.8. Below this part, the process is very fast and difficult to measure. At long time scale, there is a slow perfecting process. We take normalized $G'=0.8$ as the starting point and $G'=1$ as the end point. Then we can take the self healing time as the time at normalized $G'=0.9$ and plot it vs. temperature. For the modulus recovery measurements of sample PIB4K-BA2, the result is shown in Figure 6.21b. As we can see from the plots, the starting point that can be measured is already up to nearly 0.92. We can then take the self-healing time for sample PIB4K-BA2 as the time $G'=0.92$

as the characteristic time for self-healing. The characteristic self-healing time for two samples and the corresponding terminal relaxation time are shown in Figure 6.22. We can see that the self-healing time and the terminal relaxation time from linear rheology at different temperatures are very similar. We know from linear dynamic rheological measurements that the terminal relaxation time is related to the dissociation of the hydrogen bonding dynamic networks which also determines the relaxation time of the dynamic network. A similar time scale between the self-healing time and the terminal relaxation time might mean that the reassociation of hydrogen bonds controls self-healing.

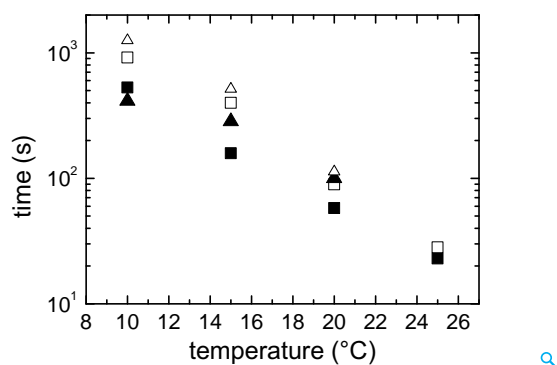


Figure 6.22: Self-healing time (filled symbols) and terminal relaxation time (unfilled symbols) depending on temperature for PIB14K-BA2 (■, □) and PIB4K-BA2 (▲, △).

6.3 Conclusion

A combined analysis of SAXS and rheological data shows that hydrogen bonding functionalized PIB forms reversible dynamic network of interconnected micelles. Two relaxation processes including PIB chain dynamics and hydrogen bonding relaxation are observed. Terminal flow is controlled by dynamic bonding and the chain dynamics corresponds to normal Rouse relaxation. Startup shear with high shear rates and large deformation leads to shear yielding followed by fast stress relaxation caused by network failure. SAOS after shear yielding shows a modulus recovery process consisting of a terminal flow dependent process and a slow perfecting of the network.

Chapter 7

Summary

In this thesis, we studied three different supramolecular polymer systems with the experimental methods of small angle X-ray scattering and rheology to investigate the structure formation and the mechanical properties of hydrogen bonding groups functionalized polymers in the bulk state. The first system includes a series of thymine/triazine functionalized telechelic PIB samples. This system shows self-assembled micelles caused by unspecific hydrogen bonding and demixing between hydrogen bonding end groups and PIB main chains. The second system is a supramolecular block copolymer PnBA-PIB linked with Hamilton wedge/Barbituric acid hydrogen bonding groups. This system resembles a covalently bonded block copolymer and shows ordered lamellar structure. The third system includes a series of Barbituric acid bifunctionalized supramolecular PIB samples. This system shows interconnected micellar network where barbituric acid groups aggregate into clusters and act as cross-link points.

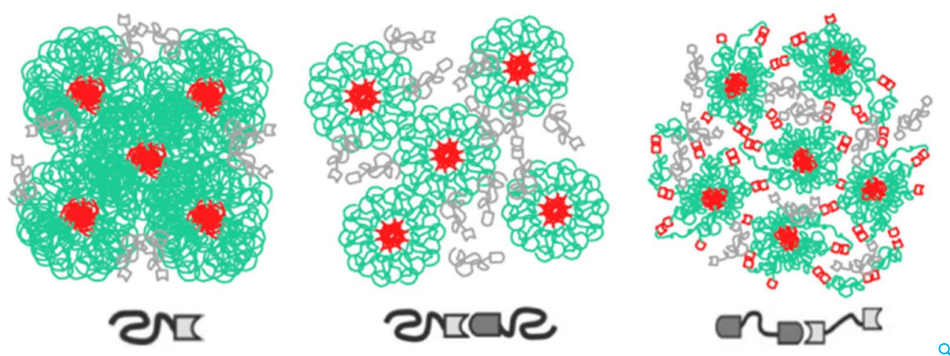


Figure 7.1: Different kinds of micellar structure formed in the supramolecular PIB melts: ordered micelles, disordered micelles and crosslinked micellar network.

The first system includes four hydrogen bonding telechelic PIB samples: a triazine monofunctional PIB, a thymine monofunctional PIB, a mixture of the triazine monofunctional PIB and the thymine monofunctional PIB, and a mixture of triazine bifunctional PIB and thymine bifunctional PIB. These four hydrogen bonding functional PIB samples were studied semi-quantitatively with SAXS and rheology. Three different micellar structures were found:

ordered micelles, disordered micellar fluid, and crosslinked micellar network. Figure 7.1 shows the schematic pictures of three different micelles. The SAXS patterns of disordered micelles were fitted well with Perkus-Yevick hard sphere model. The viscosity-volume fraction of micelles of the disordered micellar fluid can be fitted with the empirical equation from colloidal suspension. In such a system, besides the demixing between hydrogen bonding groups and the PIB chains, unspecific hydrogen bonding was found to be an important factor to influence the structural formation of supramolecular polymers in the bulk state.

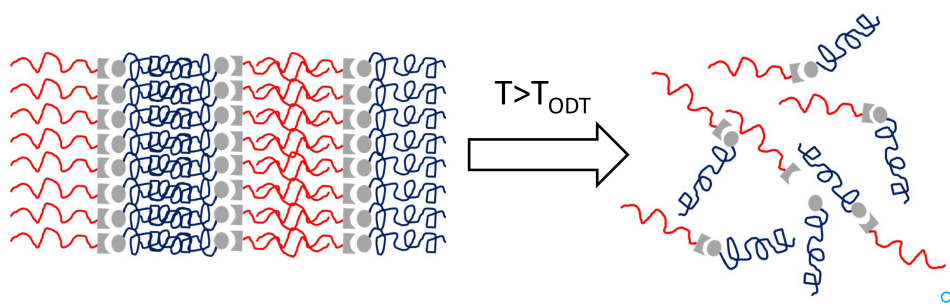


Figure 7.2: The supramolecular block copolymer shows ordered lamellar structure below T_{ODT} and disordered state above T_{ODT} .

The second system is a supramolecular block copolymer PnBA-PIB sample which is linked through Hamilton wedge/Barbituric acid hydrogen bonding groups. It was investigated with SAXS and rheology and an ordered lamellar structure was found at lower temperatures. At higher temperatures, the order-disorder transition was confirmed with both SAXS patterns and dynamic modulus curves. Figure 7.2 shows the schematic picture of the order-disorder transition from ordered lamellar structure to disordered state. In the disordered state, one different behavior from the normal covalently bonded block copolymer was observed: the mean distance between the supramolecular block copolymer increases with temperature. This indicates that an increasing fraction of the supramolecular block copolymers disassociates with increasing temperature. Such a mixture of supramolecular block copolymers and disassociated polymer blocks are in an equilibrium state because there is no macrophase separation upto 180 °C and the ordered lamellar structure is reversible after cooling. In such a system, specific multiple hydrogen bonding is dominant. The unspecific hydrogen bonding might also forms but it is not a key factor to dictate the structure of the supramolecular block copolymers. The demixing between PIB and PnBA is the key factor to influence the structural formation.

The third system includes several barbituric acid bifunctional PIB samples. The molecular weight of PIB was varied from 4 kg/mol to 28 kg/mol. Such system is interesting because it shows self-healing properties. SAXS patterns show that the sample forms aggregates. In rheological modulus curves, a long flat storage modulus plateau can be observed even for the unentangled PIB samples. While at lower frequency, terminal flow can be found. With SAXS and rheological analysis, interconnected dynamic networks (as shown in Figure 7.3) can be concluded and the terminal relaxation of the dynamic network is controlled by dynamic hydrogen bonding. Nonlinear rheological behavior was studied and shear yielding behavior was observed. Self-healing kinetics were studied by measuring the modulus recov-

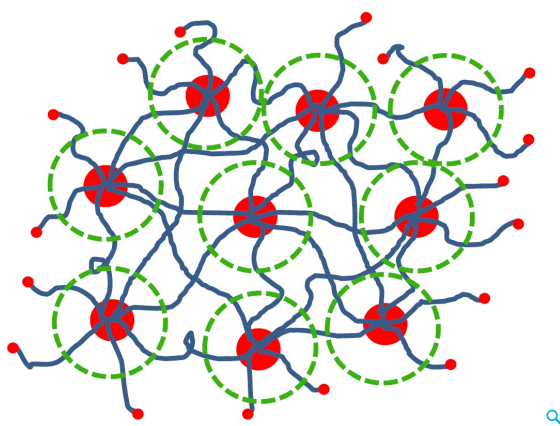


Figure 7.3: interconnected micellar network of supramolecular PIB samples.

ery after startup shear measurements. Most of the modulus recovery was finished within a time which is similar as the terminal relaxation time of the dynamic network. The difference of rheological properties between the barbituric acid bifunctional PIB network and the thymine/triazine bifunctional PIB mixture can be due to the stronger aggregation (stronger hydrogen bonding) of thymine/triazine compared to the barbituric acid groups [115]. That might also explain why barbituric acid bifunctional PIB samples shows self-healing properties while the thymine/triazine bifunctional PIB mixture not.

In conclusion, several kinds of aggregates were found in the three supramolecular polymer systems and the driving forces for these aggregates are different. For the hydrogen bonding functional nonpolar PIB samples, the demixing between the hydrogen bonding groups and the main chain plays a more important role in influencing the structural formation and rheological properties than the specific hydrogen bonding in the bulk state. A large amount of unexpected unspecific hydrogen bonding was found in several samples, which can act as another important factor. For the supramolecular block copolymer, the main driving force for the structure is the demixing between two polymer blocks and the specific hydrogen bonding was found to be very effective and structure formed was as expected.

Appendix

A. SAXS data

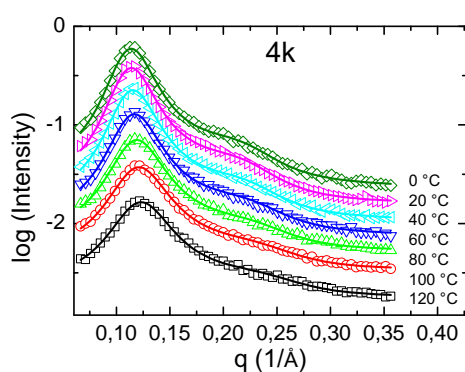


Figure A1: SAXS data (symbols) and curve fitting with hard sphere model (solid lines) for PIB4K-BA2 at a series of temperatures.

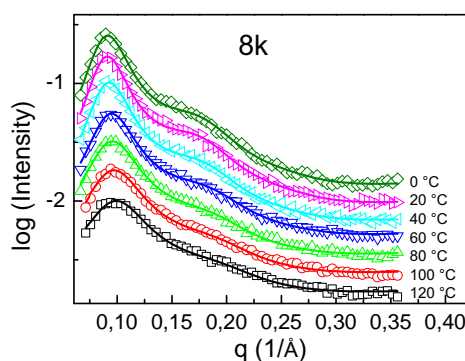


Figure A2: SAXS data (symbols) and curve fitting with hard sphere model (solid lines) for PIB8K-BA2 at a series of temperatures.

Figure A1 and A2 show the SAXS data (symbols) of PIB4K-BA2 and PIB8K-BA2 at a series of temperatures. The SAXS curves look very similar as the sample PIB14K-BA2. A peak and a bump in the SAXS pattern can be clearly seen and they become weaker with

increasing temperatures. The curve fitting (in solid lines) with hard sphere model were done and the fitting curves are shown also in Figure A1 and A2. The fitting works well, similarly as PIB14K-BA2.

B. Rheological data

Figure A3a and A3b show the original dynamic modulus curves of sample PIB4K-BA2 and PIB8K-BA2 at a series of temperatures. Master curve constructions were done with the shift factors from homopolymer PIB with molecular weight of 30 kg/mol. Figure A4a and A4b show the master curves of PIB4K-BA2 and PIB8K-BA2 with a reference temperature of 25 °C.

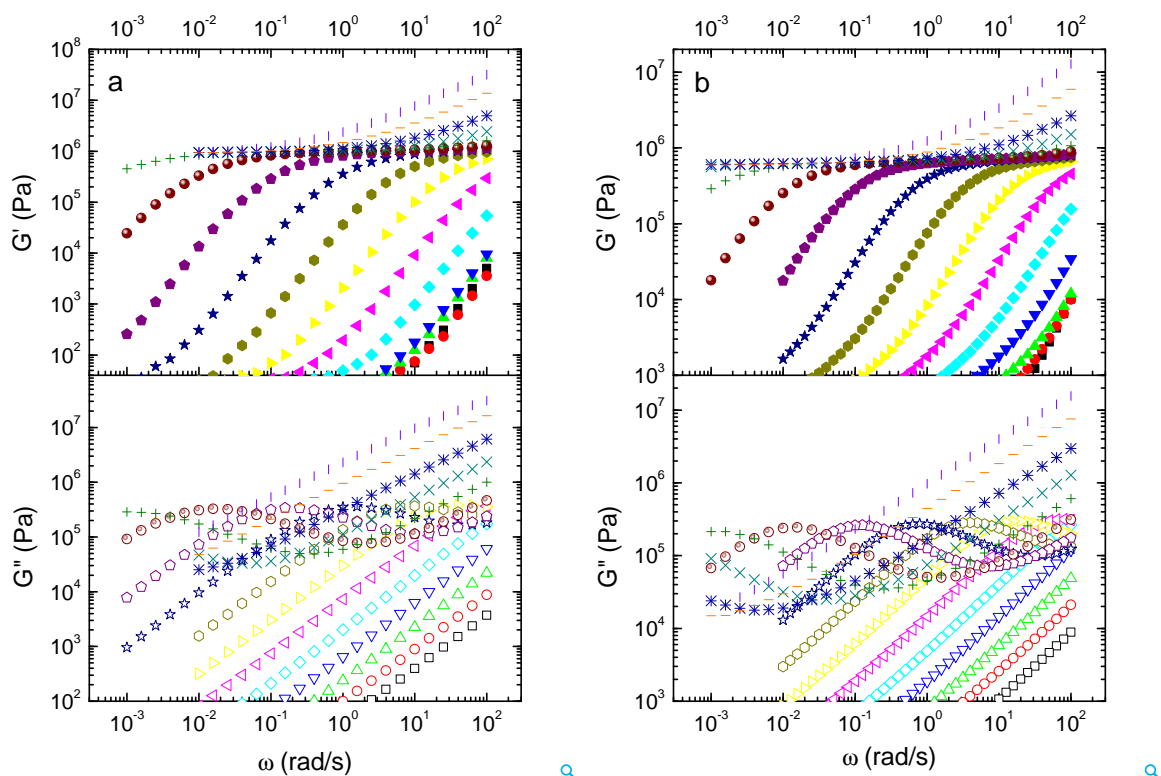


Figure A3: Complex modulus (G' , G'') v.s. angular frequency ω for (a) PIB4K-BA2 and (b) PIB8K-BA2 at different temperatures (-30 °C |, -20 °C —, -10 °C *, 0 °C x, 10 °C +, 20 °C ⊙, 30 °C ◇, 40 °C ★, 50 °C ◻, 60 °C ▷, 70 °C ◁, 80 °C ◊, 90 °C ▽, 100 °C △, 110 °C ◊, 120 °C □).

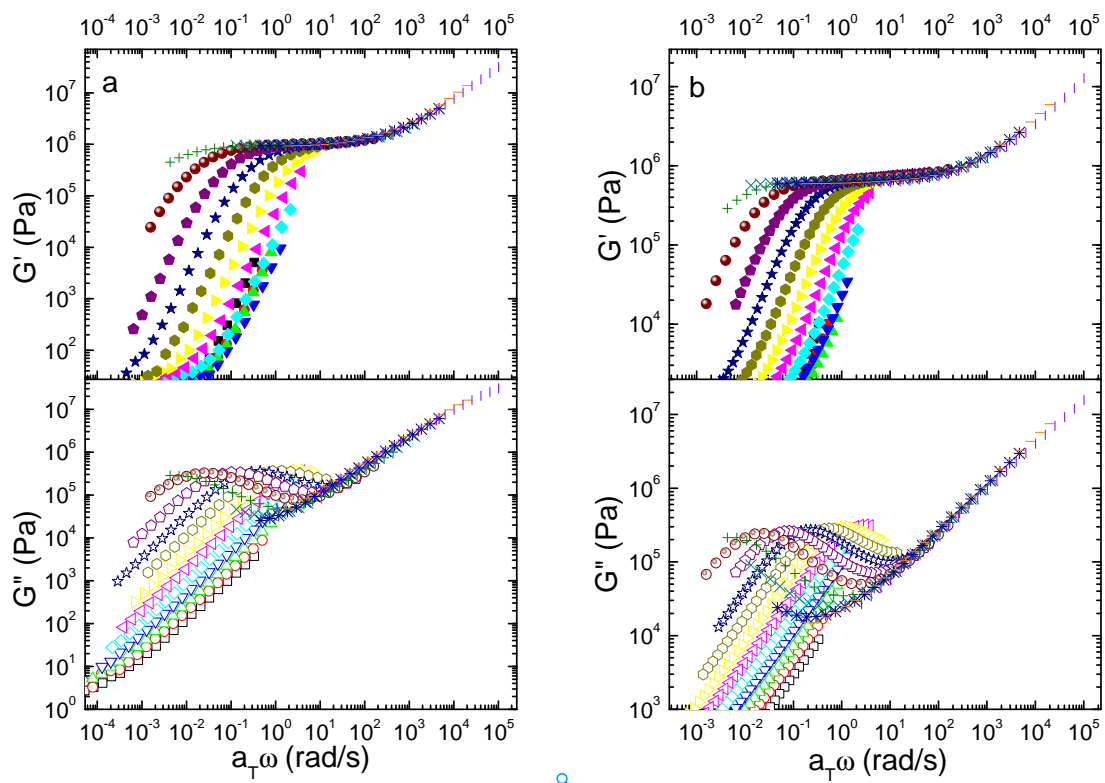


Figure A4: Master curves of (a) samples PIB4K-BA2 and (b) PIB8K-BA2 with a reference temperature of 25 °C. Different symbols represent the curves measured at different temperatures, same to the plots shown in Figure A3.

C. Startup shear

Figure A5a and A5b show the stress-strain curves of startup shear measurements for PIB8K-BA2 and PIB28K-BA2. Shear yielding can be clearly observed for PIB8K-BA2 and PIB28K-BA2. The yielding point for PIB8K-BA2 is sharp and can be clearly observed while PIB28K-BA2 not.

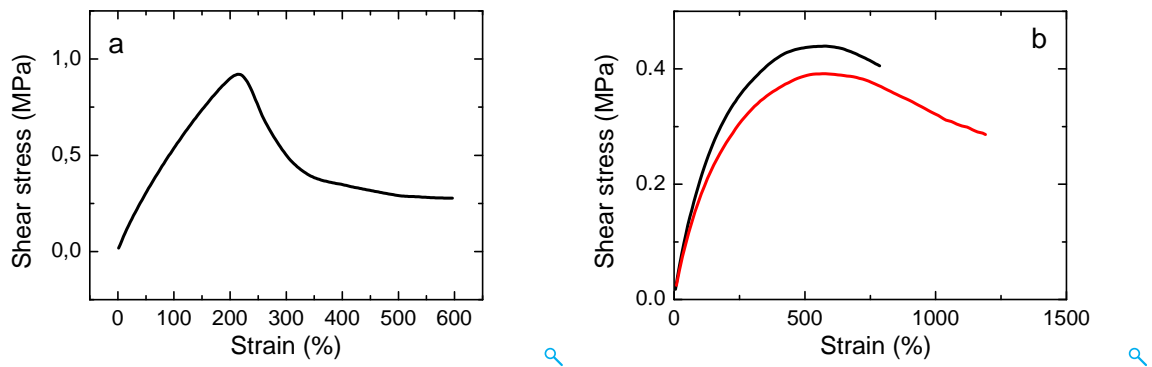


Figure A5: (a) Stress-strain curve for PIB8K-BA2 at 25 °C for $\dot{\gamma}\tau=33$; (b) Stress-strain curve for PIB28K-BA2 at 25 °C for $\dot{\gamma}\tau=27$ (—) and at 20 °C for $\dot{\gamma}\tau=23$ (—).

Bibliography

- [1] G. R. Strobl and G. R. Strobl, *The physics of polymers*, vol. 2. Springer, 1997.
- [2] H. Staudinger, “über polymerisation,” *Ber. Deut. Chem. Ges.*, vol. 53, p. 1073, 1920.
- [3] D. R. Paul, *Polymer blends*, vol. 1. Elsevier, 2012.
- [4] T. P. Lodge, “Block copolymers: Past successes and future challenges,” *Macromolecular Chemistry and Physics*, vol. 204, no. 2, pp. 265–273, 2003.
- [5] K. Wolf, H. Frahm, and H. Harms, “The state of arrangement of molecules in liquids,” *Z Phys Abt B*, vol. 36, pp. 237–287, 1937.
- [6] J.-M. Lehn, “Supramolecular chemistry-scope and perspectives molecules, supermolecules, and molecular devices (nobel lecture),” *Angewandte Chemie International Edition in English*, vol. 27, no. 1, pp. 89–112, 1988.
- [7] C. Fouquey, J.-M. Lehn, and A.-M. Levelut, “Molecular recognition directed self-assembly of supramolecular liquid crystalline polymers from complementary chiral components,” *Advanced Materials*, vol. 2, no. 5, pp. 254–257, 1990.
- [8] L. Brunsveld, B. J. B. Folmer, E. W. Meijer, and R. P. Sijbesma, “Supramolecular polymers,” *Chemical Reviews*, vol. 101, no. 12, pp. 4071–4097, 2001.
- [9] W. H. Binder and R. Zirbs, “Supramolecular polymers and networks with hydrogen bonds in the main- and side-chain,” *Advances in Polymer Science*, vol. 207, pp. 1–78, 2007.
- [10] L. Bouteiller, “Assembly via hydrogen bonds of low molar mass compounds into supramolecular polymers,” *Advances in Polymer Science*, vol. 207, no. Hydrogen Bonded Polymers, pp. 79–112, 2007.
- [11] G. R. Whittell, M. D. Hager, U. S. Schubert, and I. Manners, “Functional soft materials from metallopolymers and metallosupramolecular polymers,” *Nature materials*, vol. 10, no. 3, pp. 176–188, 2011.
- [12] F. Wang, J. Zhang, X. Ding, S. Dong, M. Liu, B. Zheng, S. Li, L. Wu, Y. Yu, H. W. Gibson, and F. Huang, “Metal coordination mediated reversible conversion between linear and cross-linked supramolecular polymers,” *Angewandte Chemie International Edition*, vol. 49, no. 6, pp. 1090–1094, 2010.

- [13] J. Cortese, C. Soulie-Ziakovic, M. Cloitre, S. Tence-Girault, and L. Leibler, "Order-disorder transition in supramolecular polymers," *J. Am. Chem. Soc.*, vol. 133, pp. 19672–75196, 2011.
- [14] F. Herbst, S. Seiffert, and W. H. Binder, "Dynamic supramolecular poly(isobutylene)s for self-healing materials," *Polymer Chemistry*, vol. 3, no. 11, pp. 3084–3092, 2012.
- [15] M. Wathier and M. W. Grinstaff, "Synthesis and properties of supramolecular ionic networks," *Journal of the American Chemical Society*, vol. 130, no. 30, pp. 9648–9649, 2008. PMID: 18593156.
- [16] M. Hayashi, A. Noro, and Y. Matsushita, "Viscoelastic properties of supramolecular soft materials with transient polymer network," *Journal of Polymer Science Part B: Polymer Physics*, vol. 52, no. 11, pp. 755–764, 2014.
- [17] T. Aida, E. W. Meijer, and S. I. Stupp, "Functional supramolecular polymers," *Science*, vol. 335, no. 6070, pp. 813–817, 2012.
- [18] R. Agnaou, M. Capelot, S. Tence-Girault, F. Tournilhac, and L. Leibler, "Supramolecular thermoplastic with 0.5 pa s melt viscosity," *Journal of the American Chemical Society*, vol. 136, no. 32, pp. 11268–11271, 2014.
- [19] P. Cordier, F. Tournilhac, C. Soulie-Ziakovic, and L. Leibler, "Self-healing and thermoreversible rubber from supramolecular assembly," *Nature*, vol. 451, no. 7181, pp. 977–980, 2008.
- [20] M. Burnworth, L. M. Tang, J. R. Kumpfer, A. J. Duncan, F. L. Beyer, G. L. Fiore, S. J. Rowan, and C. Weder, "Optically healable supramolecular polymers," *Nature*, vol. 472, no. 7343, pp. 334–338, 2011.
- [21] S. Sivakova, D. A. Bohnsack, M. E. Mackay, P. Suwanmala, and S. J. Rowan, "Utilization of a combination of weak hydrogen-bonding interactions and phase segregation to yield highly thermosensitive supramolecular polymers," *J. Am. Chem. Soc.*, vol. 127, no. 51, pp. 18202–18211, 2005.
- [22] F. Herbst, D. Döhler, P. Michael, and W. H. Binder, "Self-healing polymers via supramolecular forces," *Macromolecular Rapid Communications*, vol. 34, no. 3, pp. 203–220, 2013.
- [23] R. J. Wojtecki, M. A. Meador, and S. J. Rowan, "Using the dynamic bond to access macroscopically responsive structurally dynamic polymers," *Nature Materials*, vol. 10, no. 1, pp. 14–27, 2011.
- [24] B. J. B. Folmer, R. P. Sijbesma, R. M. Versteegen, J. A. J. van der Rijt, and E. W. Meijer, "Supramolecular polymer materials: Chain extension of telechelic polymers using a reactive hydrogen-bonding synthon," *Adv. Mater.*, vol. 12, no. 12, pp. 874–878, 2000.

-
- [25] R. P. Sijbesma, F. H. Beijer, L. Brunsveld, B. J. B. Folmer, J. H. K. K. Hirschberg, R. F. M. Lange, J. K. L. Lowe, and E. W. Meijer, "Reversible polymers formed from self-complementary monomers using quadruple hydrogen bonding," *Science*, vol. 278, no. 5343, pp. 1601–1604, 1997.
- [26] S. Abed, S. Boileau, and L. Bouteiller, "Supramolecular association of acid-terminated poly(dimethylsiloxane)s. 2. molecular weight distributions," *Macromolecules*, vol. 33, no. 22, pp. 8479–8487, 2000.
- [27] T. F. A. de Greef, G. Ercolani, G. B. W. L. Ligthart, E. W. Meijer, and R. P. Sijbesma, "Influence of selectivity on the supramolecular polymerization of ab-type polymers capable of both a center dot a and a center dot b interactions," *Journal of the American Chemical Society*, vol. 130, no. 41, pp. 13755–13764, 2008.
- [28] T. Park and S. C. Zimmerman, "Interplay of fidelity, binding strength, and structure in supramolecular polymers," *Journal of the American Chemical Society*, vol. 128, no. 44, pp. 14236–14237, 2006.
- [29] J. SARTORIUS and H.-J. SCHNEIDER, "A general scheme based on empirical increments for the prediction of hydrogen-bond associations of nucleobases and of synthetic host-guest complexes," *Chemistry*, vol. 2, no. 11, pp. 1446–1452, 1996.
- [30] B. A. Blight, C. A. Hunter, D. A. Leigh, H. McNab, and P. I. Thomson, "An aaaa-dddd quadruple hydrogen-bond array.," *Nature Chemistry*, vol. 3, no. 3, 2011.
- [31] J. D. Fox and S. J. Rowan, "Supramolecular polymerizations and main-chain supramolecular polymers," *Macromolecules*, vol. 42, no. 18, pp. 6823–6835, 2009.
- [32] F. Herbst, K. Schröter, I. Gunkel, S. Gröger, T. Thurn-Albrecht, J. Balbach, and W. H. Binder, "Aggregation and chain dynamics in supramolecular polymers by dynamic rheology: Cluster formation and self-aggregation," *Macromolecules*, vol. 43, no. 23, pp. 10006–10016, 2010.
- [33] P. J. Woodward, D. H. Merino, B. W. Greenland, I. W. Hamley, Z. Light, A. T. Slark, and W. Hayes, "Hydrogen bonded supramolecular elastomers: Correlating hydrogen bonding strength with morphology and rheology," *Macromolecules*, vol. 43, no. 5, pp. 2512–2517, 2010.
- [34] J. L. Wietor, D. J. M. van Beek, G. W. Peters, E. Mendes, and R. P. Sijbesma, "Effects of branching and crystallization on rheology of polycaprolactone supramolecular polymers with ureidopyrimidinone end groups," *Macromolecules*, vol. 44, no. 5, pp. 1211–1219, 2011.
- [35] D. J. M. van Beek, A. J. H. Spiering, G. W. M. Peters, K. te Nijenhuis, and R. P. Sijbesma, "Unidirectional dimerization and stacking of ureidopyrimidinone end groups in polycaprolactone supramolecular polymers," *Macromolecules*, vol. 40, no. 23, pp. 8464–8475, 2007.

- [36] H. Kautz, D. J. M. van Beek, R. P. Sijbesma, and E. W. Meijer, "Cooperative end-to-end and lateral hydrogen-bonding motifs in supramolecular thermoplastic elastomers," *Macromolecules*, vol. 39, no. 13, pp. 4265–4267, 2006.
- [37] J. Cortese, C. Soulie-Ziakovic, S. Tence-Girault, and L. Leibler, "Suppression of mesoscopic order by complementary interactions in supramolecular polymers," *Journal of the American Chemical Society*, vol. 134, no. 8, pp. 3671–3674, 2012.
- [38] W. H. Binder, S. Bernstorff, C. Kluger, L. Petraru, and M. J. Kunz, "Tunable materials from hydrogen-bonded pseudo block copolymers," *Advanced Materials*, vol. 17, no. 23, pp. 2824–2828, 2005.
- [39] L. M. Pitet, A. H. M. van Loon, E. J. Kramer, C. J. Hawker, and E. W. Meijer, "Nanostructured supramolecular block copolymers based on polydimethylsiloxane and polylactide," *Acs Macro Letters*, vol. 2, no. 11, pp. 1006–1010, 2013.
- [40] M. D. Hager, P. Greil, C. Leyens, S. van der Zwaag, and U. S. Schubert, "Self-healing materials," *Advanced Materials*, vol. 22, no. 47, pp. 5424–5430, 2010.
- [41] J. K. Kim and C. D. Han, "Phase behavior and phase transitions in ab- and aba-type microphase-separated block copolymers," *Advances in Polymer Science*, vol. 231, no. Polymer Materials: Block-Copolymers, Nanocomposites, Organic/Inorganic Hybrids, Polymethylenes, pp. 77–145, 2010.
- [42] F. S. Bates and G. H. Fredrickson, "Block copolymer thermodynamics: Theory and experiment," *Annu. Rev. Phys. Chem.*, vol. 41, pp. 525–557, 1990.
- [43] E. Helfand and Z. R. Wasserman, "Block copolymer theory. 4. narrow interphase approximation," *Macromolecules*, vol. 9, no. 6, pp. 879–888, 1976.
- [44] L. Leibler, "Theory of microphase separation in block copolymers," *Macromolecules*, vol. 13, no. 6, pp. 1602–1617, 1980.
- [45] I. Hamley, *The Physics of Block Copolymers*. Oxford science publications, Oxford University Press, 1998.
- [46] M. W. Matsen and F. S. Bates, "Unifying weak- and strong-segregation block copolymer theories," *Macromolecules*, vol. 29, no. 4, pp. 1091–1098, 1996.
- [47] D. J. Kinning and E. L. Thomas, "Hard-sphere interactions between spherical domains in diblock copolymers," *Macromolecules*, vol. 17, no. 9, pp. 1712–1718, 1984.
- [48] M. Schwab and B. Stühn, "Thermotropic transition from a state of liquid order to a macrolattice in asymmetric diblock copolymers," *Physical Review Letters*, vol. 76, no. 6, pp. 924–927, 1996.
- [49] E. E. Dormidontova and T. P. Lodge, "The order-disorder transition and the disordered micelle regime in sphere-forming block copolymer melts," *Macromolecules*, vol. 34, no. 26, pp. 9143–9155, 2001.

-
- [50] R. Roe, *Methods of X-ray and Neutron Scattering in Polymer Science*. ACS symposium series, Oxford University Press, 2000.
- [51] J. Ferry, *Viscoelastic properties of polymers*. Wiley, 1961.
- [52] M. Rubinstein and R. Colby, *Polymer Physics*. Oxford University Press, 2003.
- [53] M. E. D. Rosa and H. H. Winter, “The effect of entanglements on the rheological behavior of polybutadiene critical gels,” *Rheol. Acta*, vol. 33, no. 3, pp. 220–237, 1994.
- [54] D. Quemada and C. Berli, “Energy of interaction in colloids and its implications in rheological modeling,” *Advances in Colloid and Interface Science*, vol. 98, no. 1, pp. 51 – 85, 2002.
- [55] P. N. Pusey and W. van Meegen, “Phase-behavior of concentrated suspensions of nearly hard colloidal spheres,” *Nature*, vol. 320, no. 6060, pp. 340–342, 1986.
- [56] I. M. Krieger and T. J. Dougherty, “A mechanism for non-newtonian flow in suspensions of rigid spheres,” *Transactions of the Society of Rheology*, vol. 3, pp. 137–152, 1959.
- [57] P. J. Skrzyszewska, J. Sprakel, F. A. de Wolf, R. Fokkink, M. A. Cohen Stuart, and J. van der Gucht, “Fracture and self-healing in a well-defined self-assembled polymer network,” *Macromolecules*, vol. 43, no. 7, pp. 3542–3548, 2010.
- [58] M. Fukuda, K. Osaki, and M. Kurata, “Nonlinear viscoelasticity of polystyrene solutions. i. strain-dependent relaxation modulus,” *Journal of Polymer Science: Polymer Physics Edition*, vol. 13, no. 8, pp. 1563–1576, 1975.
- [59] T. Z. Yan, K. Schröter, F. Herbst, W. H. Binder, and T. Thurn-Albrecht, “Nanostructure and rheology of hydrogen-bonding telechelic polymers in the melt: From micellar liquids and solids to supramolecular gels,” *Macromolecules*, vol. 47, no. 6, pp. 2122–2130, 2014.
- [60] L. Fetters, D. Lohse, and R. Colby, “Chain dimensions and entanglement spacings,” in *Physical properties of polymers handbook*, pp. 447–454, Springer, 2007.
- [61] L. J. Fetters, D. J. Lohse, D. Richter, T. A. Witten, and A. Zirkel, “Connection between polymer molecular weight, density, chain dimensions, and melt viscoelastic properties,” *Macromolecules*, vol. 27, no. 17, pp. 4639–4647, 1994.
- [62] C. P. Royall, W. C. K. Poon, and E. R. Weeks, “In search of colloidal hard spheres,” *Soft Matter*, vol. 9, no. 1, pp. 17–27, 2013.
- [63] W. C. K. Poon, E. R. Weeks, and C. P. Royall, “On measuring colloidal volume fractions,” *Soft Matter*, vol. 8, no. 1, pp. 21–30, 2012.

- [64] A. N. Semenov, J. F. Joanny, and A. R. Khokhlov, "Associating polymers: Equilibrium and linear viscoelasticity," *Macromolecules*, vol. 28, no. 4, pp. 1066–1075, 1995.
- [65] M. B. Kossuth, D. C. Morse, and F. S. Bates, "Viscoelastic behavior of cubic phases in block copolymer melts," *Journal of Rheology*, vol. 43, no. 1, pp. 167–196, 1999.
- [66] L. J. Fetters, W. W. Graessley, and A. D. Kiss, "Viscoelastic properties of polyisobutylene melts," *Macromolecules*, vol. 24, no. 11, pp. 3136–3141, 1991.
- [67] J. R. Kumpfer, J. J. Wie, J. P. Swanson, F. L. Beyer, M. E. Mackay, and S. J. Rowan, "Influence of metal ion and polymer core on the melt rheology of metallosupramolecular films," *Macromolecules*, vol. 45, no. 1, pp. 473–480, 2012.
- [68] J. Stickel and R. Powell, "Fluid mechanics and rheology of dense suspensions," *Annual Review of Fluid Mechanics*, vol. 37, pp. 129–149, 2005.
- [69] Y. Lei and T. P. Lodge, "Effects of component molecular weight on the viscoelastic properties of thermoreversible supramolecular ion gels via hydrogen bonding," *Soft Matter*, vol. 8, no. 7, pp. 2110–2120, 2012.
- [70] E. Guth, "Theory of filler reinforcement," *Journal of Applied Physics*, vol. 16, no. 1, pp. 20–25, 1945.
- [71] N. Delbosc, M. Reynes, O. J. Dautel, G. Wantz, J.-P. Lère-Porte, and J. J. E. Moreau, "Control of the aggregation of a phenylenevinylendiimide chromophore by use of supramolecular chemistry: Enhanced electroluminescence in supramolecular organic devices," *Chemistry of Materials*, vol. 22, no. 18, pp. 5258–5270, 2010.
- [72] F. Herbst, *Dynamics of hydrogen bonds in the melt-state of supramolecular polymers*. PhD thesis, Halle, Univ., 2014.
- [73] Lüders, Friedrich, "Supramolekulare Polymere: Molekulargewichtsabhängiges Aggregationsverhalten von supramolekularem Poly-n-(Butylacrylat) und Selbstordnung eines pseudo Blockcopolymers," 2014.
- [74] S. D. Tobing and A. Klein, "Molecular parameters and their relation to the adhesive performance of acrylic pressure-sensitive adhesives," *Journal of Applied Polymer Science*, vol. 79, no. 12, pp. 2230–2244, 2001.
- [75] L. Fetters, D. Lohse, and R. Colby, "Chain dimensions and entanglement spacings," in *Physical Properties of Polymers Handbook* (J. Mark, ed.), pp. 447–454, Springer New York, 2007.
- [76] N. M. Ahmad, P. A. Lovell, and S. M. Underwood, "Viscoelastic properties of branched polyacrylate melts," *Polymer International*, vol. 50, no. 6, pp. 625–634, 2001.

-
- [77] N. Sakamoto and T. Hashimoto, "Order-disorder transition of low-molecular-weight polystyrene-block-polyisoprene .1. saxs analysis of 2 characteristic temperatures," *Macromolecules*, vol. 28, no. 20, pp. 6825–6834, 1995.
- [78] B. Stühn, R. Mutter, and T. Albrecht, "Direct observation of structure formation at the temperature-driven order-to-disorder transition in diblock copolymers," *EPL (Europhysics Letters)*, vol. 18, no. 5, p. 427, 1992.
- [79] J. H. Rosedale, F. S. Bates, K. Almdal, K. Mortensen, and G. D. Wignall, "Order and disorder in symmetric diblock copolymer melts," *Macromolecules*, vol. 28, no. 5, pp. 1429–1443, 1995.
- [80] J. H. Rosedale and F. S. Bates, "Rheology of ordered and disordered symmetric poly(ethylenepropylene)-poly(ethylethylene) diblock copolymers," *Macromolecules*, vol. 23, no. 8, pp. 2329–2338, 1990.
- [81] B. L. Riise, G. H. Fredrickson, R. G. Larson, and D. S. Pearson, "Rheology and shear-induced alignment of lamellar diblock and triblock copolymers," *Macromolecules*, vol. 28, no. 23, pp. 7653–7659, 1995.
- [82] S. Seiffert and J. Sprakel, "Physical chemistry of supramolecular polymer networks," *Chemical Society Reviews*, vol. 41, no. 2, pp. 909–930, 2012.
- [83] M. J. Serpe and S. L. Craig, "Physical organic chemistry of supramolecular polymers," *Langmuir*, vol. 23, no. 4, pp. 1626–1634, 2007.
- [84] F. Tanaka and S. F. Edwards, "Viscoelastic properties of physically cross-linked networks. transient network theory," *Macromolecules*, vol. 25, no. 5, pp. 1516–1523, 1992.
- [85] L. Bromberg, "Scaling of rheological properties of hydrogels from associating polymers," *Macromolecules*, vol. 31, no. 18, pp. 6148–6156, 1998.
- [86] C. Chassenieux, T. Nicolai, and L. Benyahia, "Rheology of associative polymer solutions," *Current Opinion in Colloid Interface Science*, vol. 16, no. 1, pp. 18–26, 2011.
- [87] R. J. Wojtecki, M. A. Meador, and S. J. Rowan, "Using the dynamic bond to access macroscopically responsive structurally dynamic polymers," *Nature materials*, vol. 10, no. 1, pp. 14–27, 2011.
- [88] Y. Lei and T. P. Lodge, "Effects of component molecular weight on the viscoelastic properties of thermoreversible supramolecular ion gels via hydrogen bonding," *Soft Matter*, vol. 8, no. 7, pp. 2110–2120, 2012.
- [89] R. F. M. Lange, M. Van Gorp, and E. W. Meijer, "Hydrogen-bonded supramolecular polymer networks," *Journal of Polymer Science Part A: Polymer Chemistry*, vol. 37, no. 19, pp. 3657–3670, 1999.

- [90] V. Castelletto, I. Hamley, X.-F. Yuan, A. Kelarakis, and C. Booth, "Structure and rheology of aqueous micellar solutions and gels formed from an associative poly (oxybutylene)–poly (oxyethylene)–poly (oxybutylene) triblock copolymer," *Soft Matter*, vol. 1, no. 2, pp. 138–145, 2005.
- [91] A. Phadke, C. Zhang, B. Arman, C.-C. Hsu, R. A. Mashelkar, A. K. Lele, M. J. Tauber, G. Arya, and S. Varghese, "Rapid self-healing hydrogels," *Proceedings of the National Academy of Sciences*, vol. 109, no. 12, pp. 4383–4388, 2012.
- [92] T.-A. Asoh, H. Yoshitake, Y. Takano, and A. Kikuchi, "Fabrication of self-healable hydrogels through sol–gel transition in metallo-supramolecular aqueous solution by aeration," *Macromolecular Chemistry and Physics*, vol. 214, no. 22, pp. 2534–2539, 2013.
- [93] P. Terech, M. Yan, M. Maréchal, G. Royal, J. Galvez, and S. K. Velu, "Characterization of strain recovery and self-healing in a self-assembled metallo-gel," *Physical Chemistry Chemical Physics*, vol. 15, no. 19, pp. 7338–7344, 2013.
- [94] M. Burnworth, L. Tang, J. R. Kumpfer, A. J. Duncan, F. L. Beyer, G. L. Fiore, S. J. Rowan, and C. Weder, "Optically healable supramolecular polymers," *Nature*, vol. 472, no. 7343, pp. 334–337, 2011.
- [95] P. J. Skrzyszewska, J. Sprakel, F. A. de Wolf, R. Fokkink, M. A. C. Stuart, and J. van der Gucht, "Fracture and self-healing in a well-defined self-assembled polymer network," *Macromolecules*, vol. 43, no. 7, pp. 3542–3548, 2010.
- [96] M. Hayashi, A. Noro, and Y. Matsushita, "Viscoelastic properties of supramolecular soft materials with transient polymer network," *Journal of Polymer Science Part B: Polymer Physics*, vol. 52, no. 11, pp. 755–764, 2014.
- [97] F. Maes, D. Montarnal, S. Cantournet, F. Tournilhac, L. Corté, and L. Leibler, "Activation and deactivation of self-healing in supramolecular rubbers," *Soft Matter*, vol. 8, no. 5, pp. 1681–1687, 2012.
- [98] D. C. Tuncaboylu, M. Sari, W. Oppermann, and O. Okay, "Tough and self-healing hydrogels formed via hydrophobic interactions," *Macromolecules*, vol. 44, no. 12, pp. 4997–5005, 2011.
- [99] F. Herbst, S. Seiffert, and W. H. Binder, "Dynamic supramolecular poly(isobutylene)s for self-healing materials," *Polym. Chem.*, vol. 3, pp. 3084–3092, 2012.
- [100] M. Matsen and R. Thompson, "Equilibrium behavior of symmetric aba triblock copolymer melts," *The Journal of chemical physics*, vol. 111, no. 15, pp. 7139–7146, 1999.
- [101] R. E. Bras and K. R. Shull, "Self-consistent field theory of gelation in triblock copolymer solutions," *Macromolecules*, vol. 42, no. 21, pp. 8513–8520, 2009.

-
- [102] M. H. Uddin, C. Rodriguez, A. Lopez-Quintela, D. Leisner, C. Solans, J. Esquena, and H. Kunieda, "Phase behavior and microstructure of poly (oxyethylene)-poly (dimethylsiloxane) copolymer melt," *Macromolecules*, vol. 36, no. 4, pp. 1261–1271, 2003.
- [103] B. E. Eichinger and P. J. Flory, "Determination of the equation of state of polyisobutylene," *Macromolecules*, vol. 1, no. 3, pp. 285–286, 1968.
- [104] L. J. Fetters, A. D. Kiss, D. S. Pearson, G. F. Quack, and F. J. Vitus, "Rheological behavior of star-shaped polymers," *Macromolecules*, vol. 26, no. 4, pp. 647–654, 1993.
- [105] J. Roovers, "Properties of the plateau zone of starbranched polybutadienes and polystyrenes," *Polymer*, vol. 26, no. 7, pp. 1091–1095, 1985.
- [106] B. Eichinger and P. Flory, "Determination of the equation of state of polyisobutylene," *Macromolecules*, vol. 1, no. 3, pp. 285–286, 1968.
- [107] A. C. Jackson, F. L. Beyer, S. C. Price, B. C. Rinderspacher, and R. H. Lambeth, "Role of metal–ligand bond strength and phase separation on the mechanical properties of metallopolymer films," *Macromolecules*, vol. 46, no. 14, pp. 5416–5422, 2013.
- [108] F. Tanaka and S. F. Edwards, "Viscoelastic properties of physically crosslinked networks. part 2. dynamic mechanical moduli," *Journal of Non-Newtonian Fluid Mechanics*, vol. 43, no. 2-3, pp. 273–288, 1992.
- [109] C. Macosko, *Rheology: principles, measurements, and applications*. New York [etc.]: Wiley-VCH, 1994.
- [110] Y. Li, M. Hu, G. B. McKenna, C. J. Dimitriou, G. H. McKinley, R. M. Mick, D. C. Venerus, and L. A. Archer, "Flow field visualization of entangled polybutadiene solutions under nonlinear viscoelastic flow conditions," *Journal of Rheology (1978-present)*, vol. 57, no. 5, 2013.
- [111] F. Tanaka and S. F. Edwards, "Viscoelastic properties of physically crosslinked networks. part 3. time-dependent phenomena," *Journal of Non-Newtonian Fluid Mechanics*, vol. 43, no. 2-3, pp. 289–309, 1992.
- [112] J.-F. Berret and Y. Serero, "Evidence of shear-induced fluid fracture in telechelic polymer networks," *Physical review letters*, vol. 87, no. 4, p. 048303, 2001.
- [113] K. A. Erk and K. R. Shull, "Rate-dependent stiffening and strain localization in physically associating solutions," *Macromolecules*, vol. 44, no. 4, pp. 932–939, 2011.
- [114] T. Koga, F. Tanaka, I. Kaneda, and F. M. Winnik, "Stress buildup under start-up shear flows in self-assembled transient networks of telechelic associating polymers," *Langmuir*, vol. 25, no. 15, pp. 8626–8638, 2009.
- [115] R. Stadler and L. de Lucca Freitas, "Thermoplastic elastomers by hydrogen bonding 1. rheological properties of modified polybutadiene," *Colloid and Polymer Science*, vol. 264, no. 9, pp. 773–778, 1986.

Acknowledgement

At the end of my PhD thesis, I would like to express my gratitude to all the people who helped and supported me during my PhD studies.

I am deeply indebted to my supervisor Prof. Dr. Thomas Thurn-Albrecht. He always encourages me and helps me to improve myself during my PhD studies. His rigorous research attitude and profound knowledge impressed me a lot and will benefit my future life. I want to thank the German Science Foundation DFG (Projects TH 1281/5-1, BI 1337/7-1, SFB / TRR 102) and the state of Saxony-Anhalt (Research Network Nanostructured Materials) for financial support. I would like to express my great gratitude to Dr. Klaus Schröter for his precious guidance of my PhD studies, broad research experiences and kind patience.

I would also like to thank Prof. Dr. Wolfgang Binder and Dr. Florian Herbst and all the collaborators in Prof. Dr. Binder's group. It was a pleasant experience for the cooperation with them and I highly appreciate the excellent samples they provided.

Many thanks to my mentor in iRTG program Prof. Dr. Wolfgang Paul for very helpful advice. Special thanks to Prof. Dr. Yongfeng Men (Changchun Institute of Applied Chemistry, Chinese Academy of Sciences) for fruitful discussion.

I would like to thank my cooperator Friedrich Lüders. He did very good work during his master thesis and I benefit a lot from him. Many thanks to Dr. Jens Lange and Ingrid Stössel for IR measurements.

Sincere thanks to my colleagues in the Polymer Physics group for their friendly help: Aline Leuchtenberger, Katrin Herfurt, Dr. Maria Ott, Dr. Anas Mujtaba, Jens Balko, Ann-Kristin Löhmann, Anne Seidlitz, Jana Rüdell, Martha Schulz, Martin Koch and our former group members. Special thanks to Dr. Gaurav Kumar Gupta and Matthias Fischer. They put a lot of efforts on the rotating anode instrument to tackle the technical problems, which helps my research work go smoothly. It was my good luck to work with all of them. This work would not have been possible without the comfortable atmosphere and the good corporation with them.

I am deeply indebted to my parents and friends for their help, support and encouragement during the entire PhD period.

Finally but importantly, I want to give sincere thanks to my wife Guoying Zhou who always supported me and encouraged me to move on with my work and whole life. I owe immense gratitude for what she did to help me reach this step.

Eidesstattliche Erklärung

Hiermit erkläre ich an Eides statt, dass ich die vorliegende Arbeit selbständig und ohne fremde Hilfe verfasst, andere als die angegebenen Quellen und Hilfsmittel nicht benutzt und die aus anderen Quellen entnommenen Stellen als solche gekennzeichnet habe.

Ferner habe ich nicht versucht, anderweitig mit oder ohne Erfolg eine Dissertation einzureichen oder mich einer Doktorprüfung zu unterziehen.

Tingzi Yan

Halle (Saale), July 1, 2015

Curriculum vitae

| | |
|----------------|---------------------|
| First Name | Tingzi |
| Family Name | Yan |
| Date of Birth | October 17, 1984 |
| Place of Birth | Heze, China |
| Nationality | China |
| E-mail | t.z.yan85@gmail.com |

EDUCATION

| | |
|-----------------------|---|
| Aug. 2003 - Jul. 2007 | Bachelor of Science University of Jinan Jinan, China |
| Aug. 2007 - Jun. 2010 | Master of Science University of Science and Technology of China Hefei, China |
| Since October. 2010 | Ph.D in Institut für Physik Experimental Polymer Physics Martin-Luther-Universität Halle-Wittenberg (Supervised by Prof. Thomas Thurn-Albrecht) |

Publications

1. T. Yan, K. Schröter, F. Herbst, W.H. Binder, and T. Thurn-Albrecht, 'Nanostructure and Rheology of Hydrogen-Bonding Telechelic Polymers in the Melt From Micellar Liquids and Solids to Supramolecular Gels' *Macromolecules*, 2014, 47(6), 2122-2130.
2. E. Ostas, T. Yan, T. Thurn-Albrecht, and W. H. Binder, 'Crystallization of Supramolecular Pseudoblock Copolymers' *Macromolecules*, 2013, 46, 4481-4490.
3. R. Zhang, T. Yan, B. D. Lechner, K. Schröter, Y. Liang, B. Li, F. Furtado, P. Sun, and K. Saalwächter, 'Heterogeneity, segmental and hydrogen bond dynamics, and aging of supramolecular self-healing rubber' *Macromolecules*, 2013, 46, 1841-1850.
4. N. Li, T. Yan, Z. Li, T. Thurn-Albrecht, and W.H. Binder, 'Comb-shaped polymers to enhance hydroxide transport in anion exchange membranes' *Energy and Environmental Science*, 2012, 5, 7888-7892.
5. E. Ostas, K. Schröter, M. Beiner, T. Yan, T. Thurn-Albrecht, W.H. Binder, 'Poly(caprolactone) poly(isobutylene) A crystallizing, hydrogen-bonded pseudo-block copolymer' *Journal of Polymer Science Part A Polymer Chemistry* 2011, 49, 3404-3416